ABSORPTION OF AMMONIA-WATER MIXTURES IN MICROSCALE GEOMETRIES FOR MINIATURIZED ABSORPTION SYSTEMS

A Dissertation
Presented to
The Academic Faculty

by

Dhruv Chanakya Hoysall

In Partial Fulfillment
of the Requirements for the Degree
Doctor of Philosophy in Mechanical Engineering

Georgia Institute of Technology
May 2018

ABSORPTION OF AMMONIA-WATER MIXTURES IN MICROSCALE GEOMETRIES FOR MINIATURIZED ABSORPTION SYSTEMS

Approved by:

Dr. Srinivas Garimella, Advisor
George W. Woodruff School of Mechanical Engineering
Georgia Institute of Technology

Dr. Satish Kumar
George W. Woodruff School of Chemical Engineering
Georgia Institute of Technology

Dr. Sheldon Jeter
George W. Woodruff School of Mechanical Engineering
Georgia Institute of Technology

Dr. Todd Sulchek
George W. Woodruff School of Mechanical Engineering
Georgia Institute of Technology

Dr. William Koros
School of Chemical and Biomolecular Engineering
Georgia Institute of Technology

Date Approved:

To my family

ACKNOWLEDGEMENTS

I would like to express my deepest gratitude to Dr. Srinivas Garimella, for his support and mentorship throughout my PhD. He has been much more than just a PhD adviser to me, he has played the role of a father figure, a mentor, a friend among other things. I hope to continue to apply and teach others what I have learnt from him.

I would like to thank my Ph.D. committee members, Drs. Sheldon Jeter, Satish Kumar, William Koros and Todd Sulchek for generously agreeing to serve on my committee and for their time and expertise in the review of my dissertation.

I would like to thank all of the current and past members of the Sustainable Thermal System Laboratory for their support, feedback and friendship. All of them have helped and guided me in different ways. I am very grateful for them pushing to be a better researcher and most importantly for making the experience at Georgia Tech a good one.

Finally, I would like to thank my family for supporting me through the highs and lows of this journey.

.

TABLE OF CONTENTS

LIST OF TABLES

LIST OF FIGURES

LIST OF SYMBOLS AND ABBREVIATIONS

A	*Area (m^2)*
Ca	*Capillary number (-)*
C_p	*Specific heat (kJ kg^{-1} K^{-1})*
Fo	*Fourier number (-)*
h	*Specific Enthalpy (kJ kg^{-1})*
IA	*Interfacial area (m^2)*
j	*Superficial Velocity (m s^{-1})*
M	*Molecular mass (kg)*
$\dot{m}$	*Mass flow rate (kg s^{-1})*
N	*Number (-)*
Nu	*Nusselt number (-)*
$\dot{n}$	*Mass flux (kg m^{-2})*
P	*Pressure (kPa)*
Pix	*Pixels (-)*
Pr	*Prandtl number (-)*
q	*Quality (-)*
Q	*Heat (W)*
R	*Thermal resistance (K W^{-1})*
Re	*Reynolds number (-)*
Sc	*Schmidt number (-)*

Sh	*Sherwood number (-)*
STD	*Standard deviation (-)*
T	*Temperature (K/°C)*
th	*Thickness (m)*
U	*Overall heat transfer coefficient (W m^{-2} K^{-1})*
x	*Concentration (kg kg^{-1})*
X	*Martinelli Parameter (-)*
$\tilde{z}$	*Concentration of condensing flux (kg kg^{-1})*

Greek Symbols

α	*Heat transfer coefficient (W m^{-2} K^{-1})*
β	*Mass transfer coefficient (m s^{-1})*
ε	*Void fraction (-)*
η	*Fin efficiency (-)*
μ	*Mean (-)*
ρ	*Density (kg m^{-3})*
σ	*Standard deviation (%)*
ϕ	*Heat transfer correction parameter (-)*
Φ	*Two-phase multiplier (-)*
Ψ	*Two-phase multiplier for bend (-)*

Subscripts

A	*Ammonia*
abs	*Absorbed/Absorption*
air	*Air*

avg	*Average*
ch	*Channel*
cf	*Coupling fluid*
in	*Inlet*
int	*Interface*
L	*Liquid*
MC	*Microchannel*
out	*Outlet*
seg	*Segment*
serp	*Serpentine*
T	*Total*
v	*Vapor*
W	*Water*
wall	*Wall*

SUMMARY

Vapor absorption-based HVAC systems are attracting increased interest due to their capability to utilize low-grade waste-heat streams, and low global warming potential of the working fluids. The performance of an absorption system depends significantly on the absorber, which absorbs the refrigerant vapor into the absorbent fluid. Components with microscale features to enhance heat and mass transfer have been shown to significantly reduce the size of absorption cooling systems, making them viable for small-scale applications, such as residential and mobile use. But an incomplete understanding of the internal flow phenomena in microscale absorbers is limiting those gains.

Performance limiting factors for microscale absorbers are investigated. One of the key performance limiting factors is maldistribution of vapor and liquid phases in these microscale geometries. Air-water mixtures are used to represent two-phase flow through three different microscale geometries, namely, a microchannel array, a microchannel array with mixing sections, and a serpentine pin-fin test section. The flow distribution is visually tracked along the length of the microscale geometries. Statistical distributions of void fraction and interfacial area along the microchannel array are calculated. Parameters such as the average void fraction and interfacial area intensity are used to evaluate and compare the different microscale geometries.

This study also investigates the internal flow phenomena in an absorber by visualizing the process of absorption and measuring local temperatures in microscale geometries. A single unit of a microscale absorber consisting of two heat exchange plates; one with an ammonia–water mixture, and the other with a coupling fluid to absorb the heat released

during absorption, is fabricated. Heat and mass transfer mechanisms in the microscale components are investigated. An open absorption system was fabricated to evaluate the absorber, as it enables control over inlet properties of the fluids. Two microscale absorber designs are evaluated in the test facility. The effects of solution flow rate, solution nominal concentration, operating pressures, and coupling fluid temperature are evaluated. A model is developed to predict heat and mass transfer in these microscale absorbers. This study provides insight into the limiting factors of current designs, and improvements that can be made in the future designs of such components.

CHAPTER 1. INTRODUCTION

The demand for primary energy has been rapidly rising in the past few decades (U.S.EIA, 2016). This has increased the pressure on the existing energy infrastructure and resources. Rattner and Garimella (2011) found that 20.3% of electricity use in the USA is for HVAC&R systems, which typically use vapor compression cycles. Vapor compression systems convert high-grade electricity to cooling and heating. Thermally driven vapor absorption systems provide alternatives to vapor compression systems, and utilize low-grade heat, rather than electrical power, to provide cooling/heating. This presents the opportunity to reduce electricity consumption and utilize non-conventional energy sources such as waste heat and solar energy. The use of an ammonia-water mixture as a working fluid allows cooling at below freezing temperatures and heating above 50°C, unlike lithium bromide-water based absorption systems. Ammonia vapor has a lower specific volume than water vapor at the relevant operating conditions, which makes it possible to miniaturize components without excessive pressure drop penalties. Absorption cooling systems have typically been used in large-scale applications such as hospitals, university campuses, etc., or in low coefficient-of-performance installations such as recreational vehicles. Determan and Garimella (2012) demonstrated 300 W of cooling using an ammonia-water absorption system miniaturized into a 200 mm × 200 mm × 34 mm monolith. This text-book-sized monolith contained all heat and mass transfer components required for an absorption system. All sub-components of the monolith utilized microchannel passages, which provide high heat and mass transfer coefficients compared to conventional designs, resulting in substantial reduction in the required size and weight of the system. The small size of the microchannel-based absorption cooling system broadens its potential applications to include residential and other small-scale applications. Among the various heat and mass exchange components

in an absorption heat pump, the absorber has been referred to as the "bottleneck" of the system by Beutler *et al.* (1996). Hence, the absorber is critical to the performance of an absorption system.

The absorption of ammonia into the dilute solution is an exothermic process, which must be actively cooled by a coupling fluid. The lack of understanding of the heat and mass transfer processes in microscale geometries has resulted in suboptimal designs for components. This study investigates an ammonia-water absorber with multiple arrays of microscale features to enhance performance. A microscale absorber is fabricated with windows to provide visual access to observe the effect of the microscale features on the flow of the vapor-liquid mixture as absorption takes place. These observations provide insights into the heat and mass transfer mechanisms in microscale absorbers. A second test section to measure intermediate temperatures is also fabricated and these intermediate temperatures are used to validate the heat and mass transfer models.

1.1 Literature review

1.1.1 Maldistribution in microchannels

Flow regimes, condensation, evaporation and related two-phase flow phenomena in a single microchannel are widely studied. However, studies on multiphase flow through arrays of parallel microchannels are limited. Flow maldistribution in microchannel components can adversely affect heat exchanger performance, especially those with phase change. For example, maldistribution in evaporators results in channels with dry-out as some channels would have a lower liquid flow rate than others. In condensers, excess liquid in some channels affects the rate of heat transfer and condensation. In absorbers and desorbers, maldistribution reduces the total interfacial area that is vital for efficient mass transfer and phase change. Therefore, even flow distribution in heat and mass exchangers is critical to optimize performance of these components.

Ozawa *et al.* (1989) studied the distribution of air-water mixtures in two parallel tubes of 3.1 mm diameter. They observed uneven distribution of the phases between the channels. This maldistribution was attributed to pressure and flow oscillations caused by pressure drop characteristics of two-phase flow at different operating conditions. Gas flow rates were observed to oscillate more than liquid flow rates.

The effect of orientation of a 6 parallel microchannel (d_h = 0.333 mm) array on evaporation was investigated by Kandlikar and Balasubramanian (2005). The vertical downward configuration used in this study had the most significant effect of flow reversal of vapor into the inlet manifold. This flow reversal was observed to be the primary cause for increased flow maldistribution, resulting in a reduction in heat transfer performance. Pressure drop fluctuations and flow patterns in the same test section were studied by Balasubramanian and Kandlikar (2005). Slug flow was observed to be the dominant flow regime in the microchannels. Significant maldistribution was observed in some cases. This was attributed to flow reversal extending into the inlet manifold due to slug flow.

Hetsroni *et al.* (2003) investigated air-water and steam-water flow in parallel triangular microchannels with hydraulic diameters of 0.1-0.16 mm. The test sections were 15 mm × 15 mm in size and consisted of 17-26 parallel microchannels. Different flow regimes were observed in the parallel channels with some channels exhibiting very low or no liquid flow. Flow maldistribution was observed in steam-water boiling experiments as well, where channels close to the inlet had lower vapor flow than those away from the inlet.

The available literature shows that gas-liquid maldistribution is a significant detriment to flow in microchannel arrays. While there are several studies investigating

improved header designs for better flow distribution, there are no studies on improving flow distribution in a microchannel array once it is maldistributed.

1.1.2 Two-phase flow through micro-pin fins

Pin fin arrays with varying geometry offer the potential to adapt the flow area in a microchannel array to address the challenges posed by the evolving flow characteristics. However, two-phase flow around circular micro-pin fins in small-gap passages has not been widely investigated.

Nitrogen-water flow across pin fins was investigated by Krishnamurthy and Peles (2007) using high-speed videography. The pin fins had a diameter and height of 0.1 mm, with a pitch-to-diameter ratio of 1.5, and $5 < Re < 50$. Four distinct flow regimes, bubbly-slug, gas slug, bridged, and annular flow were observed. Based on the data, they developed models to calculate the void fraction and pressure drop in two-phase flow across pin fins for $Re_d < 40$.

Krishnamurthy and Peles (2008b) present the effect of pin diameter and pitch on flow regime. Two distinct mechanisms for the formation of bridged flow were observed. In the smaller test section, gas slugs trapping liquid bridges between pin fins were the main mechanism for bridge flow. In the larger test section, the break-up of larger liquid slugs resulted in the formation of liquid bridges. A parameter K, defined as the product of the Weber (We) and Euler (Eu) numbers, is proposed to predict the stability of the bridge flow: the bridge flow regime is stable at $K << 1$, and unstable as $K \rightarrow 1$.

A pressure drop model for the boiling of water through 0.2×0.2 mm square pin fins with a height of 0.67 mm and a pitch of 0.4 mm is presented by Qu and Siu-Ho (2009). The single-phase friction factor correlation from Qu and Siu-Ho (2008) in combination with the laminar liquid and vapor Lockhart and Martinelli (1949) two-phase multiplier predicted their data well.

1.1.3 Ammonia-water studies

The present work primarily focuses on the miniaturization of vapor absorption systems using convective flow absorbers. The literature on absorption in convective flow absorbers can be subdivided into experimental and theoretical studies.

Experimental studies

Merrill *et al.* (1995) investigated three compact bubble absorbers developed for Generator-Absorber-Exchange (GAX) cycles. Each of the three designs was a variation of the inverted concentric U-tube design investigated in Merrill *et al.* (1994). The three new designs were compared with the baseline design of an inverted concentric U-tube with solution and vapor flowing in a co-current configuration in the inner tube as presented in Merrill *et al.* (1994). Further research on the inverted U-tube bubble absorber design was conducted by Merrill *et al.* (1998). Improved ammonia vapor distribution, and a reduction in the hydraulic diameter of the solution and coolant sides significantly improved performance of the absorber. The best performing absorber was an inverted U-tube with alternating actively cooled regions and adiabatic mixing regions. Flow inserts on the coolant side were also observed to improve absorber performance, as the cooling side resistance decreased.

Lee *et al.* (2002b) investigated the use of a plate-type absorber for ammonia-water absorption cycles. The absorber had dimensions of 0.112×0.264×0.003 m and operated in a counter-flow configuration. The absorber was tested in an open system with an ammonia vapor source and a dilute solution source. Dilute solution concentrations were varied from 0-30 wt% at a constant flow rate of 0.3 kg min^{-1} and temperature of 20°C. The log mean temperature and concentration differences were used to calculate the heat and mass transfer coefficients. The heat transfer coefficient was observed to increase with gas and solution flow rates. While the mass transfer coefficient increased with gas flow rates, it remained relatively constant with an increase in solution flow rates. The same

geometry was tested in a falling-film mode in a counter-flow configuration. The performance of the falling-film mode was compared to the bubble-mode performance by Lee *et al.* (2002a). Bubble-mode was observed to have much better mass transfer, while the falling-film mode had better heat transfer performance. The overall performance of the bubble mode was observed to be better as more ammonia was absorbed in the bubble mode.

Cerezo *et al.* (2009) investigated the use of a corrugated plate heat exchanger as an absorber. The inlet and outlet temperatures, pressures and flow rates of all fluids entering and leaving the absorber were measured. The absorber was tested in an open system, where an ammonia tank and dilute solution reservoir supplied the inlet streams to the absorber. This allowed them to precisely control the operating conditions. Logarithmic mean temperature and concentration differences were used to calculate the heat and mass transfer coefficients. An increase in solution flow rate, operating pressure and coupling fluid flow rates improved absorber performance. Conversely, an increase in dilute solution concentration, and dilute solution and coupling fluid temperatures deteriorates the absorber performance.

The microscale heat and mass exchanger concept developed by Nagavarapu and Garimella (2011) was built and tested as an absorber for an ammonia water absorption chiller by Nagavarapu (2012). The absorber was tested as part of a 2.5 kW ammonia-water absorption chiller. The microscale features in the absorber included semi-circular microchannel arrays, and inlet and outlet headers to distribute flow through the microscale channels. Two different designs of the absorber were investigated. Both designs consisted of microscale channel arrays. The first design had separate vapor ports in each channel to distribute ammonia vapor evenly between each of the microchannels. The second concept had ammonia vapor and dilute solution mixing upstream of the absorber, and a two-phase mixture entering the microscale channel arrays. The absorber

performance was observed to be lower than the design value. This below-design performance was attributed to three specific issues: complete blockage of some of the microchannels by the braze alloy, partial blockage of other microchannels, and flow mal-distribution of vapor and liquid among the different channels.

After fabrication techniques were improved to minimize blockage of the microscale channels, absorber performance improved but was still sub-design. The measured temperatures indicated that the solution exiting the absorber was subcooled. Bubbles were also observed exiting the absorber through a sight glass at the absorber exit. This indicated incomplete absorption in the absorber. Hence, maldistribution of vapor and liquid was deemed to be the most probable cause of below-design performance. Based on these tests, it was concluded that further testing of the component is required in a setup where the internal processes can be observed and flow distribution investigated.

Theoretical studies

Herbine and Perez-Blanco (1995) presented a model for a vertical tube bubble absorber. The vapor and liquid flowed co-current to each other. The model solves the bulk temperatures and concentrations at different positions in the absorber using empirical correlations for heat and mass transfer coefficients. The model predicted an almost linearly decreasing vapor concentration profile with length, which is not expected in co-current flow absorbers. Nagavarapu and Garimella (2011) present the use of microscale heat and mass exchangers in absorption heat pumps. The microscale heat and mass exchanger consists of alternating etched plates Microscale features are used to enhance heat transfer in heat and mass exchangers. The microscale features include microchannel arrays for the flow of the ammonia-water solution, ammonia vapor and coupling fluid, and inlet and outlet headers to uniformly distribute the flow. A model for the microscale component to be used as an absorber is developed in the study. The model

is based on the approach used by Price and Bell (1974), which in turn used the model for condensation of a binary fluid developed by Colburn and Drew (1937). It is shown that the use of microscale features enhances heat transfer, and significantly reduces the absorber size.

Cerezo *et al.* (2010) developed a heat and mass transfer model for the corrugated plate absorber tested in Cerezo *et al.* (2009). The Colburn and Drew (1937) analogy was implemented to model mass transfer. An iterative solver was developed for the model equations. The model assumed spherical bubbles of vapor with constant velocity to model the vapor phase. Initial bubble size was determined based on the inlet orifice diameter, and the number of bubbles was calculated based on vapor flow rate. A comparison of the results with experimental values showed that all trends were correctly predicted. The heat transfer was predicted with a mean error of 7%, while the mass transfer model had an accuracy of 19%.

The absorber models developed so far make significant assumptions to simulate the absorber. Perfect distribution was assumed by Nagavarapu and Garimella (2011). The flow is also assumed to be annular throughout the microchannels. Similarly, Cerezo *et al.* (2010) assume spherical bubbles with constant velocities to model absorbers. The use of the Colburn and Drew (1937) approach requires an estimation of interfacial area to calculate the mass transferred between vapor and liquid phases. Flow visualization will aid in improving the accuracy of determining the interfacial area. This study aims to improve the understanding of ammonia-water absorption in microscale heat exchangers.

1.2 Research objectives

Based on the above discussion, the objectives of the present study are as follows:

1. Experimentally investigate two-phase flow phenomena in microscale heat exchanger plate geometries with microchannels and pin fins.

2. Quantify the effect of factors such as maldistribution on heat and mass transfer in these geometries, and the impact of changes to overcome these limitations.
3. Observe the progression of absorption via thermal and optical measurements in microscale geometries. Identify the limitations in realizing complete absorption. Develop new designs to address limiting factors.
4. Develop a heat and mass transfer model to predict heat and mass transfer in the microscale absorber. Implement refinements based on experimental results.
5. Develop a pressure drop model for the serpentine micro-pin fin geometry.
6. Compare the performance of microchannel and serpentine pin fin absorber designs.

Two experimental test facilities were constructed to achieve these objectives. The first test setup was used to optically investigate two-phase flow through heat exchanger plates with microscale features. The second was used to investigate the performance of these microscale geometries as an absorber.

1.3 Dissertation organization

This dissertation is organized in several chapters as follows:

- Chapter 2 presents experimental results on maldistribution of two-phase flow in microchannel array heat exchanger plates using air-water mixtures to simulate two-phase flow.
- Chapter 3 investigates the use of a novel serpentine micro-pin fin geometry to improve two-phase distribution and phase interaction in a heat exchanger plate.
- Chapter 4 presents the investigation of a serpentine micro-pin fin absorber.
- Chapter 5 presents the investigation of a microchannel absorber.
- Chapter 6 presents the conclusions from this investigation and recommendations for future work..

CHAPTER 2. MALDISTRIBUTION IN MICROCHANNEL HEAT AND MASS EXCHANGERS

2.1 Introduction

Flow regimes, condensation, evaporation and related two-phase flow phenomena in a single microchannel are widely studied in literature. However, studies on multiphase flow through arrays of parallel microchannels are more limited. Flow maldistribution in microchannel components can adversely affect heat exchanger performance, especially those with phase change. For example, maldistribution in evaporators results in channels with dry-out as some channels would have a higher liquid flow rate than others. In condensers, excess liquid in some channels affects the rate of heat transfer and condensation. In absorbers and desorbers, maldistribution reduces the total interfacial area that is vital for efficient mass transfer and phase change. Therefore, flow distribution in heat and mass exchangers is critical to optimize performance of these components.

Ozawa *et al.* (1989) studied the distribution of air-water mixtures in two parallel tubes of 3.1 mm diameter. They observed uneven distribution of the phases between the channels. This maldistribution was attributed to pressure and flow oscillations caused by pressure drop characteristics of two-phase flow at different operating conditions. Gas flow rates were observed to oscillate more than liquid flow rates. Tshuva *et al.* (1999) studied the flow distribution of air and water between two tubes of 24 mm diameter and 3 m length at different inclinations. Even flow distribution was observed for horizontal flow conditions. The flow was observed to become progressively uneven as the angle of

inclination increased from 0° to 90°. Evenly distributed flow in the vertical configuration was observed only at higher superficial velocities of water (~ 1 m s^{-1}) or air (~ 8 m s^{-1}). The effect of orientation of a 6 parallel microchannel (d_h = 333 μm) array on evaporation was also investigated by Kandlikar and Balasubramanian (2005). The vertical downward configuration used in this study had the most significant effect of flow reversal of vapor into the inlet manifold. This flow reversal was observed to be the primary cause for increased flow maldistribution, resulting in a reduction in heat transfer performance. Pressure drop fluctuations and flow in the same test section were studied by Balasubramanian and Kandlikar (2005). Slug flow was observed to be the dominant flow regime in the microchannels. Significant maldistribution was observed in some cases. This was attributed to flow reversal extending into the inlet manifold due to slug flow.

Visualization of flow in an evaporator with six parallel channels, each with a hydraulic diameter of 1 mm, was conducted by Kandlikar *et al.* (2001). Large pressure fluctuations were observed, which were attributed to the vigorous evolution of vapor in the particular flow regimes with nucleate boiling.

Hetsroni *et al.* (2003) investigated air-water and steam-water flow in parallel triangular microchannels with hydraulic diameters of 0.1-0.16 mm. The test sections were 15 mm × 15 mm in size and consisted of 17-26 parallel microchannels. Different flow regimes were observed in the parallel channels with some channels exhibiting very low or no liquid flow. Flow maldistribution was observed in steam-water boiling experiments as well, where channels close to the inlet had lower vapor flow than those away from the inlet.

Peles (2003) studied boiling in 13-50 triangular parallel channels, 16 mm long, with hydraulic diameters of 50-200 μm. Large pressure oscillations were observed, which caused flow reversal. Four flow regimes, namely, rapid bubble flow, bubble flow, complete bubble flow, and annular flow were observed.

Studies on flow visualization in multiple parallel channels focus on the instabilities that arise due to boiling in micro- and mini- channels. The working fluid at the inlet of the evaporator is primarily in single phase in those studies. On the other hand, the working fluid that enters an actual component such as an evaporator or absorber is often already a two-phase mixture. In such cases, the extent of maldistribution of the two phases can be worse.

Earlier studies (Fei and Hrnjak (2004); Vist and Pettersen (2004); Marchitto *et al.* (2008); Ahmad *et al.* (2009); Mahvi and Garimella (2017)) focused on the header and changes in the header geometry for improved distribution. These studies show that the header geometry can significantly improve flow distribution, but some maldistribution persists in the channels. The goal of the present study is to understand two-phase flow in channel arrays and to improve distribution using flow mixing features between channels at intermediate locations.

Microchannel heat exchangers have the potential to take advantage of the high heat transfer coefficients typical of microchannels, thereby transferring large heat duties in compact envelopes. However, the use of microchannel heat exchangers in applications with two-phase flow presents new challenges, namely flow distribution. In applications with mass transfer between the gas and liquid phases, even distribution not only of the

overall flow, but also of the gas and liquid phases, is critical, because the respective species in the vapor and liquid phases must be able to physically interact with each other to achieve the necessary transport. Preferential flow of only liquid or only vapor in specific channels precludes such interactions, and even if some heat transfer to the coupling fluid is possible, the essential species transport does not occur. One such application is in an absorber, where vapor is absorbed into a solution. Nagavarapu and Garimella (2011) model the application of a microchannel absorber in compact absorption heat pump systems. A two-phase mixture of refrigerant vapor and dilute solution flows through the component to yield a concentrated single-phase liquid solution at the outlet. They demonstrated that microchannels can significantly reduce the size of the absorber. However, their model assumes even distribution of vapor and liquid in each channel, and any maldistribution could result in the requirement of larger components to achieve the necessary transport, negating the gains from the use of microchannels. Determan and Garimella (2012) present the application of microchannel components to integrate an entire absorption system into a monolithic block. The monolithic block integrates four components with two-phase flow, namely the absorber, desorber, condenser and evaporator. In such integrated microchannel heat and mass exchanger sub-assemblies, the potential problem of maldistribution assumes critical significance in establishing the viability of the compactness offered by microscale transport.

In the present investigation, the potential for maldistribution across microchannel arrays similar to those used by Nagavarapu and Garimella (2011) and Determan and Garimella (2012) is investigated and quantified in detail. Also, a new microchannel array

configuration that incorporates flow mixing features is investigated to assess its potential to reduce maldistribution.

The effect of phase maldistribution on evaporator and condenser performance has been investigated in literature, whereas this work investigates the impact of phase maldistribution on the performance of microchannel absorbers. In absorbers, species transport across the vapor-liquid interface is as important as effective heat transfer area. As the function of absorbers is to fully absorb a high purity vapor into a solution, they are particularly susceptible to maldistribution.

2.2 Experimental setup

Figure 2.1 shows a schematic of the test facility used in the present study. The test facility was constructed to enable investigation of two-phase flow through 52 parallel microchannels with a depth of 0.306 mm and width of 0.750 mm. Air-water mixtures were used as the two-phase working fluid. A supply tank is partially filled with distilled water, dyed red and pressurized to 350 kPa using compressed air. The inlet air to the test section is drawn from the top of the pressurized tank, while the water is drawn from the bottom. The flow rate of each stream is set using flow control valves and measured using

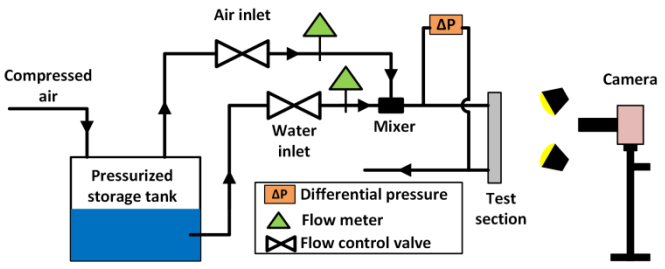

Figure 2.1: Schematic of experimental setup

the flow meters specified in Table 2.1. The air and water streams are then mixed through a T-section, following which the mixture flows to the inlet of the test section. The air-water mixture then flows through the test section in a vertically downward direction. At the outlet of the test section, the water is collected in a storage tank. A high-speed camera (Photron FASTCAM Ultima 1024 with Nikon Micro-NIKKOR 105 mm lens) is used to record high-speed videos at specific locations along the length of the test section. In addition to flow visualization, the pressure drop across the test section is measured using a differential pressure transducer for each flow condition. The mixture mass quality was varied from 0.03 to 0.15, with the corresponding volumetric qualities varying from 0.96 to 0.995. The mass fluxes through the test section ranged from 18 to 60 kg m^{-2} s^{-1}. The volumetric flow rates correspond to those typically used in microchannel absorbers for small-capacity ammonia-water absorption heat pumps.

Table 2.1: Instrument specifications

Parameter	Instrument	Range	Uncertainty
Inlet Air Volumetric Flow Rate	Rotameter	0.4 – 8.0 $\times 10^{-5}$ m^3 s^{-1}	5%
Inlet Water Volumetric Flow Rate	Rotameter	.2 – 2.6 $\times 10^{-6}$ m^3 s^{-1}	4%
Test Section Differential Pressure	Differential Pressure Transducer	0 – 175 kPa	0.245 kPa

Two microchannel geometries are tested and analyzed. Images of these geometries are shown in Figure 2.2. Test Section 1 consists of 52 parallel microchannels that have a length of 174 mm. Test Section 2 has the same width and length as Test Section 1 as shown in Figure 2.2, but, it consists of a repeating array of 52-53 parallel micro channels, each with a length of 11.5 mm followed by a mixing section with a length of 1.75 mm. This pattern repeats itself 13 times. The mixing sections shown in Figure 2.2(c) are gaps between microchannels that allow for flow from all channels to mix and redistribute among the next set of channels. These mixing sections are incorporated to improve flow distribution of initially maldistributed flow. The arrays of microchannels are not directly aligned, but are staggered as shown in Figure 2.2(c), to further facilitate flow redistribution. Both configurations have rectangular channels with large fillets on corners similar to the designs presented by Nagavarapu and Garimella (2011). The test sections are fabricated by photochemical etching of a 304 stainless steel sheet.

The test section is sealed by compressing the etched sheet against a Plexiglas plate using a metal back plate, as shown in Figure 2.3. The top and bottom plates are machined from aluminum. The back plate has a machined slot to place the microchannel test section. Multiple gaskets are used to prevent leaks from the microchannels. A gasket is placed in the pocket in the bottom plate, as shown in Figure 2.3, the test section is placed above it, and a second gasket is placed around the test section. A rectangular Plexiglas plate is placed on top of this assembly and fits into a frame machined on the back of the top plate. The top plate has six windows with dimensions of 68.58 mm × 25.4 mm. The first and last windows, referred to as 'W-Inlet' and 'W-outlet', are used to view the inlet and outlet ports on the bottom plate, respectively. The four windows labeled W-1 to W-4 are used to

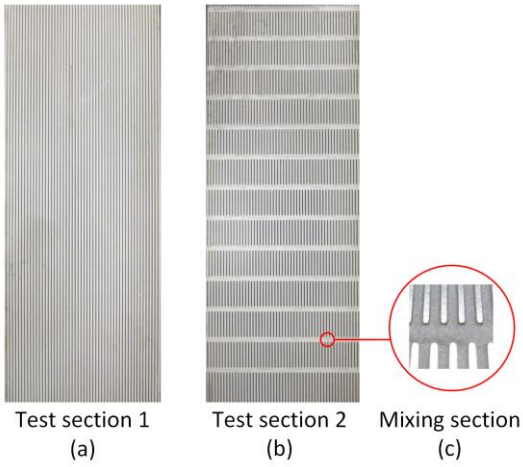

Figure 2.2: Microchannel test sections

observe flow across the test section. The test section is sealed by tightening the bolts placed at the edges of the top and bottom plates. The test section assembly has inlet and outlet ports at the center of the rectangular header of the test section. The two-phase mixture is distributed by the rectangular header across the microchannels. This results in a greater portion of the liquid flowing through the channels in the center, and more air flow through the channels close to the edges. The inlet and outlet ports are cylindrical, with a 6.35 mm NPT connection into the headers. The test sections were cut using a wire EDM, which resulted in the edges at the inlet and outlet having sharp features.

2.2.1 Flow visualization

A Photron FASTCAM Ultima 1024 camera with Nikon Micro-NIKKOR 105 mm lens is used to take high speed videos. The distilled water is dyed red to help differentiate between the two phases. Videos were recorded at 250 frames per second, at a shutter speed of 1/1000 second and a resolution of 1024 × 512 pixels. Flow videos are recorded

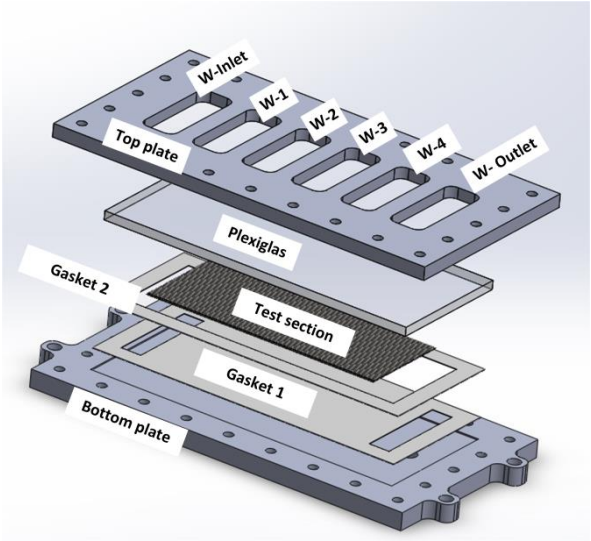

Figure 2.3: Illustration of the test section assembly

for 4 seconds to capture any intermittency that may occur during flow. Each video records the flow in all 52 channels. Videos at four different locations along the length are captured. This enables the tracking of changes in flow characteristics along the length in each of the sheets. Figure 2.4 presents a representative image of the flow in a microchannel array sheet.

2.2.2 Data reduction

The images from the high speed videos were cropped and rotated as shown in Figure 2.4.

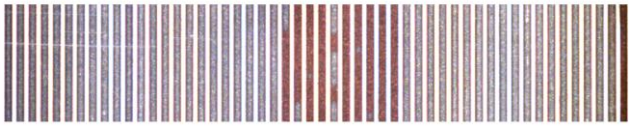

Figure 2.4 Representative image of flow through test section

The red regions represent the liquid regions, extruded white regions are the channel walls, and the grey regions represent air. Annular and slug flows are the most common flow regimes observed. The images are converted to an RGB format. In addition, an image of only liquid flowing through the microchannels is captured, referred to as the calibration image in Figure 2.5. The calibration image is used to determine channel boundaries and distinguish regions with and without flow. The red regions are identified by using the individual RGB index values to differentiate between colors. A threshold for the red color was used to differentiate between air and water to identify the liquid regions. Once the liquid regions are identified, the image is converted to a binary black and white image with liquid in black and gas in white, as shown in Figure 2.6. This binary image is further processed using a 2-D median filter that removes noise from the image. The liquid-only image is again processed using the same method to identify the liquid and non-liquid regions. The processed image is then used to identify the channel boundaries of each of the 52 microchannels. Figure 2.7 presents a noise-filtered image combined with the information about the positions of channel boundaries.

An average void fraction for individual channels is calculated using Equation (2.1). The number of air pixels is divided by the total number of pixels in the channel. This ratio is calculated for every frame of the video and is averaged over time. The temporally and spatially averaged void fraction per channel is plotted as shown in Figure 2.8. The distribution of void fraction is an indication of the distribution of vapor and liquid across multiple channels.

$$\alpha_{avg,ch} = \frac{\sum Pix_{air}}{\sum Pix_{ch}} \tag{2.1}$$

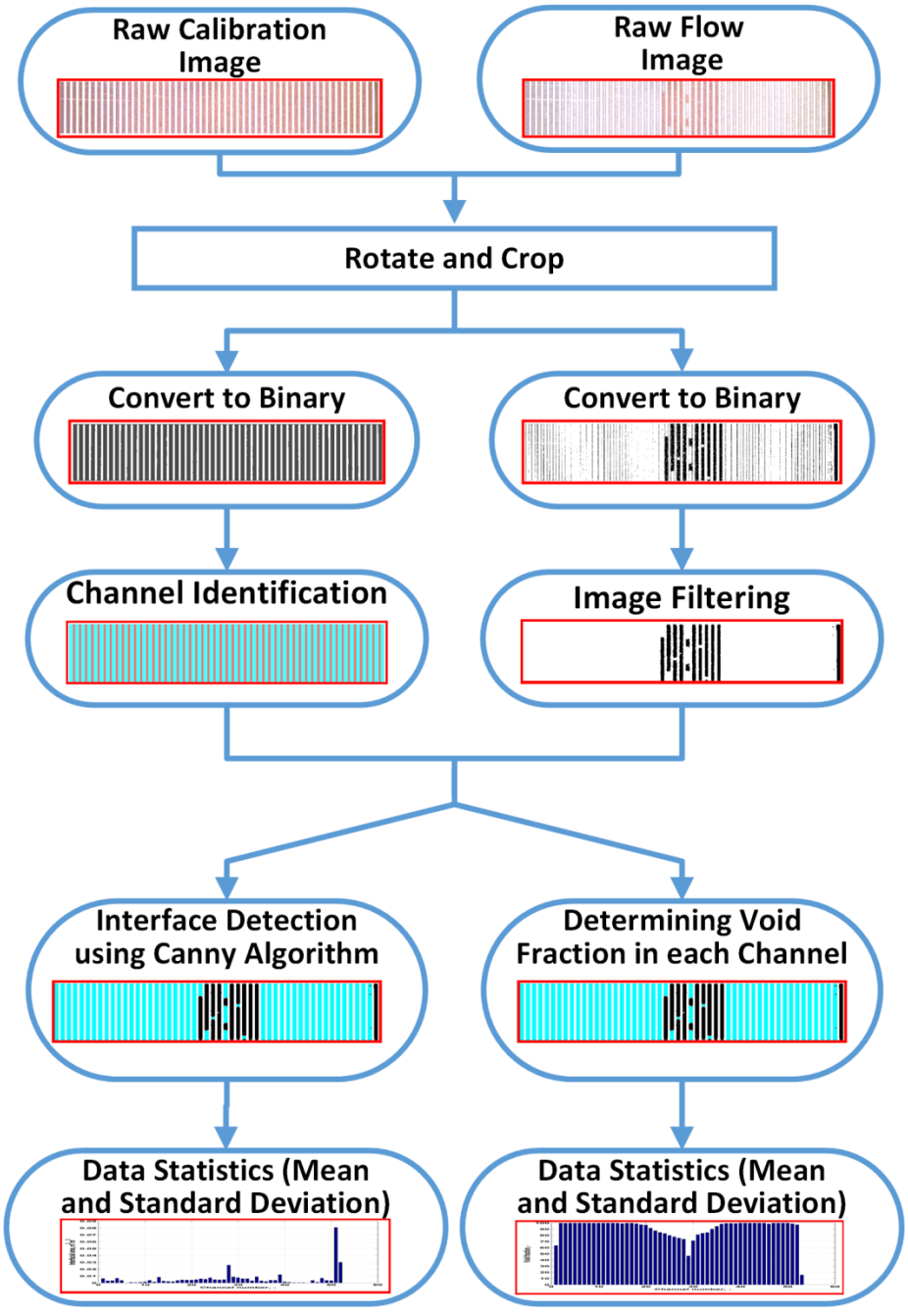

Figure 2.5: Data reduction algorithm for the analysis of flow videos

The Canny edge detector is then used to identify air-water interfaces in the image. The interfaces are represented by the red lines shown in Figure 2.7. The total interfacial area is calculated for each channel. To compare different images, interfacial area intensity is

Figure 2.6: Binary image obtained after initial processing

defined as the ratio of the number of pixels in the interface to the total number of pixels of the channel, as shown in Equation (2.2). This intensity is used to compare the performance of the two test sections. An even distribution of interfacial area intensity across the microchannels indicates good mixing between the two phases.

$$IA_{Intensity} = \frac{\sum Pix_{int}}{\sum Pix_{ch}} \tag{2.2}$$

The above data reduction method is used on the high-speed videos of both test sections. The void fractions and interfacial areas for both microchannel array configurations are compared.

2.2.3 Uncertainty analysis

The uncertainty associated with this analysis is quantified using Equation (2.3). The first

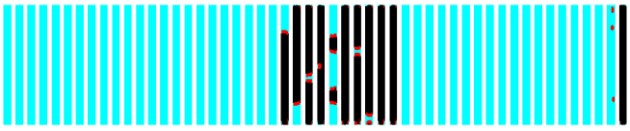

Figure 2.7: Processed image showing interfaces and channel boundaries

two terms account for the uncertainty associated with the red threshold, by estimating the change in void fraction with a 10% change in the threshold. The third and fourth terms account for the uncertainty due to the wrong identification of a pixel as liquid or air. Equation (2.3) presents the uncertainty in the measurement of void fraction of a channel for a representative data point. In the present study, the uncertainty in void fraction ranged from 0.8% to 1.7% for Configuration 1, and 1.8% to 4.0% for Configuration 2.

$$
\begin{aligned}
U_{\alpha_{Flow}} &= \sqrt{\left(\Delta_{\alpha_{Flow},110\%}\right)^2 + \left(\Delta_{\alpha_{Flow},90\%}\right)^2 + \left(\Delta_{\alpha_{Flow},+1}\right)^2 + \left(\Delta_{\alpha_{Flow},-1}\right)^2} \\
U_{\alpha_{Flow}} &= \sqrt{(-0.486)^2 + (0.698)^2 + (-0.05)^2 + (0.05)^2} \\
U_{\alpha_{Flow}} &= 0.853 \\
\alpha_{Flow} &= 88.29 \pm 0.85
\end{aligned}
\tag{2.3}
$$

2.3 Results and Discussion

The two test sections are tested individually at different flow rates. The average void fraction and interfacial area intensity values are calculated for each channel. Figure 2.8 shows a plot of the void fraction in each channel of Test Section 1. The void fraction in

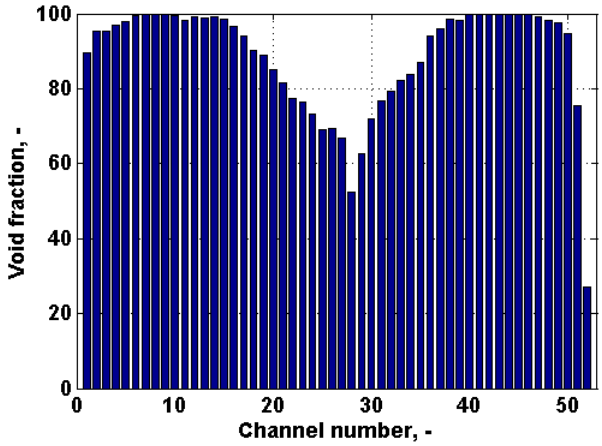

Figure 2.8: Representative void fraction distribution in Test Section 1

some channels approaches 100%, while others have a much lower value. This indicates maldistribution of liquid through the microchannels. The channels close to the center receive a major portion of the liquid flow. Channels 5-15 and 35-45 have a very high void fraction, indicating that very small amount of liquid flows through them. It was also observed in the videos that the channels at the ends of the test section have a low void fraction. These channels received very little vapor flow; therefore, any liquid that flowed into those channels tended to remain there or flow very slowly due to strong capillary forces in the microchannels. This effect was observed in both the test sections. It is also observed that the average void fraction is close to 100% for a number of channels. These channels had no flow of liquid through them at all. For a component such as an evaporator or an absorber, this would result in a severe degradation in performance. Test Section 1 did not have any flow redistribution features, leading to the same flow distribution of air and water throughout the length of the microchannel array. The standard deviation of the average void fraction distribution defined in Equation (2.4) is used to quantify the flow maldistribution.

$$\sigma_\alpha = \sqrt{\frac{1}{N_{ch}} \sum_{1}^{N_{ch}} (\alpha_i - \mu_\alpha)^2} \tag{2.4}$$

Figure 2.9 shows the evolution of the flow distribution along the length of Test Section 2. There are four windows through which the flow in the microchannels is visualized. The windows are spaced evenly at 12.7 mm from each other. The visualized microchannel area for each of the four windows is highlighted in red in Figure 2.9. Window 1 displays the 3rd microchannel array, Window 2 displays the 6th, Window 3 displays the 9th, and Window 4 displays the 12th array. Figure 2.9 shows that the presence of mixing zones

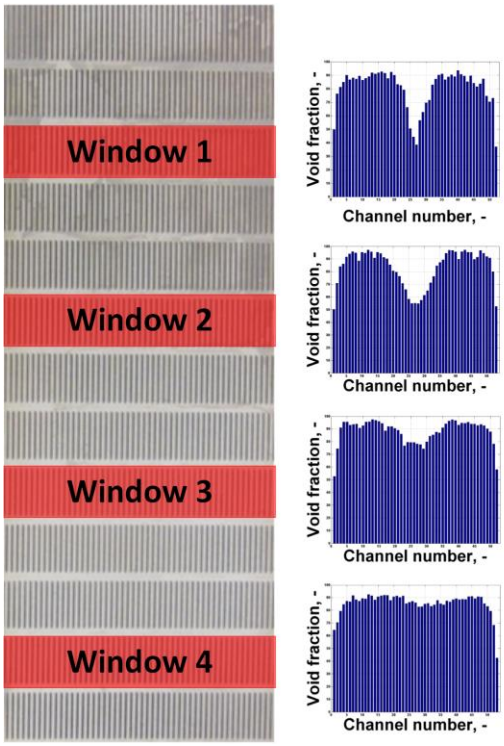

Figure 2.9: Evolution of void fraction distribution with length

significantly improves the void fraction distribution as the flow progresses through the length of the test section. The gas and liquid phases are redistributed through the mixing sections into a more even flow rate of each phase through each channel. As the volumetric flow rates of the two phases through each channel are similar, the void fraction is more evenly distributed among the parallel channels. This is further illustrated by the decreasing standard deviation of the average void fraction along the length of the etched plate, as shown in Figure 2.1.

Figure 2.10 presents the standard deviation of void fraction and its variation with the windows along the length of the test section. The standard deviation value corresponding to window '0' corresponds to Test Section 1. The distribution of gas and liquid remains

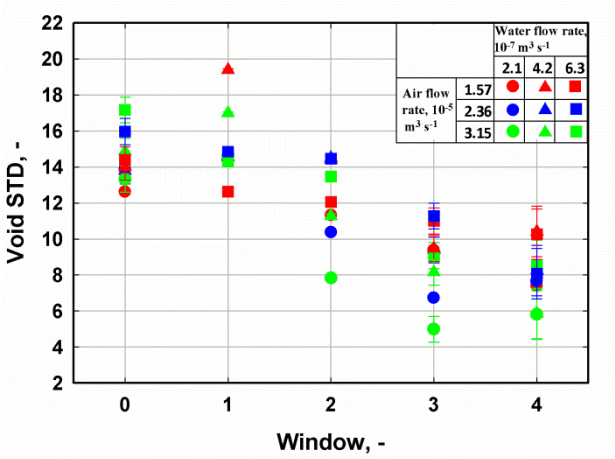

Figure 2.10: Void fraction variation with window

the same throughout Test Section 1. The values from window 1 to 4 represent those observed in Windows 1 to 4 in Test Section 2. The flow is significantly maldistributed in Test Section 1, while the standard deviation decreases monotonically along the length of Test Section 2 for all the investigated flow rates. This indicates that the channel breaks are effective at redistributing the flow for a wide range of qualities and mass fluxes. The channel breaks therefore are effective in achieving considerably uniform flow distribution downstream even when the flow enters with significant maldistribution.

The trends in average void fraction indicate that channel array configurations similar to that of Test Section 2 are more suitable for heat exchanger design. The standard deviation for Test Section 1 is of the same magnitude as that at Window 1 for Test Section 2. However, while the standard deviation is similar, all of the channels received flow in Test Section 2, which was not the case for Test Section 1. Interfacial area intensity in each of these microchannels, which is defined as the interfacial area per unit volume of the channel, was also estimated to better understand this observation. A higher intensity

indicates more mixing between the phases and better distribution. In applications such as an absorber or a desorber, where mass transfer between the vapor and liquid is often the limiting factor, a large interfacial area is favorable. The Canny edge detection algorithm is used to identify the boundaries between air and water. An illustration of the results from the edge detection algorithm is presented in Figure 2.7, where the interfaces between air and water are presented in red.

Figure 2.11 presents the distribution of interfacial area through Test Section 1 at quality 0.081 and mass flux 39.34 kg m^{-2} s^{-1}. The average interfacial area intensity for all channels was calculated to be 6.27×10^{-3} pix pix^{-2} or 914 m^2 m^{-3}. Very low to no liquid flow was observed in some channels, resulting in channels with very little or no interfacial area. This channel arrangement would be very inefficient for components that are limited by mass transfer between gas and liquid phases.

Test Section 2 was observed to have a much higher intensity of interfacial area. The

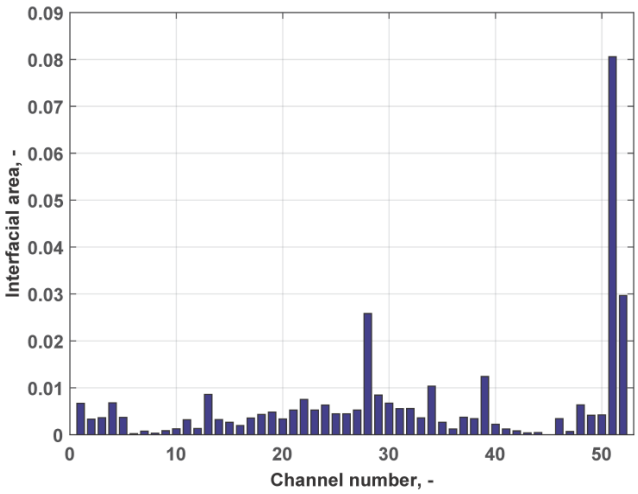

Figure 2.11: Distribution of interfacial area in Test Section 1

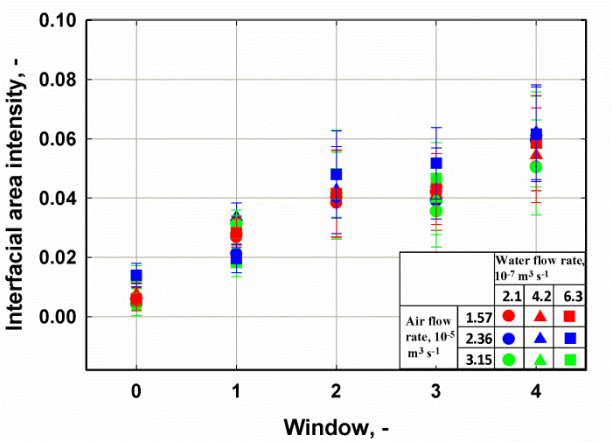

Figure 2.12: Interfacial area intensity variation with window

intensity increases as the flow becomes more evenly distributed. Figure 2.12 plots the intensity of interfacial area and its variation with length for the different flow rates tested. The value at window '0' corresponds to Test Section 1 and the values at Windows 1-4 correspond to those observed in the four viewing windows of Test Section 2. Test Section 1 has a much lower intensity of interfacial area compared to that of Test Section 2. The intensity of Test Section 2 also monotonically increases along the length; this is entirely due to the improving flow distribution of the two phases as the air-water mixture redistributes after each mixing section. Thus, better distribution of the two phases results in a higher intensity of interfacial area across all channels.

There are three major contributors to the improvement in flow distribution with window. Figure 2.13 presents an image of flow through a mixing section in Test Section 2. The predominant cause is pressure gradients across the mixing section. In the initial sections of Test Section 2, liquid flowed predominantly through the center and air through the sides. As flow is distributed from a common header, the pressures at the inlet of each

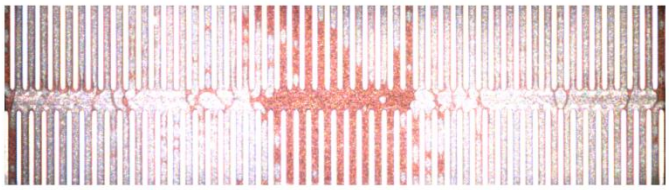

Figure 2.13: Flow across the mixing section

microchannel are approximately equal. The maldistribution of the two phases results in different pressure drops across each channel. The difference in pressure drop across each channel results in a pressure gradient across each mixing section. This pressure gradient results in the redistribution of the two phases among the channels. The flow regime in the channels with liquid was observed to be predominantly slug flow. The pressure was observed to change depending on whether the liquid slug or the air bubble was exiting the channel. The pressure in a gas bubble is higher than the liquid that surrounds it due to surface tension. The pressure of a bubble in slug flow is even greater, as its radius is limited by the microchannel boundary Mehdizadeh *et al.* (2009). The inherent intermittency of slug flow results in the areas of high and low pressure to be different in the mixing section. The mixing section also serves as the distributor to the next array of microchannels. The pressure gradients from one mixing section are observed to affect those in the successive sections.

When pressure drop across the channels in the center with greater liquid flow is higher than those close to the edges, a pressure gradient develops. The pressure in the center of the mixing section is lower than at its edges, resulting in fluid flowing towards the center. As most of the flow away from the center is air, some air is pushed towards the center. In

certain cases, the pressure drop across the channels in the center was lower than that across channels near the edges, which resulted in a pressure gradient forcing liquid towards the edges in the mixing section. Some cases had multiple pressure gradients in the mixing section, forcing liquid and vapor sideways to redistribute. There were instances when liquid exiting a channel into the mixing section is drawn toward the outlet of an adjacent channel. This was caused by the pressure difference between adjacent channels and surface tension between the wall and liquid. Reverse flow in the gas phase was not as evident because it could not be visually verified.

Slug flow was observed to be the predominant flow regime in the channels. As mentioned earlier, the pressure in a gas bubble is higher than in the liquid surrounding it. As these bubbles flow through a channel towards a mixing section, they break up, forcing liquid sideways. The bubble break up is caused as the bubble exits the microchannel section and enters the mixing section. As it enters the mixing section, the diameter of a section of the bubble in the mixing section is enlarged as it is no longer confined by the walls of the channels. The larger diameter of the bubble leads to an imbalance in pressure inside the bubble and the reduced surface tension. This force imbalance causes the bubble to break up and forces the liquid surrounding the bubble sideways.

The channels are also offset as observed in Figure 2.13. The flow from one channel is forced to distribute itself across two channels after the mixing section. The forces of surface tension cause liquid to stick to the walls of the channel at the inlet of the mixing section. This further facilitates a two-phase mixture flowing through one channel to distribute into two adjacent channels downstream.

The experiments were conducted under adiabatic conditions. These geometries are designed for heat exchangers with phase change such as condensers, evaporators, and absorbers. This phase change affects the pressure gradients in the mixing section. While the mixing sections are still expected to help redistribute flow evenly, their performance in diabatic components requires further investigation.

2.4 Absorber performance

As described in previous sections, microchannel heat exchangers are widely used to reduce the footprint of various heat exchangers. Components such as absorbers, condensers, desorbers and evaporators with phase change perform best when the two phases are evenly distributed among all the channels. The effect of phase maldistribution on evaporator and condenser performance has been investigated in the literature. This section investigates the more relevant case of the effect of flow maldistribution on the performance of a microchannel absorber. In a representative case of an absorber for an ammonia-water absorption heat pump, a mixture of ammonia vapor and a dilute solution of ammonia in water enters the absorber. In the absorber, ammonia vapor is absorbed into the dilute solution, resulting in a concentrated solution of ammonia in water, with the heat of absorption rejected to a coupling fluid. The presence of a vapor-liquid mixture increases the possibility of maldistribution in a microchannel absorber.

Void fraction distribution data obtained from the experiments conducted in the present study are used to investigate the effects of a similar flow distribution on the performance of an absorber. The mass flow rate and quality of the two-phase mixture flowing through each channel are derived by assuming a similar void fraction distribution in the

microchannel absorber. Using the individual void fractions measured in each channel along with a void fraction model, the individual flow rates of the two-phases are obtained. Different void fraction models (Kawahara *et al.* (2002); Winkler *et al.* (2012); Keinath and Garimella (2016)) were used to determine individual phase flow rates. The void fraction correlation of Kawahara *et al.* (2002) worked best here as it was developed for air-water mixtures. The other correlations were developed for fluids with lower density ratios and hence were not as accurate. The volumetric quality (β_i) of the refrigerant is obtained using the void fraction correlation presented in Kawahara *et al.* (2002) as shown in Equation (2.5). The mass quality is determined from the volumetric quality.

$$\alpha_i = \left(\frac{0.03\beta_i^{0.5}}{1 - 0.97\beta_i^{0.5}} \right) \tag{2.5}$$

As every channel has the same inlet and outlet header, the pressure drop across each channel should be equal. The pressure drop across each channel is denoted by ΔP_{ch}. This pressure drop is calculated as shown in Equation (2.6).

$$\Delta P_{ch} = \Delta P_{friction,i} + \Delta P_{acceleration,i} + \Delta P_{gravity,i} \tag{2.6}$$

The pressure drop in the channel is the sum of the pressure drop due to friction, decereration, and the gravitational head. Because the flow is downward, the gravitational component has a negative sign.

$$\Delta P_{gravity,i} = -(\alpha_i \rho_G + (1 - \alpha_i)\rho_L) gz \tag{2.7}$$

The frictional and deceleration components of pressure drop are calculated using the framework developed in Garimella *et al.* (2005a). The vapor and liquid mass flow rates at the inlet and outlet of each channel are calculated iteratively using a coupled heat transfer and pressure drop model. The mass flow rate of dilute solution at the inlet of each channel is obtained as a function of the total pressure drop across the channel. The void fraction distribution obtained experimentally is implicit in the pressure drop calculation of each channel. Thus, the phase flow rates through each channel are calculated to have a constant pressure drop across all channels and satisfy the void fraction distribution obtained experimentally.

$$\dot{m}_{L,in,i} = f(\Delta P_{ch}) \tag{2.8}$$

While the pressure drop is not known, the total dilute solution mass flow rate is; therefore, the mass flow rate of liquid through each channel is calculated by iteratively solving the pressure drop framework in Garimella *et al.* (2005a). For simplicity the average quality (obtained from the heat transfer model) through each channel is used to calculate the frictional component of pressure drop. The ammonia vapor mass flow rate is calculated using the inlet channel quality obtained from the coupled heat transfer and pressure drop model.

$$\sum \dot{m}_{L,i} = \dot{m}_{L,total} \tag{2.9}$$

Figure 2.14 presents the distribution of the two-phase mixture through the heat exchanger. The flow rate of the liquid phase is very uneven. It is higher in the channels around the center of the plate and lower away from the center. It can be observed that the vapor flow rate is highest in channels with low dilute solution flow rate and vice versa.

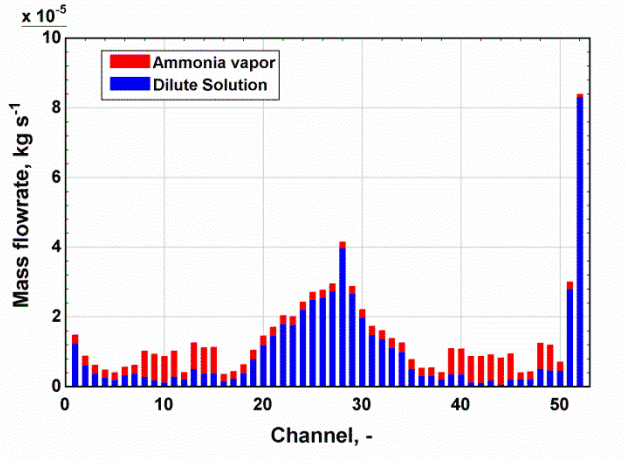

Figure 2.14: Distribution of two-phase mixture in microchannel absorber

This poor mixing of phases in the channels significantly reduces the viability of the microchannel absorber.

2.4.1 Absorber heat transfer model

The representative absorber considered here consists of 26 alternating microchannel plates each with 52 parallel channels. Adjacent plates have a two-phase mixture and water flowing in them. These plates do not incorporate the mixing features introduced in this work. It is assumed that each of the plates has the same flow distribution of phases. The effect of maldistribution on the performance of a microchannel absorber designed for a heat rejection capacity of 5.52 kW is investigated. A two-phase mixture of ammonia vapor and dilute solution that is premixed enters the absorber at a mass flow rate of 0.0094 kg s^{-1}, quality of 0.28, pressure of 501.1 kPa, temperature of 76.68°C and a mass concentration of 0.4831 (ammonia). Water at a temperature of 35°C, flowing in a direction counterflow to the ammonia-water mixture at 0.14 kg s^{-1} is used to cool the

absorber. These conditions are representative of an absorber in an absorption chiller with a cooling capacity of 3.5 kW.

The microchannel absorber is designed such that there is complete absorption of vapor into the dilute solution when the two-phases are evenly distributed. The UA value is calculated such that there is complete absorption in each channel by using the heat transferred in each channel and the log mean temperature difference. The two-phase heat transfer coefficient was calculated to vary between 3800 and 4500 W m^{-2} K^{-1}, while the single-phase heat transfer coefficient is of the order 3800 W m^{-2} K^{-1}. Given the small variation, the UA value is assumed to be constant for all channels for simplicity and the changes in UA due to changes in phase flow rates and mass transfer are neglected.

Mass, species and energy conservation equations are used to analyze the component performance. Mass conservation in each channel is given by Equation (2.10).

$$\dot{m}_{in,i} = \dot{m}_{out,i} \tag{2.10}$$

Species conservation is shown in Equation (2.11).

$$\dot{m}_{in,i} \cdot x_{in,i} = \dot{m}_{out,i} \cdot x_{out,i} \tag{2.11}$$

The zeotropic two-phase mixture requires three properties to determine the state of the solution at the inlet and outlet. The pressure at the inlet is 501.1 kPa, while at the outlet, it is calculated from the pressure drop model. The inlet temperature is known and the bulk solution concentration remains constant in the channel. For the third property at the outlet, Equations (2.12)-(2.14) are solved iteratively for enthalpy at the outlet. The heat transferred to channel ‘i’ on the solution side is presented in Equation (2.12).

$$\dot{m}_{in,i} \cdot h_{ch,in,i} = \dot{m}_{out,i} \cdot h_{ch,out,i} + Q_{ch,i} \tag{2.12}$$

The heat transferred from the corresponding coupling fluid (water) channel is calculated using Equation (2.13).

$$Q_{ch,i} = m_{CF,ch} Cp_{CF} \left(T_{CF,in} - T_{CF,out,i} \right) \tag{2.13}$$

The log mean temperature difference $\Delta T_{LM,i}$ is used as shown in Equation (2.14) to calculate the total heat transferred in the heat exchanger based on the average UA value for each channel.

$$Q_{ch,i} = UA_{avg} \Delta T_{LM,i} \tag{2.14}$$

Figure 2.15 presents the heat transferred in each channel of the absorber. A direct relation is observed between the dilute solution flow rate and the heat transferred in that channel. Channels with higher dilute solution flow rates were able to transfer more heat. The black line across Figure 2.15 represents the heat transferred for the even distribution case. The

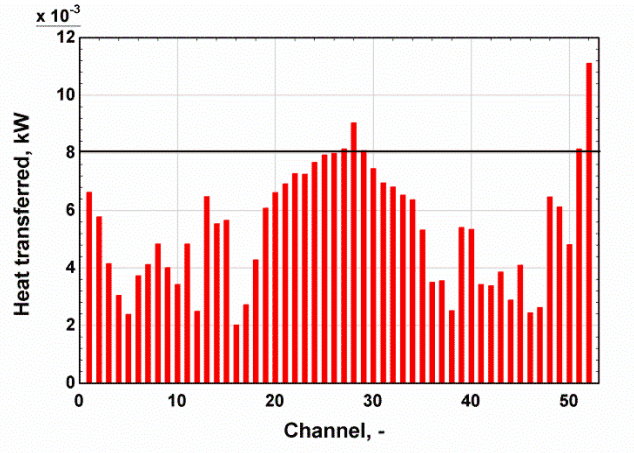

Figure 2.15: Channel wise heat transfer in absorber

total heat transferred from the component for the maldistributed case is 3.62 kW. This compares unfavorably to designed capacity of 5.52 kW, showing significant reduction in capacity due to maldistribution. The mixed outlet temperature and quality were 52.39°C and 0.076, respectively, indicating incomplete absorption. An even distribution of the ammonia-water mixture would yield an outlet temperature of 41.12°C at a subcooled liquid state. This translates to a 34% reduction in heat transferred and a 32% reduction in the mass of ammonia absorbed into the dilute solution. In most heat exchangers, oversizing the component can overcome the limitation due to maldistribution. However, in absorbers, due to the need for mass transfer, such a limitation can only be overcome by inter channel communication through mixing sections and improved distribution headers.

2.5 Conclusions

Two-phase flow through an array of microchannels was visualized. Flow is maldistributed when gas and liquid are distributed among multiple parallel channels. It is shown that conventional microchannels lead to maldistribution. The implementation of mixing sections in the microchannel plate redistributes the flow more evenly. This understanding of maldistribution and the measures to reduce it that are described here could represent a key enabling feature for the implementation of microchannels for a variety of compact phase-change heat and mass exchange components. Using an example of a compact ammonia-water absorption heat pump, maldistribution was shown to adversely affect the performance of microchannel absorbers, and improved communication between channels was shown to be critical for ensuring the desired performance.

CHAPTER 3. TWO-PHASE FLOW IN SERPENTINE MICRO-PIN FIN PASSAGES

3.1 Introduction

Heat exchangers with microscale features have been shown to significantly enhance heat and mass transfer processes over conventional designs, resulting in efficient and compact geometries. Implementation of microchannel heat exchangers, however, poses two key challenges, associated with the maldistribution of each of the phases among the microchannel array, and changes in flow velocities associated with the change in quality of the two-phase flow. Such change in quality is observed in phase-change components such as condensers, evaporators, absorbers, and desorbers. The change in superficial velocities of each phase can change the flow regime from a favorable one to an unfavorable regime. Pin-fin arrays with varying geometry offer the potential to adapt the flow area in a microchannel array to address the challenges posed by the evolving flow characteristics. The use of micro-pin fin arrays in compact heat exchangers with two-phase flow is investigated in this study and its performance is compared with that of microchannel geometries.

Peles *et al.* (2005) investigated the use of circular pin fins for application in heat sinks for MEMS. It was observed that the thermal resistance in micro-pin fins was comparable to that in microchannel geometries. Pressure drop correlations/models for single-phase flow across micro pin-fin arrays have been developed (Kosar *et al.,* 2005; Prasher *et al.,* 2006;

Qu and Siu-Ho, 2008). Kosar *et al.* (2005) present a friction factor and pressure drop correlation for flow of water over staggered and in-line circular/diamond-shaped micro pin fins with a diameter and height of 100 μm. The ratio of the pitch to diameter in the array was 1.5. Their data spanned 5 $< Re_d <$ 110. Qu and Siu-Ho (2008) developed a friction factor and pressure drop correlation for square pin fins for 40 $< Re_d <$ 100. The square pin fins have a 200 × 200 μm cross-section with a height of 670 μm and a pitch of 400 μm. Prasher *et al.* (2006) investigated single-phase pressure drop in circular and square micro pin fins with dimensions ranging from 50 −150 μm. Experiments were conducted using water to yield a correlation that spanned a wide range of Reynolds numbers (5 $< Re_d <$ 1000). (Data from Kosar *et al.* (2005) were also considered while developing the pressure drop correlation for lower *Re*.) Flow over the pin fins was observed to transition from laminar flow at $Re_d \approx 100$.

Nitrogen-water flow across pin fins was investigated by Krishnamurthy and Peles (2007) using high-speed videography. The pin fins had a diameter height of 100 μm, with a pitch-to-diameter ratio of 1.5, and 5 $< Re <$ 50. Four distinct flow regimes, bubbly-slug, gas slug, bridged, and annular flow were observed. Based on these data, they developed models to calculate the void fraction and pressure drop in two-phase flow across pin fins for $Re_d <$ 40.

Krishnamurthy and Peles (2008b) present the effect of pin diameter and pitch on flow regime. Two distinct mechanisms for the formation of bridged flow were observed. In the smaller test section, gas slugs trapping liquid bridges between pin fins was the main mechanism for bridge flow. In the larger test section, the break-up of larger liquid slugs resulted in the formation of liquid bridges. A parameter *K*, defined as the product of the

Weber (*We*) and Euler (*Eu*) numbers, is proposed to predict the stability of the bridge flow: the bridge flow regime is stable at $K << 1$, and unstable as $K \rightarrow 1$.

A pressure drop model for the boiling of water through 200×200 μm square pin fins with a height of 670 μm and a pitch of 400 μm is presented by Qu and Siu-Ho (2009). The single-phase friction factor correlation from Qu and Siu-Ho (2008) in combination with the laminar liquid and vapor Lockhart and Martinelli (1949) two-phase multiplier predicted their data well.

The studies discussed above were on single-phase and adiabatic two- phase flow. Boiling two-phase studies were also considered for using the pin fin geometry as a heat sink for high heat flux applications. Krishnamurthy and Peles (2008a) studied flow boiling in staggered micro-pin fin arrays with a diameter of 100 μm. Their experiments investigated different mass and heat fluxes, ranging from 346 to 794 kg m^{-2} s^{-1} and from 20 to 350 W cm^{-2}, respectively. They developed a superposition model for the heat transfer coefficient. They also conducted a visualization study to develop a flow regime map for flow boiling. McNeil *et al.* (2010) conducted a comparative study on heat transfer and pressure drop for flow boiling between plane channels and channels with inline pin-fins embedded in them. They found that channels with pin-fins performed slightly better than their counterparts in terms of heat transfer coefficient; however, they suffered from a higher pressure drop. McNeil *et al.* (2014) also investigated boiling of water through 1 × 1 × 1 mm square pin fins with a pitch of 2 mm. It was observed that the two-phase frictional pressure drop correlations for tube bundles predicted the frictional pressure drop during boiling most accurately. Reeser *et al.* (2014) investigated flow boiling heat transfer and pressure drop for square micro pin fin inline and staggered arrays. They used HFE-7200

and deionized water as working fluids. The square pin fins had a width and height of 153 and 305 μm, respectively. They developed heat transfer and pressure drop models for the different fluids investigated.

Two-phase flow through a serpentine micro pin-fin geometry is investigated in this work using flow visualization techniques. The performance of the serpentine micro pin-fin geometry is compared to that in microchannels in two-phase flow applications. This comparison highlights the differences in using different microscale features to enhance heat transfer in heat and mass exchangers with multi-phase flow. Additionally, a pressure drop model to predict the pressure drop across a serpentine micro-pin fin geometry is developed. This information is critical to the design of microscale absorbers, condensers, and other components with two-phase flow.

3.2 Experimental setup

The micro-pin fins have a diameter (d) of 350 μm, a depth of 406 μm, a transverse pitch (S_T) of 1651 μm, and longitudinal pitch (S_Y) of 1430 μm. Transverse pitch is the pitch between pin fins in the direction perpendicular to flow, while longitudinal pitch is the pitch in the direction of flow. The dimensions of the micro-pin fins were chosen based on those used in microscale heat and mass exchangers in absorption heat pumps. The serpentine test section has seven ribs that act as baffles. The spacing between consecutive baffles decreases, as it is designed for condensing flows. The test section is fabricated by photo chemical etching of stainless steel 304 sheets. Air-water mixtures are used to simulate two-phase flow through the test section. Flow distribution, void fraction and pressure drop of the two-phase mixture are investigated.

Figure 3.1 shows a schematic of the test facility used in this study. An overview of the instrumentation is presented in Chapter 2. The supply tank is partially filled with distilled water, dyed red and pressurized to 350 kPa using compressed air. The inlet air to the test section is drawn from the top of the pressurized tank, while water is drawn from the bottom. The flow rate of each stream is set using individual flow control valves and measured using the flow meters specified in Table 3.1. The air and water streams are then mixed through a T-section, following which the mixture flows into the inlet port of the test section. The air-water mixture then flows through the test section in a vertically downward direction. At the outlet of the test section, the air-water mixture is collected in a storage tank. A high-speed camera (Photron FASTCAM Ultima 1024 with Nikon Micro-NIKKOR 105 mm lens) is used to record high-speed videos at specific locations along the length of the test section. In addition to flow visualization, the pressure drop across the test section is measured using a differential pressure transducer for each flow condition. The mixture mass quality varied between 0.0044 and 0.308. The mass fluxes through the test section range from 19 to 526 kg m^{-2} s^{-1}. These mass fluxes and qualities represent those seen in ammonia-water microscale absorbers for application in absorption

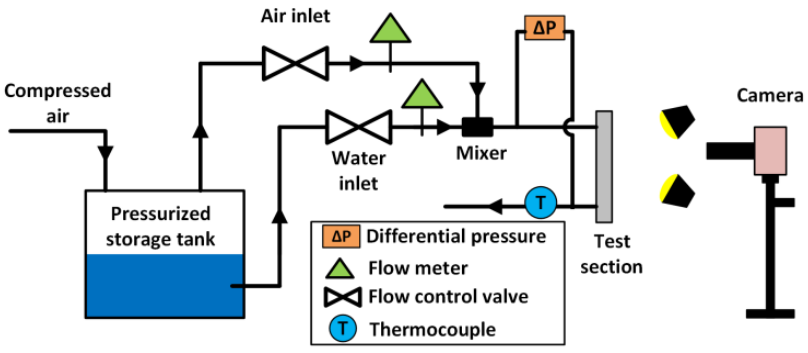

Figure 3.1: Schematic of experimental setup

Table 3.1: : Instrument specifications

Parameter	Instrument	Range	Uncertainty
Inlet Air Volumetric Flow Rate	Rotameter	0.4 – 8.0 $\times 10^{-5}$ $m^3 s^{-1}$	5%
Inlet Water Volumetric Flow Rate	Rotameter	0.2 – 2.6 $\times 10^{-6}$ $m^3 s^{-1}$	4%
Test Section Differential Pressure	Differential Pressure Transducer	0 – 175 kPa	0.245 kPa
Temperature	T-type Thermocouple	3 – 673 K	0.25 K

heat pumps.

Figure 3.2(a) presents an image of the test section used in this study, with a detailed view of the micro pin fins shown in Figure 3.2(b). Seven baffles guide the flow along the component in a serpentine path. The baffles have a thickness of 1.6 mm. The geometry is designed for condensing flow or flow in an absorber, where the quality of the flow decreases from the inlet to the outlet. Hence, the spacing between the baffles is progressively decreased. For flow in an evaporator or desorber, where the flow quality increases, the inlet and outlet can be interchanged such that the cross-sectional area increases from the inlet to the outlet. Details of the micro pin-fin geometry are provided in Figure 3.2(c). The test section is sealed by compressing the etched sheet against a Plexiglas plate using a metal plate as shown in Figure 3.3. The assembly consists of a top

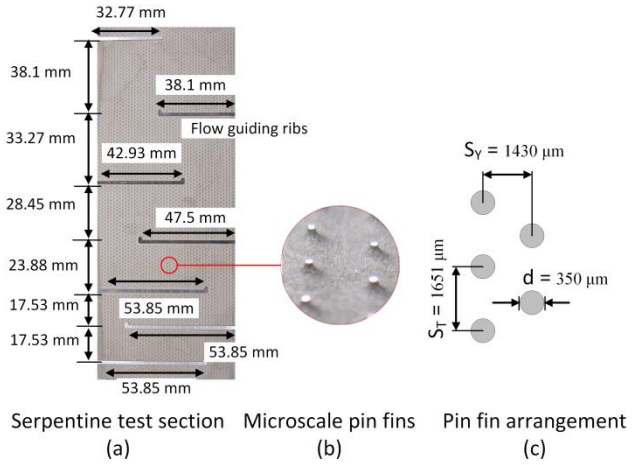

Figure 3.2: Illustration of test section geometry

plate, a Plexiglas plate, two gaskets and a bottom plate. The test section is placed in a slot machined in the bottom plate and sealed by compressing the gaskets around it using the Plexiglas plate. Further details of the assembly are presented in Chapter 2.

3.2.1 Flow visualization

Videos were recorded at 250 frames per second at a shutter speed of 1/1000 second, and a resolution of 1024 × 512 pixels. Flow videos capturing the entire width of the test section are recorded for 4 seconds for each test condition at four different locations along the length, which enables the tracking of changes in flow characteristics along the length. Figure 3.4(a) presents a representative image of the flow in Window 1 at a mass flux of 38.52 kg m^{-2} s^{-1} and a quality of 0.062. Several liquid bridges are observed in the central area of Figure 3.4(a). Similar flow characteristics were also observed in Krishnamurthy and Peles (2007), who referred to it as bridge flow. Water was observed to aggregate around the pin fins and the edges of the shim. At low air flow rates, a bubbly flow regime

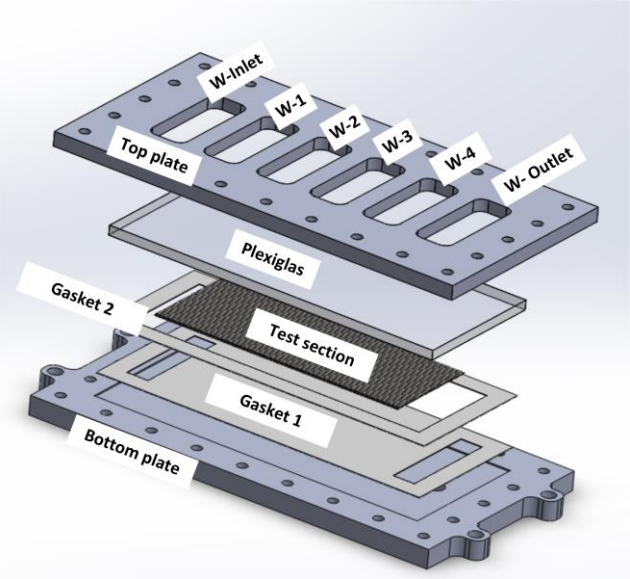

Figure 3.3: Illustration of the test section assembly

was observed, with bubbles smaller than the fin pitch (Figure 3.4(b).) At higher air flow rates, the flow regime transitions to gas-slug flow, where the presence of large bubbles encompassing multiple pins between them is observed (Figure 3.4(c).) The differentiation between bubbly and gas-slug regimes is challenging because both small and large bubbles can be observed at the same time. Therefore, the presence of any large bubbles in the flow indicates gas-slug flow. As the superficial velocity of air increases, the flow transitions to bridge flow (Figure 3.4(d).) At high air and water flow rates, annular flow is observed (Figure 3.4(e).)

3.2.2 Data Reduction

An image analysis tool was developed using MATLAB as part of the work. The tool was custom developed for the serpentine pin fin geometry to process a large number of images in a short period of time. The flow images were rotated and cropped as shown in

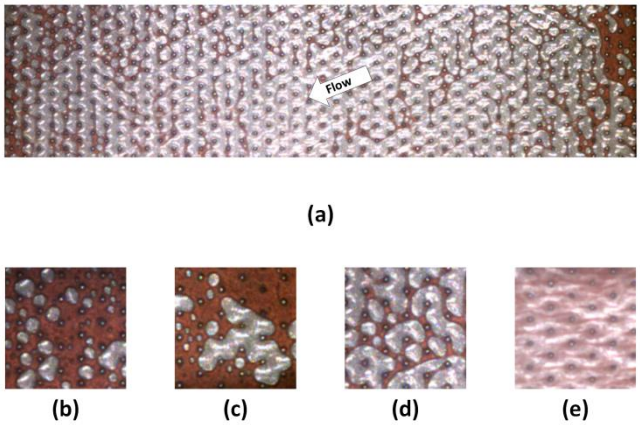

Figure 3.4:Representative image of flow through the test section

Figure 3.4(a). The red regions represent the liquid regions, the dark circles are the microscale pin fins, while the grey regions represent air. These images are converted to an RGB format. The captured images are processed using the algorithm shown in Figure 3.5, which is similar to that used in Chapter 2, but modified to map the pin fins in the present study. Air bubbles often aggregated at the edges and corners of the ribs that guide the flow in the passage, resulting in the inability of taking flow images with only liquid in the test section. Therefore, a 'no flow' image is used to map pins for this test section. A red threshold was used to differentiate between air and water to identify the liquid regions. Once the liquid regions are identified, the image is converted to a binary black and white image with liquid in black and gas in white, as shown in Figure 3.5. This binary image is further processed using a 2-D median filter that removes noise from the image. Figure 3.6 presents a filtered image combined with information about the pin fin locations. The window void fraction is calculated using Equation (3.1). The number of air pixels is divided by the pixels of total area available for flow. The mean window void fraction for each frame in the video is calculated.

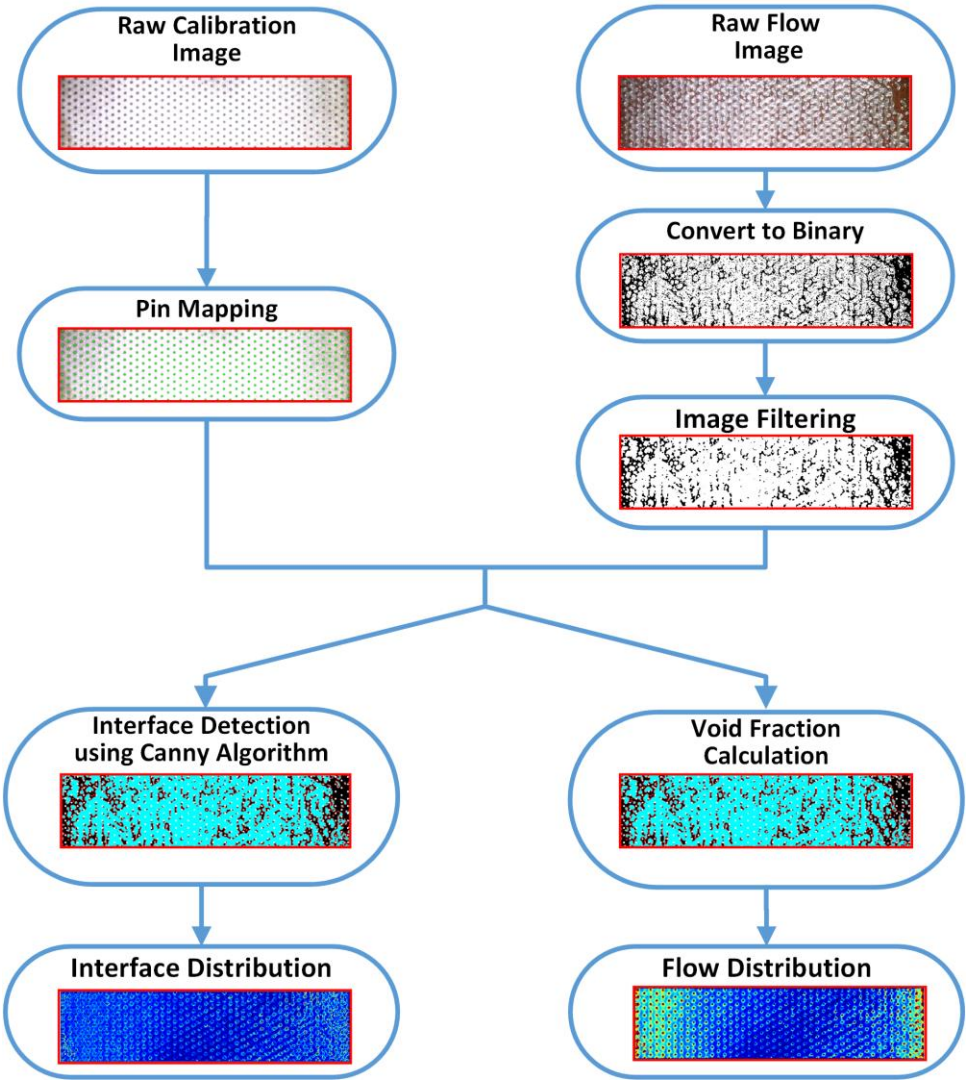

Figure 3.5: Data reduction algorithm for the analysis of flow videos

$$\alpha_{win} = \frac{1}{N_{frames}} \sum_{1}^{N_{frame}} \left(\frac{\sum Pix_{air}}{\sum Pix_{flow\ area}} \right) \tag{3.1}$$

The Canny edge detector is used to identify interfaces between air and water, which are shown in red in Figure 3.6. The curvature of the air-water interface is neglected, and the interface is assumed to be a straight line. This under predicts the total area as the interface will have some curvature due to surface tension. The interfacial area intensity, defined as

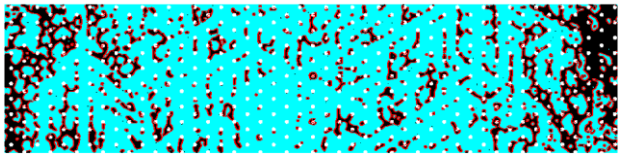

Figure 3.6: Processed image showing interfaces and flow area

the interfacial area per unit volume, is calculated as shown in Equation (3.2) and is the number of interface pixels divided by the total number of pixels. This quantity is proportional to the total interfacial area. These images are further processed to observe the flow distribution and the interface distribution through the serpentine test section.

$$IA_{Intensity} = \frac{1}{N_{frames}} \sum_{1}^{N_{frames}} \left(\frac{\sum Pix_{int}}{\sum Pix_{flow\ area}} \right) \tag{3.2}$$

The uncertainty associated with this analysis is quantified using Equation (3.3). The first two terms account for uncertainty in the red threshold, by observing the change in void fraction for a 10% change in threshold. The third and fourth terms account for the uncertainty due to the wrong identification of a pixel as liquid or air. Equation (3.3) presents the uncertainty in the measurement of void fraction of a channel for a representative data point.

$$\begin{aligned} U_{\alpha_{Flow}} &= \sqrt{\left(\Delta_{\alpha_{Flow},110\%}\right)^2 + \left(\Delta_{\alpha_{Flow},90\%}\right)^2 + \left(\Delta_{\alpha_{Flow},+1}\right)^2 + \left(\Delta_{\alpha_{Flow},-1}\right)^2} \\ U_{\alpha_{Flow}} &= \sqrt{\left(-0.015\right)^2 + \left(0.0184\right)^2 + \left(-4.54\times10^{-6}\right)^2 + \left(4.54\times10^{-6}\right)^2} \\ U_{\alpha_{Flow}} &= 0.0237 \\ \alpha_{Flow} &= 0.736 \pm 0.0237 \end{aligned} \tag{3.3}$$

A similar method is used to calculate the uncertainty in the interfacial area. A sample uncertainty of the interfacial area is shown in Equation (3.4)

$$U_{IA} = \sqrt{\left(\Delta_{IA,110\%}\right)^2 + \left(\Delta_{IA,90\%}\right)^2 + \left(\Delta_{IA,+1}\right)^2 + \left(\Delta_{IA,-1}\right)^2}$$
$$U_{IA} = \sqrt{\left(0.00439\right)^2 + \left(-0.00542\right)^2 + \left(-4.54\times10^{-6}\right)^2 + \left(4.54\times10^{-6}\right)^2} \quad (3.4)$$
$$U_{IA} = 0.00698$$
$$IA_{intensity} = 0.0765 \pm 0.00698$$

3.3 Results and discussion

3.3.1 Flow Regimes, Void Fraction and Interfacial Area

The average void fraction variation does not change significantly along the length, as shown in Figure 3.7. The values of void fraction of each window are within experimental uncertainty and do not show any trends with phase superficial velocities. This measured void fraction is compared with predictions of correlations in the literature (Schrage *et al.*, 1988; Kawahara *et al.*, 2002; Krishnamurthy and Peles, 2007; Winkler *et al.*, 2012), as shown in Figure 3.8. All these correlations predict the measured values with reasonable accuracy. Among these, only Krishnamurthy and Peles (2007) was developed for pin

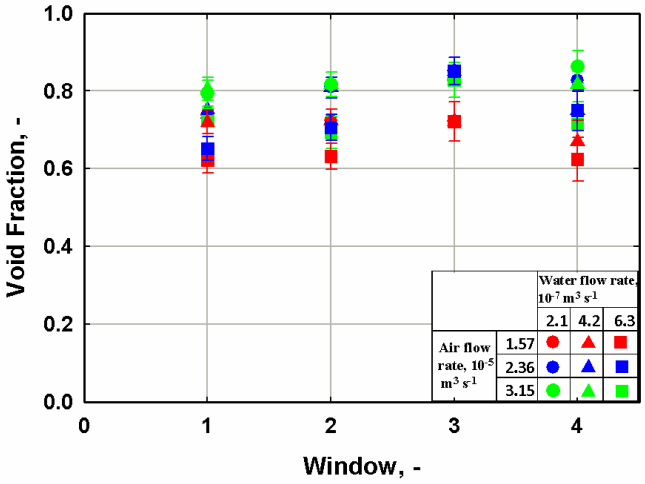

Figure 3.7: Void fraction variation with window

fins. The Kawahara *et al.* (2002) correlation worked the best and predicted all points within an accuracy of 25%. The Winkler *et al.* (2012) correlation is able to predict cases with high void fraction more accurately than those with lower void fraction. The Schrage *et al.* (1988) correlation developed for vertical flow across tube bundles is able to correctly predict trends, but under predicts most values. It should also be noted that this correlation depends on Froude number, which is used when the gravitational force is important. However, gravity has not been observed to influence the flow through microscale geometries such as those under consideration.

Flow maldistribution was observed to be a limiting factor in the microchannel passage

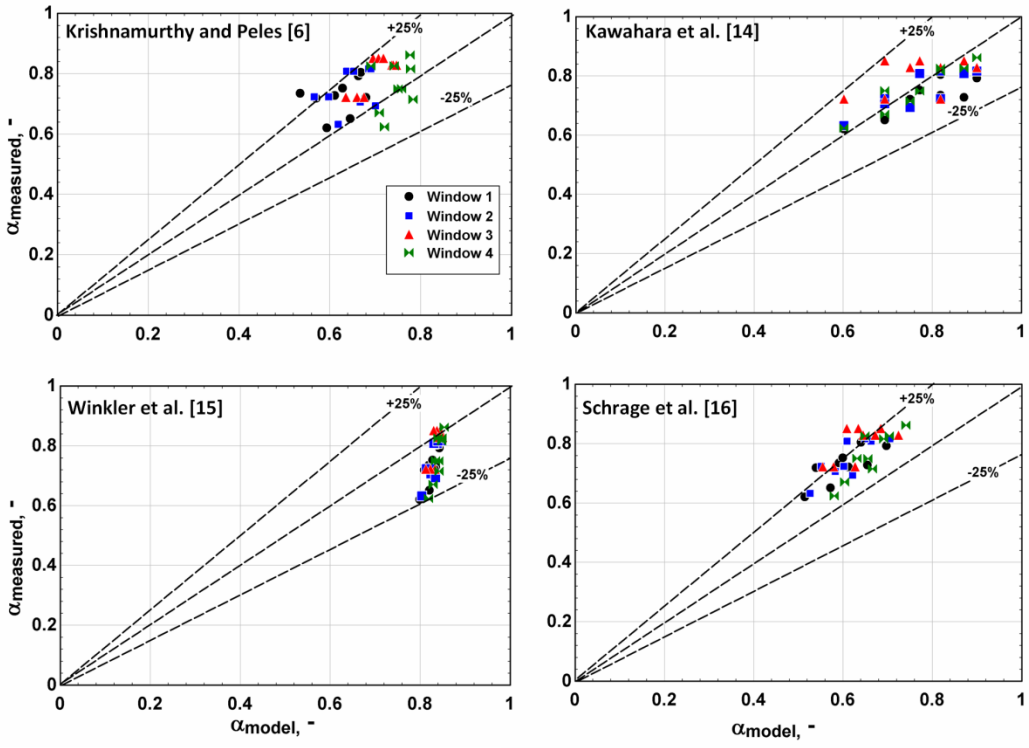

Figure 3.8: Comparison of different void fraction models with measured data

arrays investigated in Chapter 2. Quantifying the flow distribution in the serpentine micro pin fin geometry under consideration here is more challenging. Figure 3.9 presents the time-averaged distribution of liquid in the serpentine section. The flow direction of two-phase is the top right to the bottom left, which is shown in Figure 3.9. Regions with liquid constantly flowing through them are shown in red, while a blue color represents regions with no liquid flow at any time. The edges experience higher liquid flow, while the core areas exhibit higher gas flow. The brightly colored regions around the pins show the liquid aggregated around the pins due to surface forces. A trace of bridge flow is observed where the pins are connected by a bridge-like structure in a highlighted color.

Figure 3.10 presents the distribution of the flow along the length of the test section observed through four different windows for a representative case. As mentioned earlier, the flow area decreases along the test section, because it is designed for condensing flows. The flow area decreases from 9.58×10^{-6} m^2 in the first pass to 4.17×10^{-6} m^2 in the last. As air-water mixtures were used in this study, the superficial velocities of the two phases increase significantly along the serpentine length of the test section. This enables the study of different flow regimes in the different sections of the sheet. It is observed

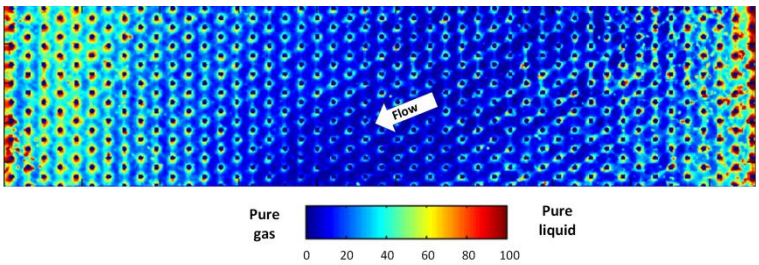

Figure 3.9: Flow distribution through serpentine section

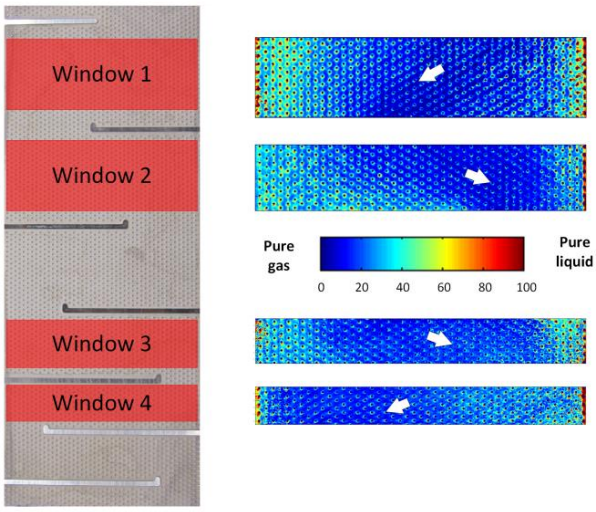

Figure 3.10: Flow distribution along the length of the test section

that all the windows appear to have an air core and liquid flowing close to the edges. Liquid was observed to aggregate around the pin fins in all the sections due to the effects of surface tension.

Interfacial area is critical to accomplish condensation heat and mass transfer. The interfacial area in two microchannel sheet designs investigated in Chapter 2 was observed to increase with improved mixing of the two phases. Figure 3.11 compares interfacial area intensity observed in the present serpentine test section to that observed in the microchannel geometries studied in Chapter 2. Figure 3.11(a) presents the interfacial area intensity in the microchannel test sections. Window '0' corresponds to the shim without mixing features, while Windows 1-4 correspond to values for the microchannel test section with mixing features presented in Chapter 2. It should be noted that all three designs being compared have the same overall width and length. The interfacial area

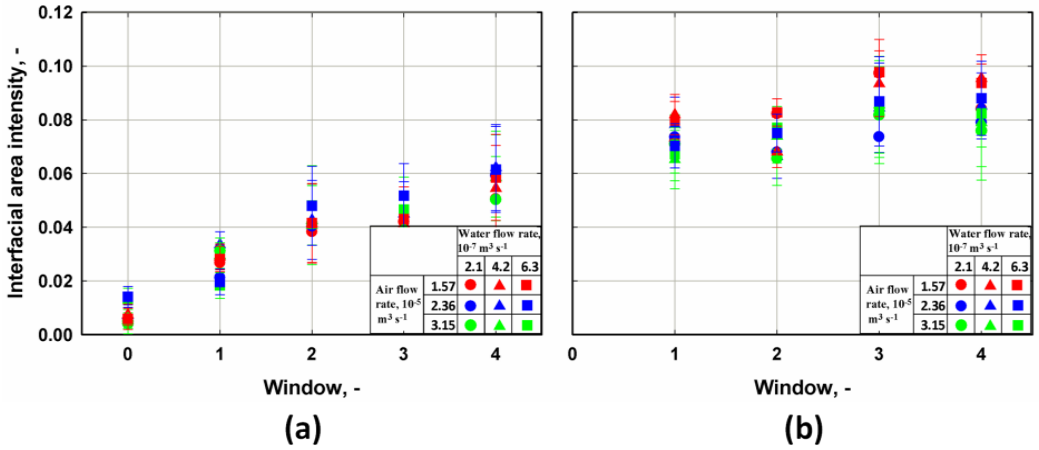

Figure 3.11: Comparison of interfacial area intensity between microchannels and serpentine micro pin-fin geometry

intensity in the serpentine test section is presented in Figure 3.11(b). The interfacial area intensity for the serpentine test section was observed to be much higher than the corresponding value for the microchannel test sections. This indicated that the gas and liquid phases interact more vigorously in the serpentine section than in the microchannel section.

The time averaged distribution of interfacial area is presented in Figure 3.12(a) for the same data set as Figure 3.9. A comparison of Figures 3.9 and 3.12(a) shows that the interfaces between air and water were concentrated in regions with high liquid flow. Liquid aggregation around pins also facilitated mixing between the two phases, as observed in the high concentration of interfaces in regions surrounding pin fins. Interfaces formed in the bridge flow regime were also observed to be significant. As liquid flows away from a bridge structure, it is replenished by liquid flowing towards the bridge. This led to liquid bridges being sustained for long periods as observed in Figure 3.12(a). The presence of some stagnant and slow moving bubbles close to the edges of

the test section led to a high concentration of interfacial area in the region. Such bubbles do not contribute to the improved performance, but highlight the region close to the edges.

Figure 3.12(b) presents the distribution of interface area in Window 4. The section analyzed has a narrow flow area, resulting in higher velocities of air and water in the test section. The flow regime observed in this section is annular flow. Interfacial area is again concentrated in regions with higher liquid flow. Annular flow results in air-water interfaces between pins; unlike bridge flow, these flow regimes have intense mixing between the two phases. This was also observed in Krishnamurthy and Peles (2007). The interfaces in bridges are clearly observed in the time averaged map, as the bridges are constantly replenished and remain in the same location. The interfaces in annular flow are more widely spread and not concentrated in the same location.

3.3.2 Pressure Drop Correlation

Correlations for single-phase pressure drop across micro pin fins have been developed in

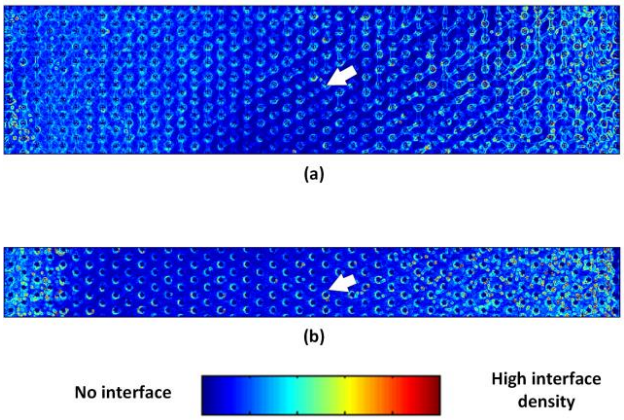

Figure 3.12: Interfacial area distribution through serpentine section

earlier studies. Table 3.2 presents a brief overview of the various geometries investigated in the literature and their applicability. Krishnamurthy and Peles (2007) presented a new two-phase multiplier to predict pressure drop for two-phase flow through micro pin fins. Qu and Siu-Ho (2009) observed that the Lockhart and Martinelli (1949) two-phase multiplier accurately predicted the two-phase pressure drop through pin fins. The other studies presented in Table 3.2 developed correlations to predict the pressure drop in single-phase flow. The liquid and gas Reynolds numbers in the present study varied from 7-198 and 15-424, respectively. The frictional pressure drop across the serpentine test section is calculated as shown in Equation (3.5).

$$\Delta P = \Delta P_{in} + \Delta P_{pin} + \Delta P_{bend} + \Delta P_{gravity} + \Delta P_{out} \tag{3.5}$$

The ΔP_{pin} represents the frictional pressure drop due to two-phase flow through the micro pin-fin arrays. The ΔP_{bend} represents the pressure drop due to the guiding baffles that direct the flow through the serpentine test section, causing a 180° change in the flow direction that accounts for about 3% of total pressure drop. There are seven such bends in

Table 3.2: Pressure drop model comparison

Author	Pin dimensions (μm)	Re range
Krishnamurthy and Peles [6]	d = 100, H = 100, P/d = 1.5	$Re_d < 40$
Qu and Siu-Ho [8]	L_p = 200, H = 670, $S_T/L = 2$, $S_Y/L = 2$	$37 < Re_d < 86$
Prasher et al. [5]	$50 \leq d, L_p \leq 150$, $155 \leq H \leq 310$,	$40 < Re_d < 1000$

the test section with a progressively decreasing flow cross-section. $\Delta P_{gravity}$ is the change in pressure due to gravity. The contribution due to gravity is very small, and accounts for about -1% of total pressure drop. As the flow is downward, this term has a negative value. ΔP_{in} is the frictional pressure loss around micro pin-fins as the flow enters from the inlet port and crosses the first baffle. Similarly, ΔP_{out} accounts for the frictional losses around the micro pin-fins between the last baffle and the outlet port. Losses associated with the expansion and contraction of the two-phase mixture from the inlet port into the inlet header and outlet header to outlet port were observed to be negligible.

Flow between baffles is assumed to be in the horizontal direction. The pressure drop around the baffle is modeled as flow through a 180° pipe bend as modeled by Chisholm (1980). The mass flux is calculated based on the minimum area in the baffle gap. The corresponding single-phase pressure drop is calculated as shown in Equation (3.6), where K_{BL0} is the single-phase loss coefficient for the bend.

$$\Delta P_{L0} = K_{BL0} \frac{G^2}{2\rho_L} \tag{3.6}$$

The two-phase pressure drop is calculated as shown in Equation (3.7).

$$\Delta P_{bend} = \Psi_{L0} \Delta P_{L0} \tag{3.7}$$

Ψ_{L0} is the two-phase multiplier given in Equation (3.8),

$$\Psi_{L0} = 1 + \left(\frac{\rho_L}{\rho_G} - 1 \right) \left[B_{180} x (1 - x) + x^2 \right] \tag{3.8}$$

where *x* is the quality and B is an empirical constant given by Equations (3.9) and (3.10). B_{90} and B_{180} represent the values for 90° and 180° bends. B_{180} is derived from B_{90} as outlined in Chisholm (1980); $K_{BL\,0,90}$ has a value of 0.3.

$$B_{180} = \frac{1 + B_{90}}{2} \tag{3.9}$$

$$B_{90} = 1 + \frac{2.2}{K_{BL\,0,90}\left(2 + R/D\right)} \tag{3.10}$$

The hydraulic diameter for flow around the pin fins is used as the diameter (D) in Equation (3.10). Half the baffle opening length is used as the bend radius (R), which represents the mean radius for all paths along which the flow bends.

The pressure drop due to gravity ($\Delta P_{gravity}$) is calculated as shown in Equation (3.11). The void fraction model from Kawahara *et al.* (2002) is used as it was observed to best predict the measured void fraction in the experiments.

$$\Delta P_{gravity} = -\left[\alpha\rho_g + (1-\alpha)\rho_l\right] gh \tag{3.11}$$

The pressure drop around the micro pin fins is calculated by subtracting $\Delta P_{gravity}$ and ΔP_{bend} from ΔP_{total}. Figure 3.13 presents the contributions of frictional, baffle and gravitational components towards the total pressure drop. The x-axis shows ten selected data points from the test matrix in increasing order of pressure drop. It is observed that the frictional pressure drop for flow through the micro pin-fin array is the dominant contribution. Gravity has a negative contribution as the test section is in a downward flow configuration. The magnitude of the gravitational component is higher at lower qualities due to the higher liquid fraction.

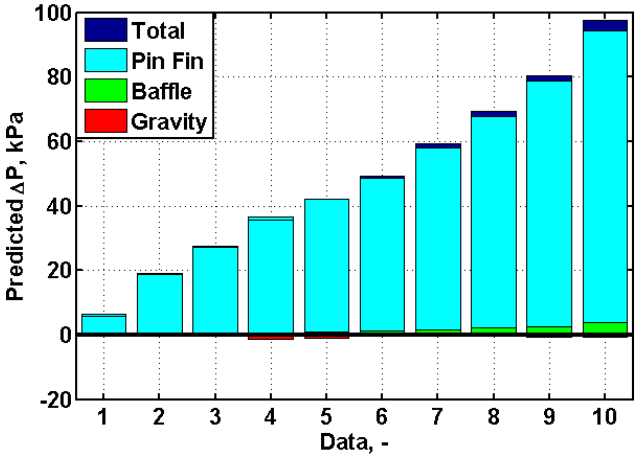

Figure 3.13: Comparison of pressure drop contributions

Model development

The Reynolds number is calculated as shown in Equation (3.12).

$$\mathrm{Re}_d = {Gd_{pin}}/{\mu} \tag{3.12}$$

The mass flux (G) is calculated based on A_{min} as shown in Equation (3.13).

$$G = {\dot{m}}/{A_{\min}} \tag{3.13}$$

A_{min} is the minimum cross-sectional area defined in Equation (3.14).

$$A_{\min} = \frac{S_T - d}{S_T} S_B H \tag{3.14}$$

where S_B is the spacing between the baffles.

The single-phase (liquid) pressure drop is presented in Equation (3.15).

$$\Delta P_{L,pin,i} = f_i \frac{N\left[G_i(1-x)\right]^2}{2\rho_l} \tag{3.15}$$

where *f* is the single-phase Darcy friction factor, and N is number of pin rows in the flow direction.

The pressure drop across the micro pin fins is calculated as shown in Equation (3.16).

$$\Delta P_{pin} = \sum_{i=1}^{N_{baffle}-1} \Phi_{L,i}^2 \Delta P_{L,pin,i} \tag{3.16}$$

where $\Delta P_{L,pin}$ is the single-phase pressure drop around the micro pin fins and Φ_L^2 is the two-phase multiplier. ΔP_{pin} is calculated using Equations (11)-(16). ΔP_{in} is the frictional pressure drop around the pins between the inlet port and the first baffle. ΔP_{out} is the frictional pressure drop around the pins between the last baffle and the outlet port. ΔP_{in} and ΔP_{out} are both calculated using the same method as ΔP_{pin}. The corresponding number of pin rows are N_{pin}, N_{in} and N_{out}. Flow between the baffles is assumed to be in the horizontal direction. N_{pin} is the number of pin rows in the horizontal direction of flow. N_{in} and N_{out} are the number of pin rows in the vertical direction between the inlet and outlet.

The two phase multiplier is calculated as shown in Equation (3.17), where C is a parameter obtained by the regression of the frictional contribution for flow around the micro pin fins based on the overall pressure drop measurements in the test section as described above.

$$\Phi_L^2 = 1 + \frac{C}{X} + \frac{1}{X^2} \tag{3.17}$$

Figure 3.14 presents the comparison of the measured pressure drop data with the various two-phase pressure drop models.

Comparison with the literature

As mentioned earlier, the pressure drop around the pin fins is calculated by subtracting $\Delta P_{gravity}$ and ΔP_{bend} from ΔP_{total}. This pin fin pressure drop is then compared to those in the literature. Krishnamurthy and Peles (2007) used the expression 0.0358×Re to calculate C. This value of C under-predicts the pressure drops from the present study, and leads to a mean absolute error (MAE) of 37.5% as shown in Figure 3.14(a). Qu and Siu-Ho (2009) use a value of 5 for C, which predicts the pressure drop from the present study within a reasonable MAE of 12.5% as shown in Figure 3.14(b), but the model was developed only for cases with Re < 86. The data presented in this work have $Re_L \leq 198$ and $Re_G \leq 424$, which is beyond the range of applicability of their correlation. The Reynolds number for the serpentine geometry increases as the spacing between baffles keeps decreasing along the length of the test section. While the correlation is able to

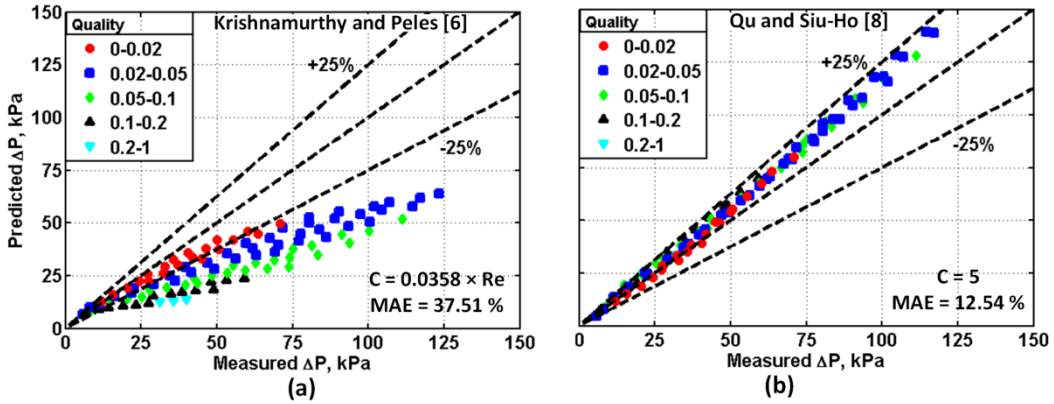

Figure 3.14: Comparison of pressure drop data with the literature

accurately predict the pressure drop of the model, there is a need to develop a method to predict the two-phase pressure drop over a larger range of Reynolds numbers. Of the various friction factor correlations for micro pin fins in the literature, the one developed by Prasher *et al.* (2006) was found to be applicable for Reynolds numbers up to 1000.

Pressure drop model

Based on the above discussion and comparison of the results from the present study with the literature, a regression analysis was performed on the pin-fin portion of the two-phase pressure drop deduced from the measurements to develop a new two-phase multiplier of the form shown in Equation (3.17). The corresponding single-phase pressure drop was calculated using the correlation of Prasher *et al.* (2006). The regression analysis revealed that the pressure drop around the pins was predicted best by a value of 20 for C. Figure 3.15 compares the measured pressure drop with the pressure drop predicted using the developed two-phase multiplier. The MAE for the model is 7.16% indicating a very good agreement with the measured data. Table 3.3 summarizes the pressure drop models used and their predictions. On comparison with a microchannel array with the same footprint, it is observed that the pressure drop through the serpentine test section is 2.7 to 4.1 times higher. The higher pressure drop is due to the increased flow length of the serpentine path that the fluid follows. This higher pressure drop represents the tradeoff required to overcome the limitations due to maldistribution. It should be noted that a heat and mass exchanger with maldistribution will need to be over-sized to compensate for maldistribution, which will in turn increase the pressure drop in the microchannel component as well. The choice of geometry between these two should be assessed based on the design requirements and the penalties of maldistribution.

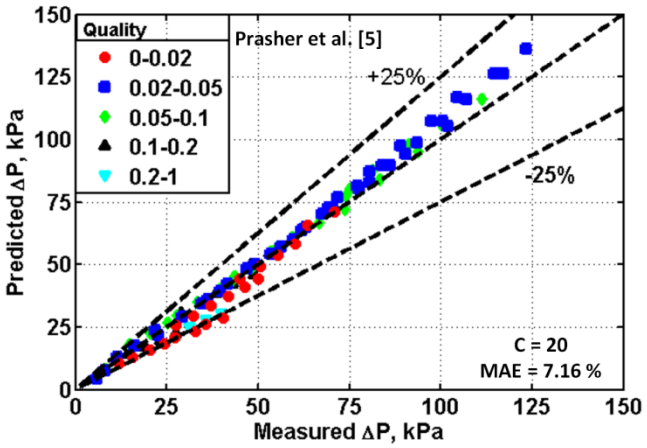

Figure 3.15: Comparison of pressure drop data with model predictions

3.4 Conclusion

Two-phase flow through a serpentine micro-pin fin geometry was visually investigated. The micro pin fins allowed for redistribution of the two phases, resulting in an improved

Table 3.3: Two phase flow pressure drop model evaluation

Authors	**f_{Darcy}**	**C**	**X**	**MAE %**
Krishnamurthy and Peles [6]	$1166.6\,\mathrm{Re}_d^{-1.489}$	0.0358× Re	$\left(\frac{\mu_L}{\mu_G}\right)^{0.745}\left(\frac{1-x}{x}\right)^{0.256}\left(\frac{\rho_G}{\rho_L}\right)^{0.5}$	37.51
Qu and Siu-Ho [8]	$20.09\,\mathrm{Re}_d^{-0.547}$	5	$\left(\frac{\mu_L}{\mu_G}\right)^{0.274}\left(\frac{1-x}{x}\right)^{0.727}\left(\frac{\rho_G}{\rho_L}\right)^{0.5}$	11.44
Prasher et al. [5]	$14\left(\frac{H}{d}\right)^{0.724}\left(\frac{S_Y-d}{d}\right)^{-0.442}\left(\frac{S_T-d}{d}\right)^{-0.245}\mathrm{Re}_d^{-0.58}$	20	$\left(\frac{\mu_L}{\mu_G}\right)^{0.29}\left(\frac{1-x}{x}\right)^{0.71}\left(\frac{\rho_G}{\rho_L}\right)^{0.5}$	**7.16**

flow distribution in the passages. Some maldistribution was still observed in the pin-fin geometry, as the vapor phase was observed to predominantly flow through the center of the test section. The serpentine geometry had higher mixing of the two phases compared to the microchannel design of same size. Hence, it is better suited for components with mass transfer between the two phases. Microchannel void fraction models from the literature were found to accurately predict the void fraction through the test section. The frictional pressure drop through the pin fins was the largest contributor to the overall pressure drop across the serpentine test section. A new method to calculate two-phase pressure drop across a serpentine pin fin geometry was developed. It was observed that a Chisholm parameter of 20 in the two-phase multiplier accurately predicted two-phase pressure drop through the pin fins.

CHAPTER 4. SERPENTINE MICRO-PIN FIN ABSORBER

4.1 Introduction

The performance of an absorption cooling system is strongly influenced by the performance of the absorber, which is referred as the 'bottleneck' of the system in Beutler *et al.* (1996). However, an incomplete understanding of the different phenomena in microscale absorbers is limiting the implementation of such designs. Kang *et al.* (1998) investigated the performance of a plate heat exchanger in bubble mode. The plate had dimensions of 0.389 m length × 0.127 m width × 0.424 m depth. The vapor and liquid were in counter-flow with each other, with offset fin strips on the cooling fluid side to increase heat transfer rates. The models predicted the vapor region to be close to saturation while the liquid regions were subcooled. This showed that in the absence of mass transfer from the vapor to thin films, the mass transfer resistance in the liquid-phase can be a significant detriment to absorber performance. It was also observed that the vapor phase presented the dominant resistance to heat transfer.

Kang *et al.* (2000) investigated the performance of a plate heat exchanger in falling film and bubble mode. Segmental models for both modes of absorption were developed to predict heat and mass transfer rates. It was observed that the plate heat exchanger performed significantly better in bubble mode. The models showed that vapor side presented the dominant heat transfer resistance in the falling-film mode. It was also observed that in bubble mode, the dominant mass transfer resistance was on the liquid side.

Lee *et al.* (2002b) investigated the use of a plate type absorber for ammonia-water absorption cycles. The absorber had dimensions of 0.112 m × 0.264 m × 0.003 m and operated in a counter-flow configuration. The absorber was tested in an open system with an ammonia vapor source and a dilute solution source. Dilute solution concentrations were varied from 0-30 wt% at a constant flow rate of 0.3 kg min^{-1} and a temperature of 20°C. The log mean temperature and concentration differences were used to calculate the heat and mass transfer coefficients. The heat transfer coefficient was observed to increase with vapor and solution flow rates. While the mass transfer coefficient increased with vapor flow rates, it remained relatively constant with an increase in solution flow rates. The same geometry was tested in a falling-film mode in a counter-flow configuration. The performance in the falling-film mode was compared to the bubble mode performance by Lee *et al.* (2002a). The bubble mode was observed to have higher rates of mass transfer, while the falling-film mode had better heat transfer performance. The overall performance of the bubble mode was observed to be better, as more ammonia was absorbed in the bubble mode.

Jenks and Narayanan (2006) investigated the absorption of ammonia-water in a large aspect ratio microchannel using a constrained film design, where a porous plate between the vapor and liquid regions acted as the interface. The use of a porous sheet allowed vapor and liquid to be in a cross-flow arrangement, while the cooling fluid was in a counter-flow arrangement with the solution. The channel was 100 mm long × 20 mm wide × 0.15 mm deep and was tested in a horizontal configuration. Logarithmic mean temperature and concentration differences were used to calculate the overall heat and mass transfer coefficients. It was observed that the overall heat transfer coefficient was

between 400-1200 W m^{-2} K^{-1}. Jenks and Narayanan (2008) investigated the impact of varying channel depth and surface structures on absorption in the same experimental setup. They investigated channels of three depths of 0.15 mm, 0.4 mm and 1.2 mm. It was observed that the 0.4 mm channels had the highest heat transfer coefficients. In the 0.4 mm deep channel, vapor bubbles that encompassed the whole depth limited heat transfer. And in larger channels, a thick liquid layer limited heat transfer. It was also observed that mass transfer coefficient increased with channel depth. It should be noted that these results were for low solution concentrations and only cases with complete absorption were considered.

Cerezo *et al.* (2009) investigated the use of a corrugated plate heat exchanger as an absorber. The inlet and outlet temperatures, pressures and flow rates of all fluids entering and leaving the absorber were measured. The absorber was tested in an open system, where an ammonia tank and dilute solution reservoir supplied the inlet streams to the absorber. This allowed them to precisely control the operating conditions. Logarithmic mean temperature and concentration differences were used to calculate the heat and mass transfer coefficients. An increase in solution flow rate, operating pressure, and cooling fluid flow rates improved absorber performance. However, an increase in dilute solution concentration, dilute solution and cooling fluid temperatures led to lower absorber performance.

Cerezo *et al.* (2010) developed a heat and mass transfer model for the corrugated plate absorber tested in Cerezo *et al.* (2009). The Colburn and Drew (1937) analogy was implemented to model mass transfer using an iterative solver. They assumed spherical bubbles of vapor with constant velocity to model the vapor phase. Initial bubble size was

determined based on the inlet orifice diameter, and the number of bubbles were calculated based on vapor flow rate. Their model predicted the experimental trends well. The heat transfer was predicted with a mean error of 7%, while the mass transfer model had an accuracy of 19%.

The microscale heat and mass exchanger investigated by Nagavarapu and Garimella (2011) was fabricated and tested as an absorber for an ammonia water absorption chiller as reported by Nagavarapu (2012). The microscale features in the absorber included semi-circular microchannel arrays, and inlet and outlet headers to distribute flow through the microscale channels. The absorber was tested as part of a 2.5 kW ammonia-water absorption chiller. The absorber performance did not meet design predictions, which was attributed to three specific issues: complete blockage of some of the microchannels by the braze alloy, partial blockage of microchannels, and flow maldistribution of vapor and liquid among the different channels. It was demonstrated in Chapter 2 that maldistribution of two-phase flow in microchannels is a significant concern for heat and mass transfer phenomena, and can be detrimental to performance. A serpentine micro-pin fin design was proposed in Chapter 3 to overcome issues related to maldistribution. The design uses serpentine passes with decreasing cross-sectional area for condensing flows. It was shown that the interfacial area between the gas and liquid phases in the micro-pin fin design was significantly higher than that in the microchannel array of the same geometric size. This indicated that the serpentine design has the potential to achieve high heat transfer rates while allowing for mixing between the two phases.

The present study investigates an ammonia-water absorber with multiple arrays of micro-pin fins to enhance component performance. Visual data are collected using high-speed photography, and heat transfer measurements are used to better understand the factors governing heat and mass transfer in micro-pin fin geometry. A microscale absorber is fabricated with windows to provide visual access to observe the effect of the microscale features on the flow of the vapor-liquid mixture as absorption takes place, which provides insight into the heat and mass transfer mechanisms in microscale absorbers.

4.2 Test sections

Two test sections, one for flow visualization, and a second for heat transfer experiments, were designed. Figure 4.1(a) shows the design of the serpentine micro-pin fin geometry. The micro-pin fins have a diameter of 580 μm, a transverse pitch of 1320 μm, and a longitudinal pitch of 1520 μm, as shown in Figure 4.1(b). The serpentine test section has seven passes, and a constantly decreasing cross-sectional flow area. The width of first pass is 56.4 mm and that of the seventh pass is 27.43 mm. The decreasing cross section is implemented to maintain high superficial velocities of the two-phase mixture as vapor is being absorbed into the solution. The guiding ribs that define the passes have a width of 1.6 mm, with their lengths based on the cross-sectional flow areas between the two adjacent passes. A second sheet is shown in Figure 4.1(c); this is the sheet through which cooling fluid flows to absorb heat from the serpentine sheet. There are 88 channels in the cooling fluid sheet, and each channel has a semi-circular shape with a channel depth of 0.5 mm and a width of 0.76 mm. The serpentine miro-pin fin sheet is fabricated using a photochemical etching process. In this process, a stainless steel sheet is first cleaned with hydrochloric acid. A template of the geometry is placed on the stainless sheet with

photoresist. The sheet is then exposed to UV light, which hardens the exposed regions of photoresist. The untreated photoresist is then removed and the sheet is then exposed to acid. The acid removes metal from the exposed metal regions, creating the micro-pin fin geometry. The shape of the resulting geometry is very sensitive to the time it is exposed and can result in micro-pin fins with different diameters or a slight conical shape. To account for this, the pin diameter is measured at the top and bottom of the pin fin. The average pin diameter is used for the calculations.

The test section assembly for flow visualization is shown in Figure 4.2(a). The assembly consists of six sheets stacked together to form a single unit of a microscale absorber. The stacked components from top to bottom are the cover sheet, Plexiglas window, gasket, working fluid sheet, cooling fluid sheet and the end sheet. The setup is assembled and the gasket is compressed using screws in each of the through-holes. The fluids enter and exit

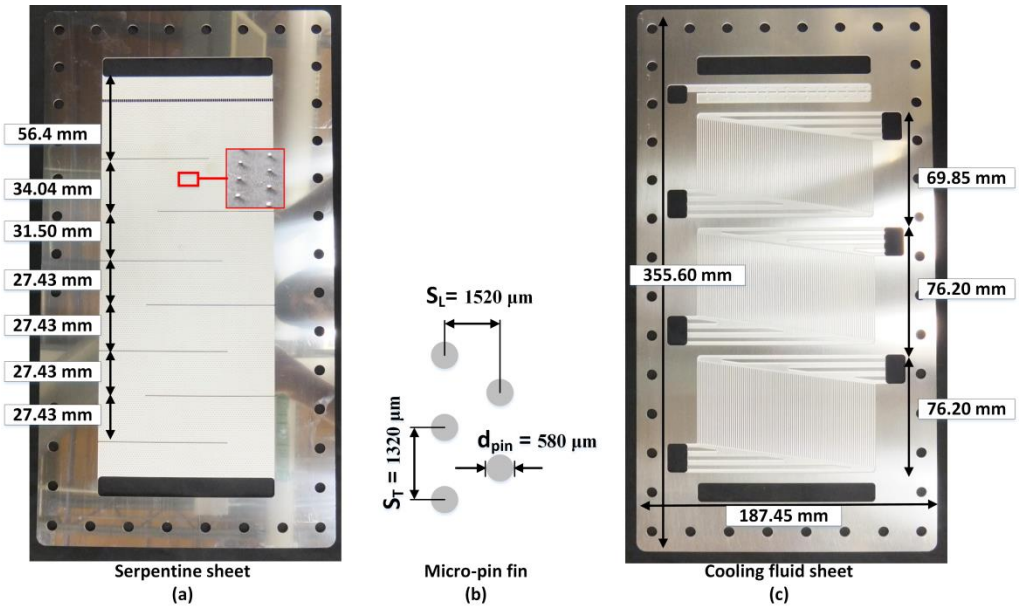

Figure 4.1: Serpentine micro pin fin absorber

the test section through the inlet and outlet ports on the end sheet. The bottom three layers of the absorber, the working fluid sheet, the cooling fluid sheet and the end sheet, are brazed in a separate bonding process. The brazed component has separate pathways for the working fluid and the cooling fluid. The cooling fluid flows counter to the working fluid as it absorbs the heat of absorption. Ammonia vapor and dilute solution flow in the volume between a Plexiglas sheet and the working fluid sheet. The Plexiglas window provides optical access to the flow through the shim. The temperature of the individual ammonia vapor and dilute solution streams are measured at the inlet. The concentrated solution temperature is measured at the outlet.

The test section is placed in a chamber that is pressurized so that the pressure difference between the chamber and the test section is less than 25 kPa. This minimizes the possibility of leaks and decreases the large pressure differentials on the window between its top and bottom surfaces. The pressure chamber is also heated to avoid condensation of

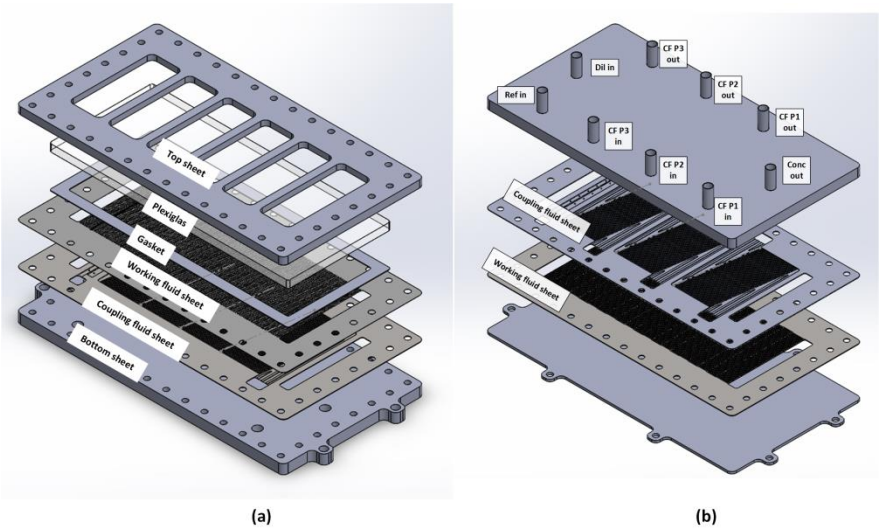

Figure 4.2: Test section assembly

moisture on the windows and to limit parasitic heat loss from the absorber test section to the ambient in the pressure chamber.

The flow visualization tests in this setup enable qualitative assessment of the component, but for more quantitative analysis, intermediate temperature measurements are required. The microscale features on the working fluid and cooling sheets have depths of 0.4 and 0.5 mm. These dimensions make it difficult to obtain reliable temperature measurements using thermocouples. Given these constraints, a separate test section for heat transfer experiments was built as shown in Figure 4.2(b). The test section consists of a single working fluid and cooling fluid sheet sealed between a top and bottom sheet. The cooling fluid sheet is divided into three segments, as shown in Figure 4.3. The temperature of the cooling fluid entering each segment is measured. The intermediate cooling fluid temperatures and segment heat duties are used to validate the heat and mass transfer models.

4.3 Experimental setup

Figure 4.3 presents a schematic of the experimental setup used in this study, which consists of an open ammonia-water loop, and a closed cooling fluid loop. A two-phase mixture of known concentration is prepared by mixing distilled water and ammonia in an adiabatic mixer. A high precision needle valve (Ideal valve model 54-1-11) is used to control the flow rate of water into the absorber. The valve can control flow rates with a precision of 2×10^{-5} kg s^{-1}. An ammonia reservoir is used to supply ammonia vapor into the adiabatic mixer, while another high precision needle valve is used to control the flow rate of ammonia into the adiabatic mixer. A 500 W tape electric heater with a variable

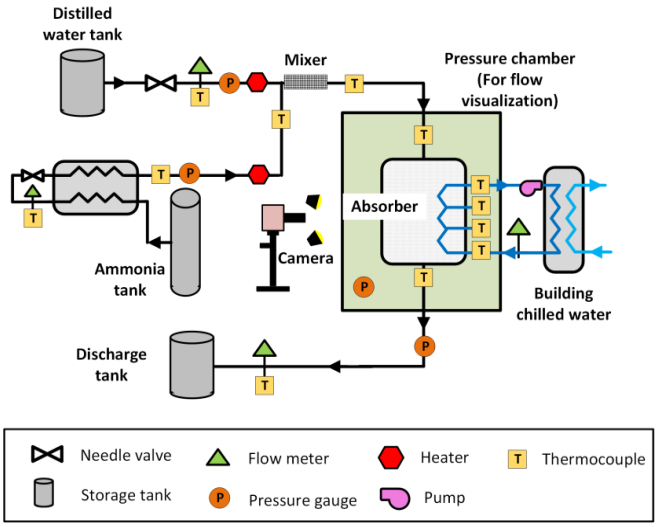

Figure 4.3: Schematic of absorber test facility

load controller is used to heat the water and ammonia streams to the required test conditions. The two-phase mixture then flows into the absorber test section. The temperature of the two-phase mixture is measured at the inlet of the absorber. The ammonia vapor is absorbed into the liquid phase and the mixture exits the absorber as a concentrated ammonia-water solution, where its temperature is measured. The concentrated solution is then discharged into a reservoir. Cooling fluid flows in the counterflow direction in the cooling fluid sheet to remove the heat generated during absorption. For flow visualization tests, the test section is placed in the pressure chamber, which allows the system to operate at the higher pressures of ammonia-water systems. The flow of the two-phase solution is monitored through the Plexiglas windows in the test section. During heat transfer tests, the test section is placed outside the pressure chamber so that it can be insulated to minimize heat losses. The temperature of the cooling fluid is measured at the inlet and outlet of each segment. The intermediate cooling fluid temperatures and segment heat duties are used to validate the heat and mass

transfer models. Distilled water is used as the cooling fluid for the absorber. The mass flow rate is measured using a Rheonik Coriolis-type flow meter (Model: RHM 015; Error: ±0.1%).

A photograph of the test facility is shown in Figure 4.4. The setup is subdivided into two sections: the system block, and the test section. The system block contains all the components to condition the flow, while the test section is placed in the pressure chamber. The cooling fluid is cooled by a separate loop connected to an external chiller to maintain the desired distilled water temperature.

Micro Motion Coriolis-type meters (Model CMFS010M; Error: ±0.4%) are used to measure the concentrated solution and dilute solution flow rates. Three pressure

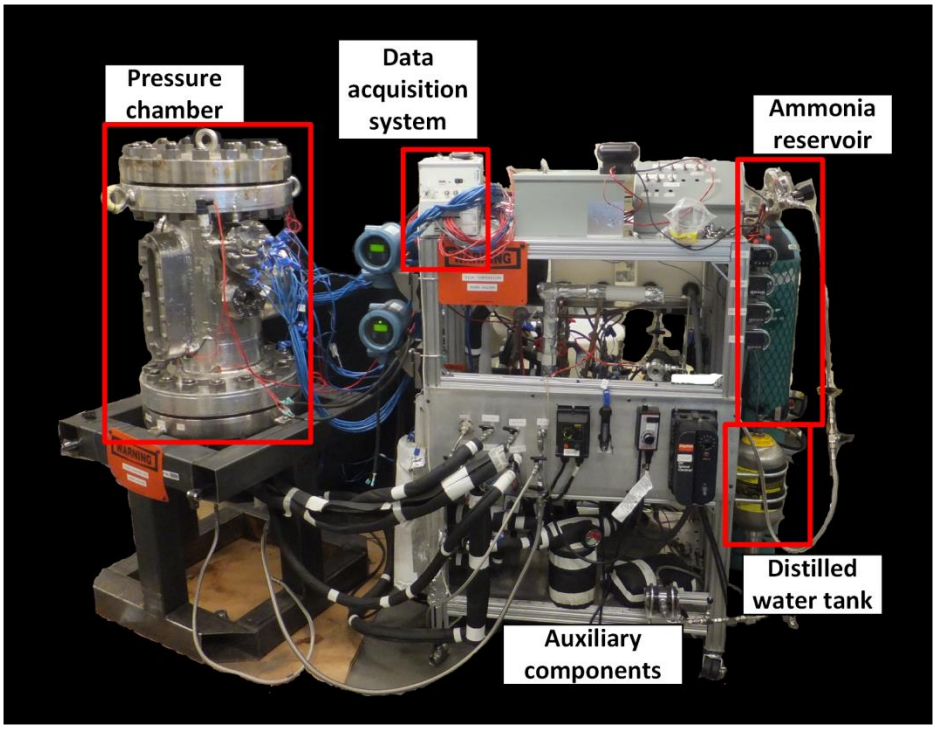

Figure 4.4: Photograph of absorber test facility

transducers are used to measure the pressure of each of the working fluid streams (WIKA Model S-10, ±0.25%). T-type thermocouples (±0.5°C) are used for all temperature measurements. A National Instruments, Model SCXI-1000 data acquisition system is used to record all the measurements.

The serpentine test section is tested across three concentrations, flow rates, and operating pressures, and two cooling fluid temperatures, which helps in understanding the impact of the individual parameters on the process of absorption in micro-pin fin geometries as shown in Table 4.1. On a system level, this corresponds to different operating loads, cooling temperatures and ambient temperatures. The cooling fluid flow rates were kept almost constant correponding to Reynolds numbers between 24 and 31. The cooling fluid flow rates were chosen to meet the somewhat contradictory requirements to keep heat duty uncertainties low, present a low thermal resistance to the overall heat and mass transfer so that the ammonia-water side could be deduced more accurately, and to minimize heat loss. A typical cooling fluid temperature rise (ΔT) across the absorber is about 17°C. The segmental cooling fluid streamwise ΔTs are observed to be 13°C, 3°C and 1°C for the top, middle and bottom segments of the cooling fluid sheet.

4.4 Results and discussion

4.4.1 Flow visualization

A representative image of flow through the micro-pin fin absorber is shown in Figure 4.5. The ammonia-water mixture flows through the third pass from the top left to the bottom right. The representative image in Figure 4.5 has a mass flux of 20.15 kg m^{-2}

Table 4.1: Test Matrix

Cooling Fluid Inlet Temperature (°C) 20/35		Inlet Solution Nominal Concentration								
		42%			47%			52%		
		Flow rate (g s^{-1})			Flow rate (g s^{-1})			Flow rate (g s^{-1})		
		0.15	0.19	0.23	0.15	0.19	0.23	0.15	0.19	0.23
Pressure[kPa]	450	x	x	x	x	x	x	x	x	x
	500	x	x	x	x	x	x	x	x	x
	550	x	x	x	x	x	x	x	x	x

s^{-1} and $Re_{LO}\left(Re_{LO,in} = G_{sol,in}\, d_{pin} / \mu_{L,in}\right)$ of 8.24. The flow regime is predominantly gas-slug flow with distinct vapor and liquid regions. Such high-speed images are captured at four locations along the length of the absorber, as shown in Figure 4.6. The images are processed to enhance the contrast between the vapor and liquid phases. Images at the lower windows are not shown, as the pressure chamber window was not large enough to capture good quality images at the bottom locations. The vapor flow rate decreases from the top to the bottom as it is absorbed; the decreasing superficial velocities result in predominantly gas-slug flow.

A representative image of flow through the microchannel absorber is shown in Figure 4.5. Distinct vapor and liquid regions can be seen. The images are taken for each of the windows and a stitched image of flow through the test section windows is shown in Figure 4.6. A two-phase mixture of ammonia-water enters through the inlet at the top of

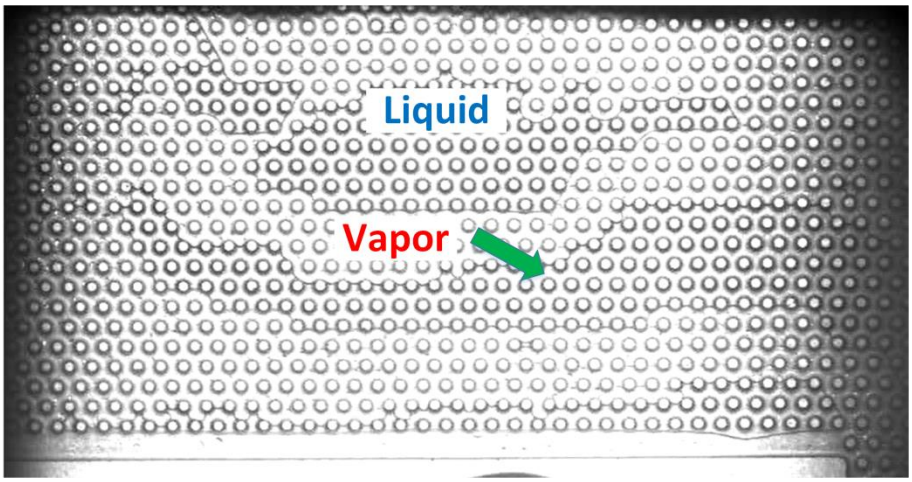

Figure 4.5: Representative image of flow through the test section

the test section. The mixture is assumed to be in equilibrium as a there is an adiabatic mixer positioned just upstream of the inlet to the test section. The vapor flow rate is high at the inlet and decreases toward the outlet as it is absorbed into the liquid. In most cases, the flow regime changes from a bridge flow close to the inlet to gas-slug flow. An illustration of bridge flow is shown in Figure 4.7(a). In the bridge flow regime, the micro-pin fins are connected by liquid bridges and surrounded by a vapor bulk. In the other cases, gas-slug flow is seen throughout the absorber. A schematic of gas-slug flow is shown in Figure 4.7(b). In the gas-slug flow regime, large vapor bubbles and liquid regions flow through the micro-pin fin geometry. The vapor and liquid regions encompass multiple micro-pin fins. Different flow regimes were observed in different regions of the serpentine micro-pin fin test section. At times, attributes of both bridge flow and gas-slug flow are observed. Bridge flow is observed in the center of the test section, along with a large and slow-moving liquid section towards the edges of the test section. The bridge flow regime is more favorable for mass transfer, with better mixed

phases and significantly lower liquid-phase mass transfer resistance. The bridge flow regime also has lower liquid mass transfer resistance, as the liquid regions are thinner and more dispersed. This leads to smaller length scales for mass transfer in the liquid phase. The gas-slug flow had large vapor bubbles flowing through a large liquid bulk, and this flow regime is clearly observed in Windows 3 and 4 of Figure 4.6. These large vapor and liquid regions result in large mass transfer resistances. Because the two phases are not well mixed in this flow regime, vapor has to diffuse from the vapor-liquid interface to the liquid bulk. As diffusion through the liquid phase is slow, it leads to poor mass transfer from the vapor to the liquid.

It was also observed that flow through the test section could be very intermittent in the gas-slug flow regime, with large bubbles flowing through the test section in pulses. This intermittency decreases absorber performance in some cases. These flow visualization results provide qualitative insights into flow regimes, flow distribution, flow intermittency and mixing between the phases. For a more quantitative assessment, heat transfer experiments and numerical studies are conducted.

It was observed that there was a very thin film or no perceptible film between the vapor bubble and top/bottom surface of the absorber in bridge and gas-slug flow regimes. Adiabatic experiments in Chapter 3 also showed the absence of a film on the top and bottom surface in a serpentine micro-pin fin geometry in bridge or gas-slug flow. It is more likely that a very thin film is present in the current diabatic experiments as some vapor will condense on to the surface of the absorber. This film also easily saturated with ammonia and cannot absorb significant quantities of ammonia from the vapor. A schematic of a cross-sectional view is shown in Figure 4.8. It is observed that there are

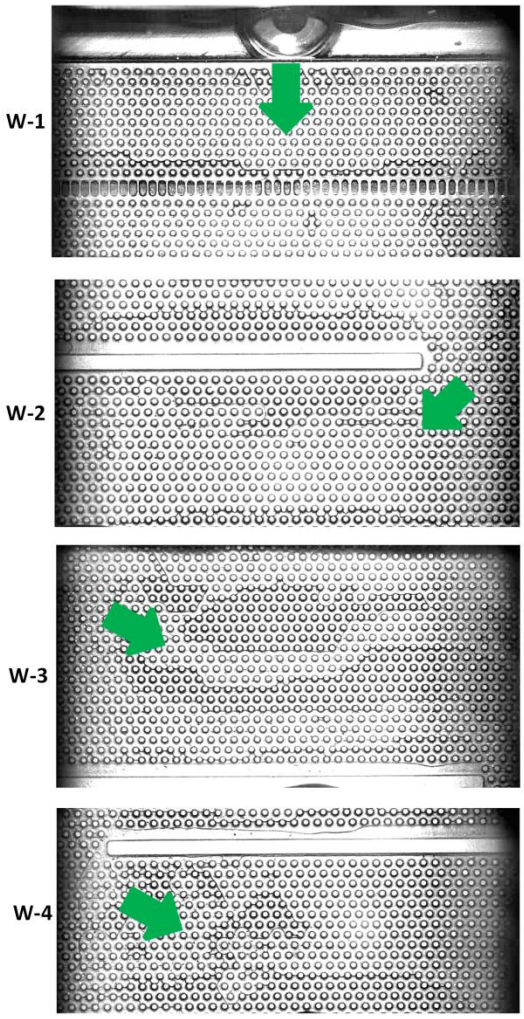

Figure 4.6: Progression of absorption through absorber

horizontal and vertical interfaces in the absorber. There is negligible mass transfer across the thin film on the absorber surface. The major fraction of the mass transfer occurs across the vertical interfaces in the direction of the black arrows shown in Figure 4.8. The thermal energy on the other hand is transferred to the cooling fluid from the absorber sheet shown by the red arrows in Figure 4.8. This observation is critical as prior models have assumed that most of the vapor is absorbed into the thin films between the vapor

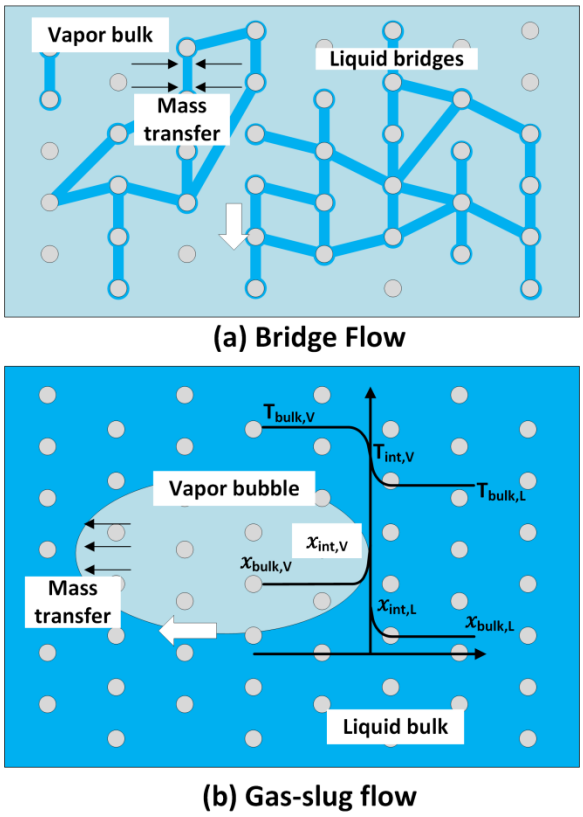

Figure 4.7: Dominant flow regimes through the absorber

and absorber surface. But in micro-pin fin geometries, the major fraction of vapor is absorbed through the interface perpendicular to the absorber surface. Therefore, an accurate estimation of this interfacial area is critical for the development of accurate absorber models.

4.4.2 Heat transfer experiments

A schematic of the absorber is shown in Figure 4.9. Ammonia and water are premixed at the inlet and flow through the absorber. Cooling fluid flows counter to the ammonia-water mixture and the temperature is measured at two intermediate locations. The flow rate of the distilled water and concentrated solution are measured in the test

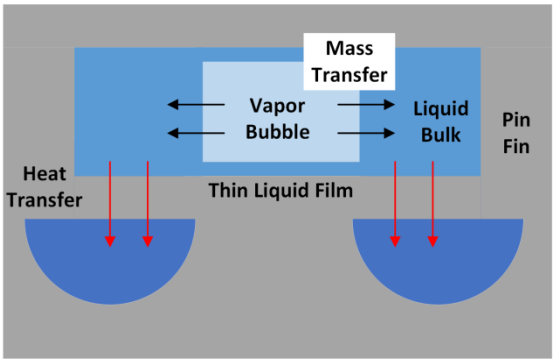

Figure 4.8: Cross-sectional view of the micro-pin fin absorber

facility. Appendix A.1 presents measurements from a sample data point. The flow rate of ammonia into the test section $\dot{m}_A$ is calculated as shown in Equation (4.1):

$$\dot{m}_A = \dot{m}_{abs,in} - \dot{m}_W \tag{4.1}$$

The two-phase mixture flowing into the absorber is assumed to be in equilibrium as it flows through an adiabatic mixer before entering the absorber. The concentration of the mixture at the inlet $x_{abs,in}$ of the absorber is calculated as shown in Equation (4.2). Here, x_A is the concentration of the ammonia stream at 0.999, and x_W is the concentration of the distilled water stream, which is 0.

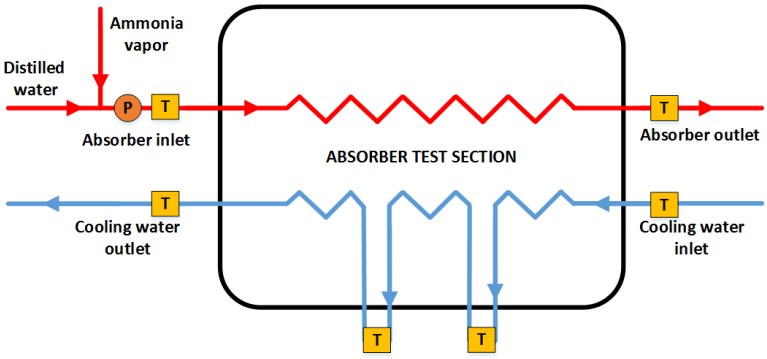

Figure 4.9: Absorber schematic

$$\dot{m}_{abs,in} x_{abs,in} = \dot{m}_A x_A + \dot{m}_W x_W \tag{4.2}$$

Three properties are required to define the state of the mixture. The measured inlet temperature and pressure, along with the concentration calculated in Equation (4.2), are used to calculate the inlet quality as shown in Equation (4.3)

$$q_{abs,in} = f(T_{abs,in}, P_{abs,in}, x_{abs,in}) \tag{4.3}$$

The individual vapor and liquid properties are calculated from the saturated vapor and liquid properties as the two-phase mixture is in equilibrium at the inlet of the component. The inlet liquid concentration is calculated as shown in Equation (4.4).

$$x_{liq,in} = f(T_{abs,in}, P_{abs,in}, q_{liq,in} = 0) \tag{4.4}$$

The inlet vapor concentration is calculated assuming saturated vapor conditions as shown in Equation (4.5).

$$x_{vap,in} = f(T_{abs,in}, P_{abs,in}, q_{vap,in} = 1) \tag{4.5}$$

The heat duty of the absorber is calculated using the measured cooling fluid flow rates and temperatures. The heat transferred through each segment is calculated by summing the heat absorbed by the cooling fluid and the heat lost to the ambient. A sample calculation of the heat loss is presented in Appendix A.2 A representative calculation for a segment is shown in Equation (4.6). The heat loss from each segment is calculated using the thermal resistance diagram shown in Figure 4.10. The heat losses from the top, middle and bottom segments were of the order of 3.3, 1.7 and 1.4 W for an absorber heat duty of 97.8 W. This corresponds to approximately 6.6% of the total absorber heat duty.

$$\dot{Q}_{seg} = \dot{m}_{CF} C_{p,CF} \left(T_{seg,in} - T_{seg,out} \right) + \dot{Q}_{loss,seg} \tag{4.6}$$

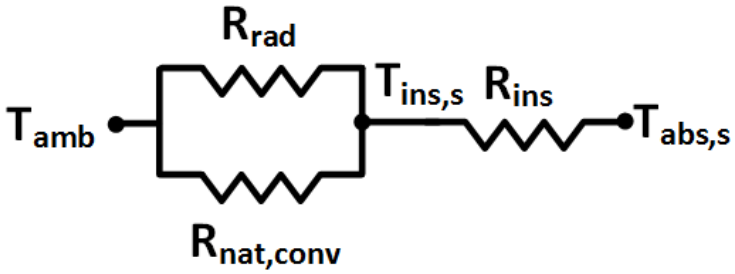

Figure 4.10: Resistance network to calculate heat loss from absorber

The heat transferred in each of the segments is then summed to obtain the total heat transferred in the absorber as shown in Equation (4.7).

$$\dot{Q}_{abs,CF} = \dot{Q}_{seg,top} + \dot{Q}_{seg,mid} + \dot{Q}_{seg,bot} \tag{4.7}$$

The heat transferred in the absorber is also calculated from the solution side as shown in Equation (4.8). In this calculation, it is assumed that the ammonia-water mixture exiting the absorber is in equilibrium.

$$\dot{Q}_{abs,sol} = \dot{m}_{sol,in}\left(h_{sol,in}\left(T_{sol,in}, P_{sol,in}, x_{sol,in}\right) - h_{sol,out}\left(T_{sol,out}, P_{sol,out}, x_{sol,out}\right)\right) \tag{4.8}$$

This method of calculating the absorber heat duty is less accurate than calculating the duty from the cooling fluid temperatures. The assumption of equilibrium conditions at the absorber outlet is not valid if there is incomplete absorption in the absorber. Figure 4.11 shows that the heat transfer values calculated from the two methods are within experimental uncertainties for 80% of the data points. The heat transfer rate calculated from the working fluid side is significantly higher than that calculated on the cooling fluid side for some of the data. This deviation is an indication of a case with incomplete absorption of vapor into the liquid. Under certain conditions, a two-phase mixture of sub-

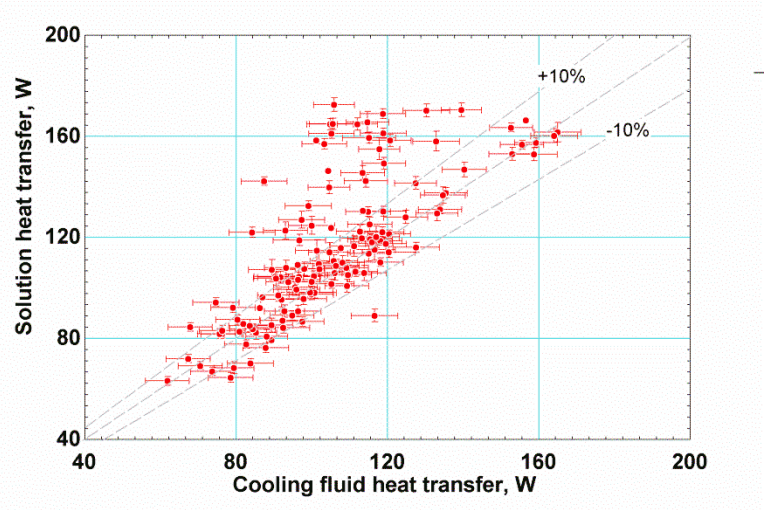

Figure 4.11: Heat transfer rates in the working fluid and cooling fluid

cooled ammonia water solution and superheated ammonia vapor exit the absorber. This indicates that the absorber could be mass transfer limited under certain conditions.

As shown in Figure 4.1, the cooling fluid sheet is divided into three segments, which enables the measurement of the temperature distribution on the cooling fluid side. This temperature distribution can be used to obtain the distribution of heat transfer in the sheet. Figure 4.12 shows the cooling fluid temperature distribution and the segmental heat transfer distribution in the absorber for complete absorption. The solution enters the absorber at a bulk concentration of 0.416, mass flow rate of 0.185 g s^{-1}, pressure of 493 kPa and temperature of 81.3°C. It represents a case where there is complete absorption in the absorber. The Y-axis on the left corresponds to cooling fluid temperatures at the four locations shown. The Y-axis on the right presents the cumulative heat transferred from the working fluid. There is a steep increase in temperature in the top cooling fluid segment; this indicates that most (~71 W) of the heat transfer occurs in the top segment. The heat transferred through the middle and bottom segments is about 21 Wand 6 W,

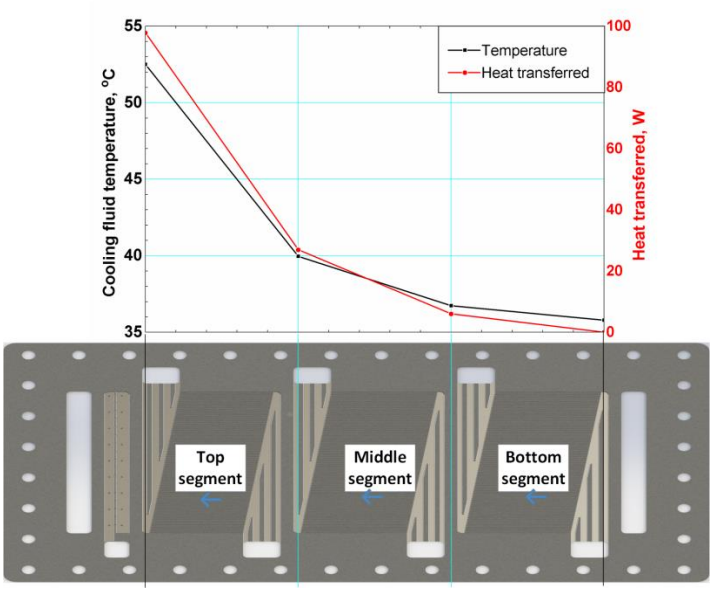

Figure 4.12: Cooling fluid temperature and heat duty distribution in absorber

respectively. This characteristic distribution of heat transfer rate is observed in all tests. As the ammonia water mixture is pre-mixed, it enters at a high temperature at the inlet. The sensible cooling of this mixture results in a high rates of sensible heat transfer and condensation of vapor as temperature drops rapidly. This sensible cooling and condensation of vapor accounts for the large amount of heat transfer in the first segment. This type of distribution is also observed in cases with incomplete absorption, where a two-phase mixture of subcooled liquid and saturated/superheated vapor exits the absorber. This indicates that the absorber has high rates of heat transfer between the solution and the cooling fluid, but is mass transfer limited as subcooled liquid and saturated vapor flow out of the absorber.

The component UA value is calculated as shown in Equation (4.9) from the component heat duty and a logarithmic mean temperature difference.

$$\dot{Q}_{abs,CF} = UA \cdot \Delta T_{LM} \left(T_{sol,in} T_{CF,out}, T_{sol,out}, T_{CF,in} \right) \tag{4.9}$$

The thermal resistance network in the absorber is shown in Figure 4.13. The solution-side thermal resistance is calculated from the *UA* value as shown in Equation (4.10). The heat transfer coefficient is difficult to define in zeotropic mixtures unlike for pure fluids, as there is a large non-linear temperature glide from the inlet to the outlet. Additionally, zeotropic mixture condensation is a combination of heat and mass transfer. Pure fluids use the interface temperature to define a heat transfer coefficient, which is easily measurable, as condensation is isothermal. Given the large temperature glides, the interface temperatures are hard to measure; hence, the actual heat transfer coefficients cannot be calculated. Given these constraints, the measured bulk temperature is used to calculate the heat transfer coefficient. Therefore, an apparent heat transfer coefficient is defined as shown in Equation (4.11). The solution apparent heat transfer coefficient is then calculated as shown in Equation (4.12). The coolant-side thermal resistance is calculated using the heat transfer coefficient for semi-circular channels developed by Sparrow and Haji-Sheikh (1965) and cited in Kakac *et al.* (1987). For the low coolant Reynolds numbers (~27) in this investigation, the Nusselt number is constant with a value 4.08, corresponding to a heat transfer coefficient of ~3600 W m^{-2} K^{-1}. A sample data

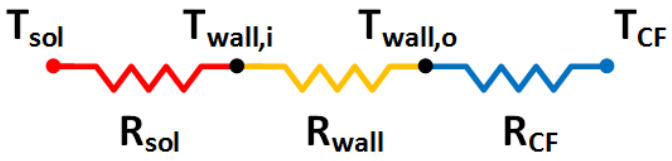

Figure 4.13: Absorber resistance network

reduction is presented in Appendix A.3.

$$R_{sol} = \frac{1}{UA} - R_{wall} - R_{CF} \tag{4.10}$$

$$\alpha'_{abs} = \frac{q''_{abs}}{T_{bulk} - T_w} \tag{4.11}$$

$$\alpha'_{abs} = \frac{1}{R_{sol} A_{serp,ht}} \tag{4.12}$$

Figure 4.14(a) shows that absorber heat duty increases with an increase in the inlet liquid-only Reynolds number and a decrease in cooling fluid temperature. Figure 4.14(b) shows that the solution apparent heat transfer coefficient varies between 150-900 W m^{-2} K^{-1} with the inlet Re_{LO}. The data points that have large uncertainty are those with a really low approach temperature at the absorber outlet (i.e., $T_{sol,out}$ -$T_{CF,in} \leq 0.5$°C). The uncertainty in the measured heat duty is a combination of the uncertainty in the flow meter and thermocouple measurements. For the low coolant Re range under consideration here, the uncertainty in heat duty had a nearly a constant value ~5.5 W. The solution side accounted for 78-91% of the thermal resistance, which resulted in low uncertainties in the apparent heat transfer coefficient. The uncertainty in the apparent heat transfer coefficient varies from 5.5% to 96%, with the average at about 15.2 %. The lowest uncertainties occur for ΔT_{LM} of 15.6°C and $\Delta T_{Approach}$ of 7.5°C, while the highest uncertainties are at a ΔT_{LM} of 7.3°C, corresponding to a $\Delta T_{Approach}$ of 0.3°C.

For a constant cooling fluid temperature, the apparent heat transfer coefficient increases with Reynolds number. There are a few outliers to this trend, but they have large uncertainties. The apparent heat transfer coefficient was observed to be higher at lower cooling fluid temperatures. As the solution is cooled to a lower temperature, the interface temperature decreases, which increases the concentration difference between the interface

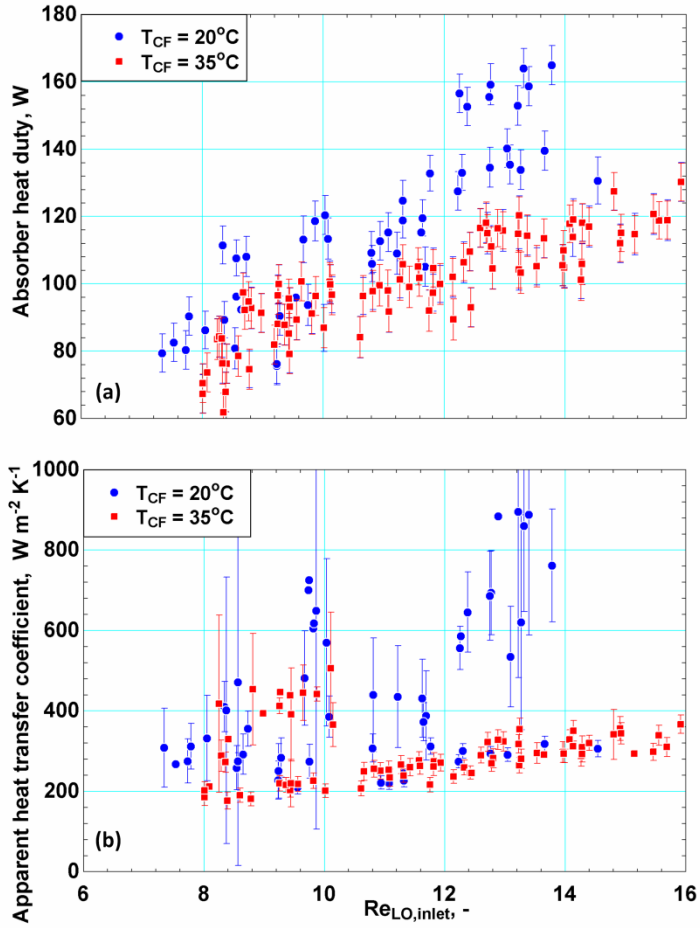

Figure 4.14: Variation of apparent heat transfer coefficient with inlet Reynolds number

and the bulk liquid. This concentration difference is the driving force for mass transfer between the liquid bulk and the interface; hence, as it increases, the rates of mass transfer increases. This increased rate of absorption contributes to the higher apparent heat transfer coefficient at lower Re_{LO}.

Both the vapor and liquid phases exhibit high single-phase heat transfer coefficients due to the small heat transfer length scale. The vapor-phase mass transfer coefficients are expected to be significantly higher than the liquid phase mass transfer coefficients. This

is primarily due to the fact that the diffusion coefficient of ammonia in a vapor is 6.4×10^{-6} m^2 s^{-1} whereas the diffusion coefficient of ammonia in the liquid phase is 4.2×10^{-9} m^2 s^{-1}. The mass transfer length scale was observed to vary depending on the flow regime. The bridge flow regime had a small liquid-phase mass transfer length scale, which would correspond to the thickness of the liquid bridges, which is of the same order of magnitude as the diameter of the micro-pin fin as shown in Figure 4.7(a). The gas-slug flow regime has a significantly larger liquid-phase mass transfer length scale as observed in Figure 4.7(b), corresponding to multiples of the fin pitch. This large length scale implies significant liquid-phase mass transfer resistance in the gas-slug flow regime. These results indicate that the absorber was mass transfer limited but had high rates of heat transfer. Hence, the vapor and liquid are assumed to be in thermal equilibrium at the measured temperature. When the two-phases are in thermal equilibrium and there is poor mass transfer in gas-slug flow regime, in cases with incomplete absorption, the vapor is assumed to be saturated at the outlet. The average enthalpy of the solution outlet is calculated as shown in Equation (4.13)

$$\dot{m}_{sol} h_{sol,out} = \dot{m}_{sol} h_{sol,in} - \dot{Q}_{abs,cf} \tag{4.13}$$

Equations (4.14-4.16) are then solved iteratively to obtain the mass flow rates and individual phase concentrations.

$$\dot{m}_{sol} = \dot{m}_{vap,out} + \dot{m}_{liq,out} \tag{4.14}$$

$$\dot{m}_{sol} x_{sol,out} = \dot{m}_{vap,out} x_{vap,out} + \dot{m}_{liq,out} x_{liq,out} \tag{4.15}$$

$$\dot{m}_{sol} h_{sol,out} = \dot{m}_{vap,out} h_{vap,out}\left(P_{abs,out}, T_{sol,out}, q_{vap,out} = 1\right) + \dot{m}_{liq,out} h_{liq,out}\left(P_{abs,out}, T_{sol,out}, x_{liq,out}\right) \tag{4.16}$$

Two metrics are used to quantify mass transfer rates. The first is an absorption flux, which is defined as the rate of vapor absorbed per unit area. The second is the

absorption intensity, defined as the rate of vapor absorbed per unit fluid volume of the heat exchanger. The absorption flux is a measure of how efficiently the heat exchanger area is utilized, while the absorption intensity is a measure of how efficiently the heat exchanger volume is used. The absorption flux and intensity are highly dependent on operating conditions. For a vapor absorption system, the absorber cooling fluid temperature is typically determined by the ambient conditions and the operating pressure is determined by the chilled water temperature supplied by the evaporator in system. Hence, this parameter is very relevant to compare absorbers designed for compact space-conditioning applications. Figure 4.15 shows the impact of cooling fluid temperature on the rate of absorption. A lower cooling water temperature results in higher rates of absorption. As the liquid interface temperature decreases, the corresponding equilibrium concentration at the liquid interface increases. This increases the concentration difference between the liquid interface and liquid bulk, which is the driving force for absorption into

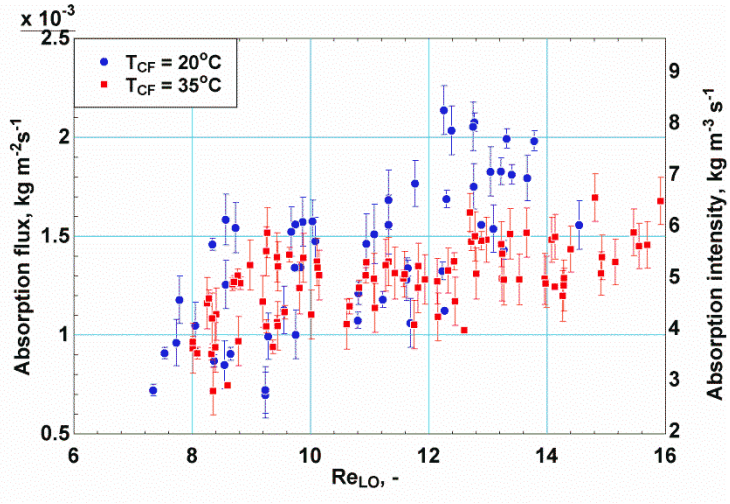

Figure 4.15: Influence of cooling fluid temperature on the rate of absorption

the liquid bulk. In the vapor phase, as the vapor cools, more water is condensed from the vapor bulk to the interface. In the following figures, only the absorption flux is plotted, as the absorption flux and intensity are directly proportional to each other.

Figure 4.16(a) shows that the apparent heat transfer coefficient increases as the pressure decreases. The two-phase mixture at the inlet has a slightly higher quality (10-20%) at a given temperature and concentration at the lower pressure of 450 kPa compared to the 550 kPa (at equilibrium). This higher quality translates to a higher vapor mass flow rate at the inlet. At 450 kPa, the specific volume of vapor is ~0.38 m^3 kg^{-1}, which is about 30% higher than the specific volume at 550 kPa, ~0.3 m^3 kg^{-1}. The higher vapor specific volumes result in higher velocities, which translates to higher heat and mass transfer rates through favorable flow regimes and higher heat and mass transfer coefficients. This increase in heat and mass transfer results in the higher apparent heat transfer coefficients. Figure 4.16(b) shows that the absorption flux increases with a decrease in absorber pressure. The increased vapor velocities are more likely to favor a bridge flow regime in the absorber, resulting in higher liquid mass transfer rates. Higher vapor velocities result in higher vapor mass transfer coefficients. At 450 kPa, the higher vapor specific volume results in higher void fractions, which means that the liquid phase flows through a smaller area, resulting in higher liquid velocities. These higher liquid velocities again contribute to higher mass transfer from the interface to the liquid bulk. At higher pressures, the interface concentration increases by about 0.04 at the same interface temperature, resulting in a higher concentration difference between the interface and the liquid bulk. This counteracts the decrease in mass transfer coefficients due to a lower vapor specific volume. Overall, the impact due to the higher vapor velocities at lower

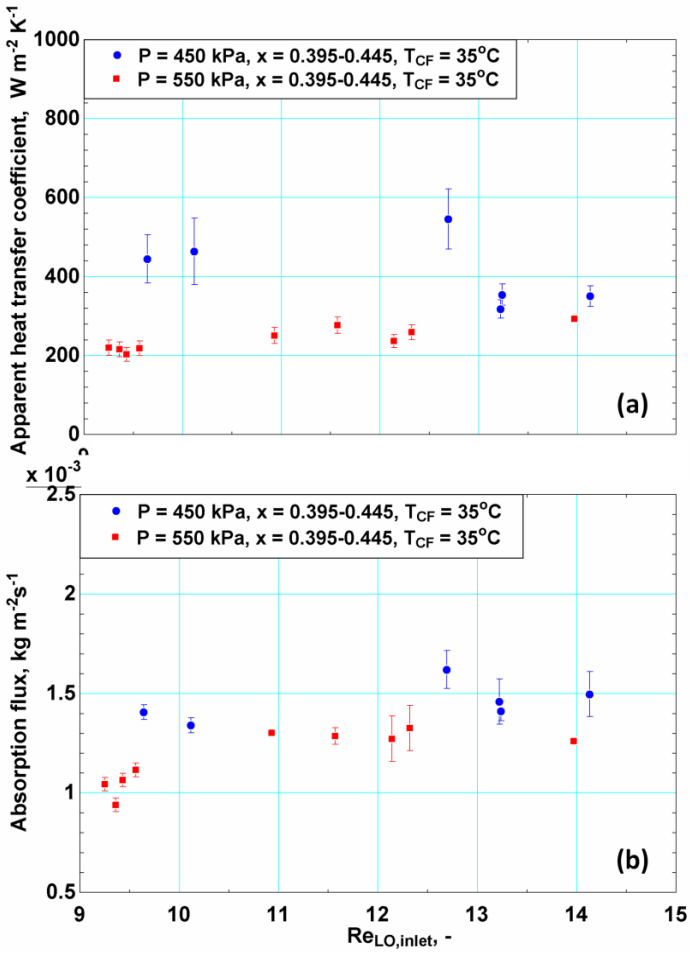

Figure 4.16: Effect of pressure on heat transfer coefficient and absorption flux

pressures is more significant than the increase in the liquid phase interface-to-bulk concentration difference at higher pressures.

Figure 4.17(a) presents shows that the solution bulk concentration does not have a significant effect on the apparent heat transfer coefficients. The absorption flux shown in Figure 4.17(b) is also not significantly affected by the bulk concentration. Both parameters appear to be more dependent on the Reynolds number than concentration. A closer look suggests that there are two counteracting effects that balance each other.

Higher concentrations result in higher vapor flow rates when pre-mixed; these higher vapor flow rates translate to higher vapor velocities, which increase the rates of heat and mass transfer. A higher solution concentration leads to higher liquid bulk concentration, resulting in a lower concentration difference between the interface and the liquid bulk. This decrease in the driving concentration difference results in decreased absorption rates. The decrease in the driving concentration difference (~0.1) is significantly larger than the decrease observed by the increase in absorber pressure (~0.04); therefore, the impact on the absorption rates is significantly higher.

Garimella *et al.* (2016) and Goyal *et al.* (2017) have previously discussed the sensitivity of system performance to the absorber, especially in miniaturized absorption systems. Hence, a model based on the underlying phenomena in absorption processes is needed to enable the development of microscale geometries that could lead to high capacity and COP vapor absorption systems. A new model to predict the absorption of ammonia into a dilute ammonia-water solution in microscale geometries is developed and discussed here.

4.5 Heat and mass transfer model development

Two approaches used to model zeotropic mixture condensation are typically applied to model absorption of ammonia-water mixtures. The first approach, which is typically computationally easier, is the equilibrium approach described by Silver (1947) and Bell and Ghaly (1973). In this approach, the pure component heat transfer coefficient is corrected to account for degradation due to mass transfer. This approach is only applicable if the Lewis number, defined as the ratio of Schmidt and Prandtl

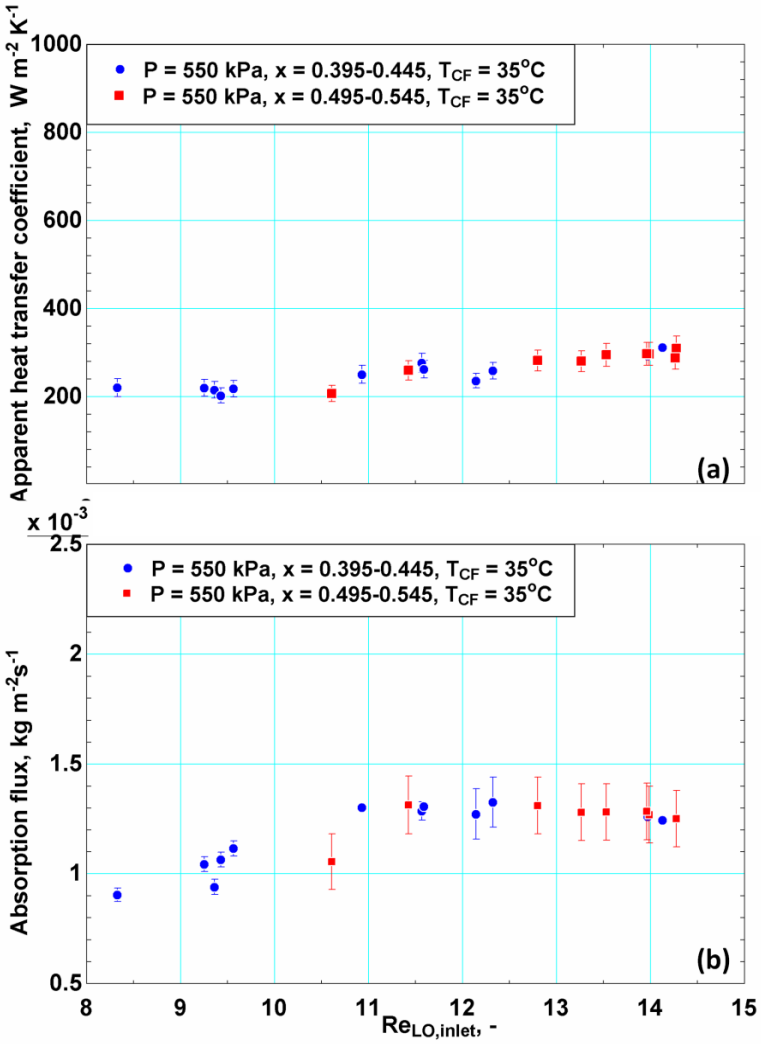

Figure 4.17: Variation of heat transfer coefficient and absorption flux with solution concentration

numbers, is less than 1 or if there is a well-mixed liquid film. The Lewis number for the conditions under consideration is about 20, and the liquid bulk is not well-mixed. Hence, the equilibrium approach is not applicable in this work.

A second approach to modeling the absorber is the non-equilibrium approach. This approach is derived from the mass transfer analyses originally presented by Colburn and Drew (1937) and later adapted by Price and Bell (1974). In this approach, vapor and

liquid interface are assumed to be at equilibrium at the interface, and resistances for heat and mass transfer from the interface to the individual phases are analyzed. The non-equilibrium method was observed to best predict zeotropic mixture condensation of ammonia water mixtures in micro and mini channels by Fronk and Garimella (2016). Therefore, in the present study, the non-equilibrium approach is used for model development.

Figure 4.5 shows a representative flow through the serpentine micro-pin fin absorber. A large vapor bubble is surrounded by large liquid regions, indicating that mass transfer predominantly occurs across the interfaces perpendicular to the plane shown. These high-speed videos of flow aid in the development of the schematic of flow across micro-pin fins shown in Figure 4.7(b). This figure shows a two-phase mixture flowing from right to left, with a vapor bubble surrounded by the liquid bulk. The temperature and concentration gradients in the absorber are also illustrated. The ammonia-water mixture enters the absorber as a two-phase mixture in thermal equilibrium. As the cooling fluid sensibly cools the mixture, water is preferentially absorbed into the mixture, resulting in higher ammonia concentration at the interface. The mixture that is absorbed at the interface has a higher ammonia concentration than the liquid bulk; therefore, there is transfer of ammonia from the interface to the liquid bulk. The temperature is highest in the vapor phase, which then exchanges heat with the interface. The heat is then transferred to the liquid bulk which is cooled by the cooling fluid flowing on the adjacent sheet. A model is developed for the process described above.

It should be noted that mass transfer resistance in the liquid phase is typically neglected in models for absorption. It is assumed the thin liquid films would have low

mass transfer resistance. Flow visualization of absorption in micro-pin fins showed that these films are very thin and cannot absorb much vapor; hence, the major portion of the mass transfer occurs across the interface perpendicular to the absorber sheet.

4.5.1 Segmental Model

The inputs to the model are the inlet two-phase solution state. A cross-sectional view of flow through the micro-pin fin geometry was shown in Figure 4.8. It is assumed that there is a very thin liquid film between the bubble and the sheet surface. Each pass is divided into 20 segments. Two types of segments are used in the model, which change depending on the pass. Examples of the two types of segments are shown in Figure 4.18, where, the flow of the coolant and the working fluid in the first pass is modeled to be in counter flow orientation. Passes two to seven are modeled to be in cross-flow as shown in Figure 4.18. The corresponding resistance diagram for heat and mass transfer is shown in Figure 4.19. Heat is transferred from the vapor to the interface. The vapor-liquid interface is assumed to be in thermal equilibrium with the liquid bulk as the liquid-phase heat transfer coefficients are very high. Heat is then transferred from the liquid phase to the channel wall. The conducted heat across the wall is then absorbed by the cooling fluid flowing in the adjacent sheet. An explicit segmented model is developed where outlet conditions from one segment are the inlet conditions to the next segment.

At the inlet of each segment, the inlet interface liquid and vapor concentrations are determined as shown in Equations (4.17) and (4.18). The segment inlet pressure, interface temperature and a saturation condition are used to determine the properties. The

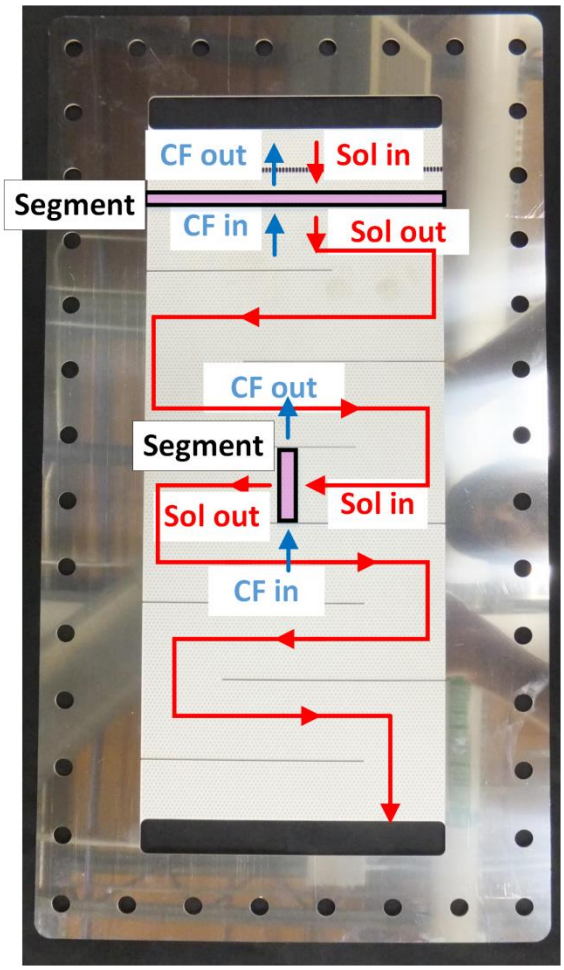

Figure 4.18: Representative absorber segment

interface temperature is assumed to be same as the liquid temperature due to the high rates of heat transfer in the geometry.

$$x_{L,int,in} = f\left(P = P_{seg,in}, T = T_{L,in}, q = 0\right) \tag{4.17}$$

$$x_{v,int,in} = f\left(P = P_{seg,in}, T = T_{L,in}, q = 1\right) \tag{4.18}$$

Once the interface concentrations are known, the mass fluxes from the vapor to the interface are calculated using the framework presented in Price and Bell (1974) as shown in Equation (4.19).

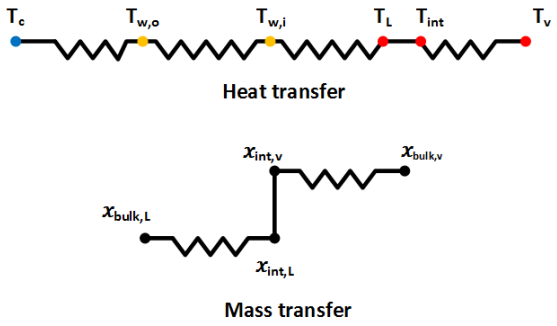

Figure 4.19: Resistance diagram for heat and mass transfer

$$\dot{n}_{\mathrm{T}}'' = \beta_v \times C_{\mathrm{v,T}} \times \ln\left(\frac{\tilde{z} - \tilde{x}_{\mathrm{v,int}}}{\tilde{z} - \tilde{x}_{\mathrm{v,bulk}}}\right) \tag{4.19}$$

where, $\tilde{x}_{v,int}$ is the mole fraction of vapor at the interface, $\tilde{x}_{v,bulk}$ is bulk vapor concentration, $\tilde{z}$ is the mole fraction of the condensing flux, and $C_{\mathrm{v,T}}$ is the bulk concentration. It should be noted all properties are averaged across the inlet and outlet. β_{v} is the vapor-phase mass transfer coefficient, calculated from the heat and mass transfer analogy shown in Equations (4.20) and (4.21).

$$\left(\frac{Sh}{Nu}\right)_v = \left(\frac{Sc}{\mathrm{Pr}}\right)_v^{1/3} \tag{4.20}$$

$$\beta_v = \frac{Sh_v D_{aw,v}}{d_{pin}} \tag{4.21}$$

where $D_{\mathrm{aw,v}}$ is the diffusivity of ammonia in the vapor phase and d_{pin} is the diameter of the pin fin. The Nusselt number (Nu_{v}) is calculated using the correlation for single-phase heat transfer coefficient across micro-pin fins by Prasher *et al.* (2006) shown in Equations (4.22) and (4.23).

$$Nu_{pin} = 0.132\left(\frac{S_T - d_{pin}}{d_{pin}}\right)^{-0.256} \mathrm{Re}^{0.84}\left(\frac{\mathrm{Pr}_f}{\mathrm{Pr}_{water}}\right)^{0.36} \quad \mathrm{Re}<100 \tag{4.22}$$

$$Nu_{pin} = 0.132\left(\frac{S_T - d_{pin}}{d_{pin}}\right)^{-0.63} \mathrm{Re}^{0.73}\left(\frac{\mathrm{Pr}_f}{\mathrm{Pr}_{water}}\right)^{0.36} \quad \mathrm{Re}>100 \tag{4.23}$$

The molar flux from the interface to the liquid bulk is also calculated similarly, as shown in Equation (4.24).

$$\dot{n}_T'' = -\beta_L \times C_{L,T} \times \ln\left(\frac{\tilde{z} - \tilde{x}_{L,\mathrm{int}}}{\tilde{z} - \tilde{x}_{L,bulk}}\right) \tag{4.24}$$

The individual molar fluxes of the condensing ammonia and water are calculated as shown in Equations (4.25) and (4.26). The liquid mass transfer coefficient is also calculated using the heat and mass transfer analogy shown in Equations (4.20) and (4.21)

$$\dot{n}_A'' = \tilde{z} \cdot \dot{n}_T'' \tag{4.25}$$
$$\dot{n}_W'' = (1 - \tilde{z}) \cdot \dot{n}_T'' \tag{4.26}$$

The mass of ammonia and water absorbed into the solution is then calculated as shown in Equations (4.27) and (4.28)

$$\dot{m}_{abs,A} = \dot{n}_A'' \cdot A_{int} \cdot M_A \tag{4.27}$$
$$\dot{m}_{abs,W} = \dot{n}_W'' \cdot A_{int} \cdot M_W \tag{4.28}$$

where M_A and M_W are the molecular masses of ammonia and water. The interfacial area (A_{int}) is estimated from the results presented in Chapter 3, where the average interfacial area intensity was observed to be 1200 m^2 m^{-3} × ε for the test results. Here, ε is the void fraction in passages with the micro-pin fin geometry, calculated using the correlation of Kawahara *et al.* (2002), which was observed to work well for micro-pin fins in Chapter 3. The mass and concentration of vapor leaving the segment are calculated as shown in Equations (4.29) and (4.30).

$$\dot{m}_{v,out} = \dot{m}_{v,in} - \dot{m}_{abs,A} - \dot{m}_{abs,W} \tag{4.29}$$
$$\dot{m}_{v,out} \cdot x_{v,out} = \dot{m}_{v,in} \cdot x_{v,in} - \dot{m}_{abs,A} \tag{4.30}$$

where $x_{v,in}$ and $x_{v,out}$ are the segment inlet and outlet concentrations of ammonia in the vapor phase. Once the outlet vapor mass flow rate and concentration are known, a mass, species and energy balance on the segment is conducted to obtain the liquid outlet properties as shown in Equations (4.31) and (4.32).

$$\dot{m}_{v,out} + \dot{m}_{L,out} = \dot{m}_{v,in} + \dot{m}_{L,in} \tag{4.31}$$

$$\dot{m}_{v,out} \cdot x_{v,out} + \dot{m}_{L,out} \cdot x_{L,out} = \dot{m}_{v,in} \cdot x_{v,in} + \dot{m}_{L,in} \cdot x_{L,in} \tag{4.32}$$

With the liquid concentration state known, the heat released during absorption is calculated as shown in Equation (4.33).

$$\dot{m}_{v,out} \cdot h_{v,out} + \dot{m}_{L,out} \cdot h_{L,out} + \dot{Q}_{abs} = \dot{m}_{v,in} \cdot h_{v,in} + \dot{m}_{L,in} \cdot h_{L,in} \tag{4.33}$$

$\dot{Q}_{abs}$ is heat released by the process of absorption and includes the sensible cooling and heat of absorption. It should be noted that at this point, the outlet vapor and liquid enthalpies are not known. While the outlet pressure and concentration of the two phases are known, a third property is needed to completely define the outlet state. The sensible heat transfer from vapor to the interface is calculated as shown in Equation (4.34).

$$\dot{Q}_v = \alpha_v \left(\frac{\phi}{1 - e^{-\phi}} \right) A_{int} \cdot \Delta T_{LM,v,int} \tag{4.34}$$

where α_v is the vapor heat transfer coefficient and $\Delta T_{LM,v,int}$ is the log mean temperature difference between the vapor and the interface. The term in the parenthesis accounts for mass transfer from the vapor to the interface, and ϕ is defined as shown in Equation (4.35).

$$\phi = \frac{\left(\dot{n}''_A \tilde{c}_{p,A} \right) + \left(\dot{n}''_W \tilde{c}_{p,W} \right)}{\alpha_v} \tag{4.35}$$

where $\tilde{C}_{p,A}$ and $\tilde{C}_{p,W}$ are the molar specific heat capacities of ammonia and water. The sensible heat transfer from the vapor phase can also be calculated as shown in Equation (4.36). The vapor outlet temperature is calculated by solving Equations (4.34) and (4.36).

$$\dot{Q}_v = \dot{m}_v \cdot c_{p,v} \cdot \left(T_{v,in} - T_{v,out}\right) \tag{4.36}$$

An energy balance on the cooling fluid is presented in Equation (4.37). $\dot{Q}_{abs}$ is also calculated from the overall heat transfer coefficient as shown in Equation (4.39). The cooling fluid outlet temperature, liquid outlet temperature and $\dot{Q}_{abs}$ are calculated by iteratively solving Equations (4.33), (4.37) and (4.38).

$$\dot{Q}_{abs} = \dot{m}_{CF} \cdot c_{p,CF} \cdot \left(T_{CF,out} - T_{CF,in}\right) \tag{4.37}$$

$$\dot{Q}_{abs} = \left(U \cdot A\right)_{abs} \cdot \Delta T_{LM,int,CF} \tag{4.38}$$

where U_{abs} is the overall heat transfer coefficient, A_{abs} the overall absorber area and $\Delta T_{\text{LM,int,CF}}$ is the log mean temperature difference between the interface and cooling fluid. The *UA* for the absorber is calculated from the resistance network shown in Equation (4.39).

$$\left(U \cdot A\right)_{abs} = \frac{1}{R_{abs}} = \frac{1}{R_{sol} + R_{wall} + R_{CF}} \tag{4.39}$$

where R_{sol} is the solution-side thermal resistance, R_{wall} is the thermal resistance for conduction across the sheet, and R_{CF} is the cooling fluid resistance. The individual resistances are calculated as shown in Equations (4.40) - (4.42).

$$R_{sol} = \frac{1}{\alpha_{sol} \cdot \left(A_{base} + N_{pin}\eta_{pin}A_{pin}\right)} \tag{4.40}$$

where α_{sol} is the solution-side heat transfer coefficient. The absorber is designed to operate in a vertical configuration. Flow visualization experiments showed that the flow is stratified, hence, the stratified flow correlation from Cavallini *et al.* (2006) is used. A_{base} is the segment base area, N_{pin} is the number of pin fins in the segment, A_{pin} is the pin fin surface area and η_{pin} is the fin efficiency of the pin fin.

$$R_{wall} = \frac{th_{sheet}}{k_{wall} \cdot A_{seg}} \tag{4.41}$$

where th_{sheet} is the thickness of the absorber sheet, k_{wall} is the thermal conductivity of the sheet (stainless steel 304) and A_{seg} is the segmental cross-sectional area.

$$R_{CF} = \frac{1}{\alpha_{CF} \cdot N_{ch} \cdot \left(A_{ch,base} + \eta_{ch,fin} A_{ch,fin} \right)} \tag{4.42}$$

where α_{CF} is the cooling fluid heat transfer coefficient calculated for laminar flow through semi-circular microchannels using the correlation developed by Sparrow and Haji-Sheikh (1965) and cited in Kakac *et al.* (1987). For the laminar flows under consideration, the correlation predicted a Nusselt number of 4.08 and heat transfer coefficient of ~3600 W m^{-2} K^{-1}. N_{ch} is the number of channels in the segment, $A_{ch,base}$ is channel base area, $A_{ch,fin}$ is the fin area and $\eta_{ch,fin}$ is fin efficiency of the channel fin. A sample calculation for one segment of the model is presented in Appendix B. The pressure drop is calculated across every segment as shown in Equations (4.43) - (4.47) and the inlet pressure to the following segment is updated.

$$\Delta P_{seg} = \Delta P_{pin} + \Delta P_{bend} + \Delta P_{gravity} + \Delta P_{dec} \tag{4.43}$$

$$\Delta P_{bend} = \Psi_{L0} K_{BL0} \frac{G^2}{2\rho_L} \tag{4.44}$$

$$\Delta P_{gravity} = -\left[\alpha \rho_g + (1-\alpha) \rho_l \right] gh \tag{4.45}$$

$$\Delta P_{pin,seg} = \Phi_L^2 \Delta P_{L,pin} \tag{4.46}$$

$$\Delta P_{dec} = \frac{G^2}{\rho_{h,out}} - \frac{G^2}{\rho_{h,in}} \tag{4.47}$$

Further details of the pressure drop model used are presented in Chapter 3. The above section describes the heat and mass transfer model for a single segment. The calculated solution outlet conditions are used as the inlet conditions for the successive segment, which continues for all 140 segments. The cooling fluid flow path is more complex. The first pass is assumed to be in counter-flow orientation, while the rest of the passes are assumed to be in crossflow. For the segments in counterflow, the cooling fluid outlet state is directly used as the inlet for the successive segment. In case of the cross-flow passes, the cooling fluid temperature distribution at the outlet of one pass is used as the temperature distribution at the inlet of the successive pass.

4.6 Model results

The temperature profiles of the vapor bulk, interface, liquid bulk and cooling fluid along the absorber are shown in Figure 4.20 for a case with a bulk concentration of 0.42, inlet pressure of 493 kPa, inlet temperature of 80°C and inlet coolant temperature of 35°C. Each pass has 20 segments; hence, there are discontinuities in cooling fluid temperature after every 20 segments. The x-axis presents the 140 segments that account for the seven passes in the absorber. There is a steep temperature gradient in the first few segments as the solution is cooled from a high inlet temperature of ~ 80°C. This results in significant heat transfer in the first pass of the absorber. The vapor temperature is higher than the interface temperature in the initial segments and then decreases to the same temperature as the liquid. This shows that heat transfer rates between the two phases are high. The

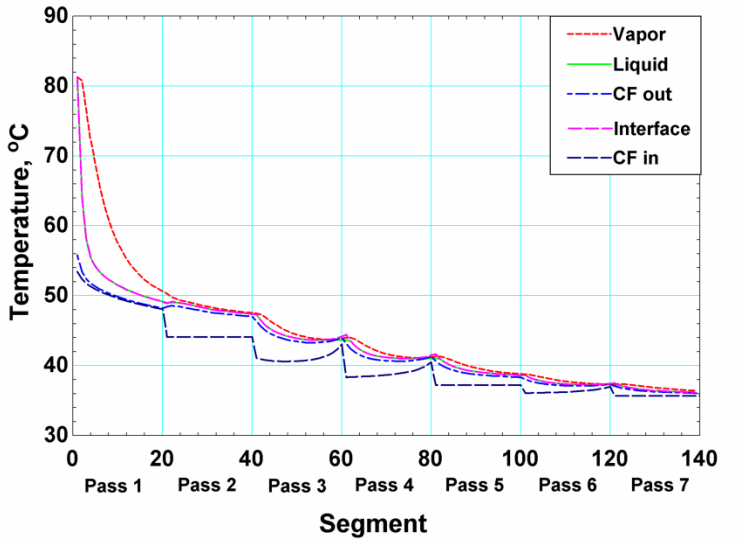

Figure 4.20: Temperature profile in absorber

discontinuous and unique profiles for cooling fluid temperatures are a result of serpentine path of the absorber and each discontinuity corresponds to a new pass. This is a direct result of the cross-flow geometry in each of the passes.

The concentration profiles of the vapor, vapor interface, liquid, liquid interface, and the concentration of the condensing flux (z) in the absorber are plotted in Figure 4.21. The concentration of the condensing flux increases along the length of the absorber from 0.56 to toward 1 as water preferentially condenses from the vapor as it is cooled. Once the water condenses out of the vapor phase, the vapor and vapor interface concentration are both close to unity. This indicates that while there is some vapor mass transfer resistance initially, it decreases after two passes once the vapor bulk and interface concentrations are close to each other. This shows that in the latter passes of the absorber, the vapor is close to saturation conditions. The liquid bulk concentration is significantly lower than the liquid interface concentration as the liquid phase has high heat transfer rates, but has a

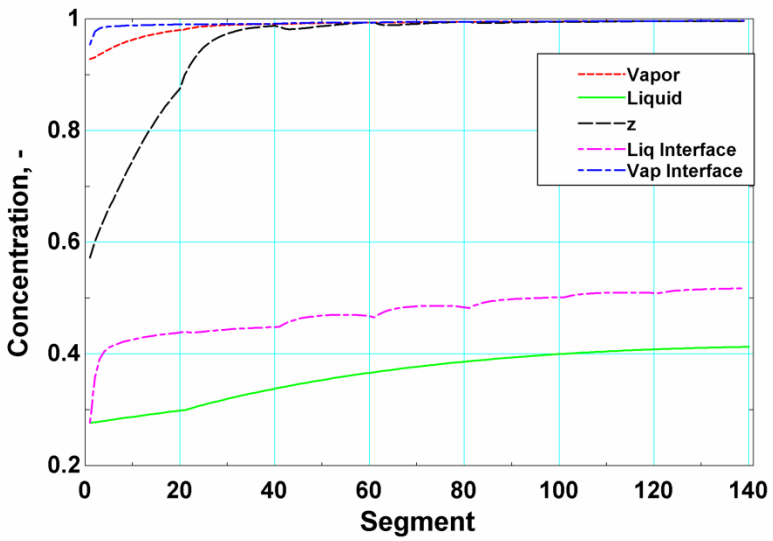

Figure 4.21: Concentration profile in absorber

high mass transfer resistance. This high mass transfer resistance is due to lower diffusivity of ammonia in the liquid phase (4.2×10^{-9} m^2 s^{-1}) compared to the gas phase (6.4×10^{-6} m^2 s^{-1}), and low circulation velocities in the liquid phase. The high mass transfer resistance results in the liquid phase being in a subcooled state, while the interface is in a saturated phase. Unlike the vapor phase, the liquid region continues to be subcooled throughout the absorber due to the high mass transfer resistance in the liquid phase. The intermittency in concentration profiles after every 20 segments corresponds to a change in pass in the serpentine flow geometry.

Figure 4.22 presents the rates of heat and mass transfer in the absorber. The heat transfer from the solution bulk to the cooling fluid is shown in red. High rates of heat transfer are observed in the first few segments, which then decreases after the first two passes. The absorption rate follows a similar trend where it is very high in the first two passes in which the temperature decreases rapidly, followed by a more gradual decrease. It is also

observed that the absorption rate spikes at the inlet of every pass before it gradually decreases. As the solution flows from one pass to the other, the cooling fluid temperature drops to a lower value, leading to a higher temperature difference between the solution and the cooling fluid. Also, when the solution flows from one pass to another, the cross-sectional area decreases, resulting higher vapor and liquid velocities, which lead to higher heat and mass transfer rates. The segmental heat duty also follows a similar trend where there is a spike in temperature at the inlet of each pass. This spike corresponds to the sudden drop in cooling fluid temperature at the inlet of the next pass. The rates of absorption and heat transfer are dependent on each other as the segments with high rates of heat transfer typically have high absorption rates too. The sensible heat transfer from the vapor bulk to the interface is also plotted in Figure 4.22. Sensible heat transfer from the vapor phase to the interface is much lower than the total heat transferred to the coolant and decreases to almost zero after the first pass. This coincides with the vapor

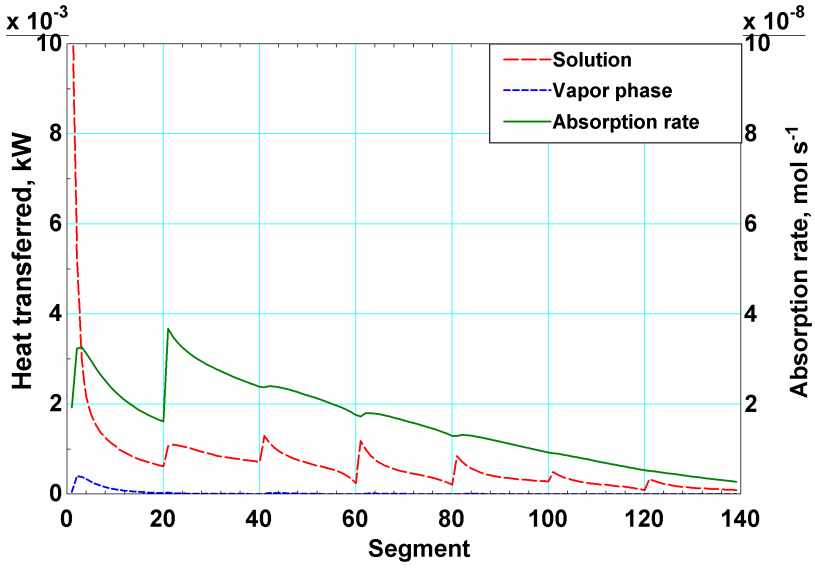

Figure 4.22: Heat and mass transfer rates in the absorber

reaching close to saturation conditions in the absorber as observed in the temperature and concentration profiles.

Figure 4.23 presents the cumulative heat transferred in the absorber and mass flow rates of the two phases. The cumulative heat transfer curve shows that most of the heat is transferred in the first three passes and then tapers off as the heat transfer rates decrease. The vapor mass flow rate decreases along the length, while the liquid mass flow rate increases. The liquid flow rate tapers off along the length of the absorber as the rate of absorption decreases.

The pressure drop through the absorber is plotted in Figure 4.24. The pressure gradient is proportional to the vapor flow rate; hence, the initial passes with higher vapor flow rates have higher pressure gradients. The pressure gradient decreases as more vapor is absorbed. The serpentine path developed to maintain high flow rates typically results in

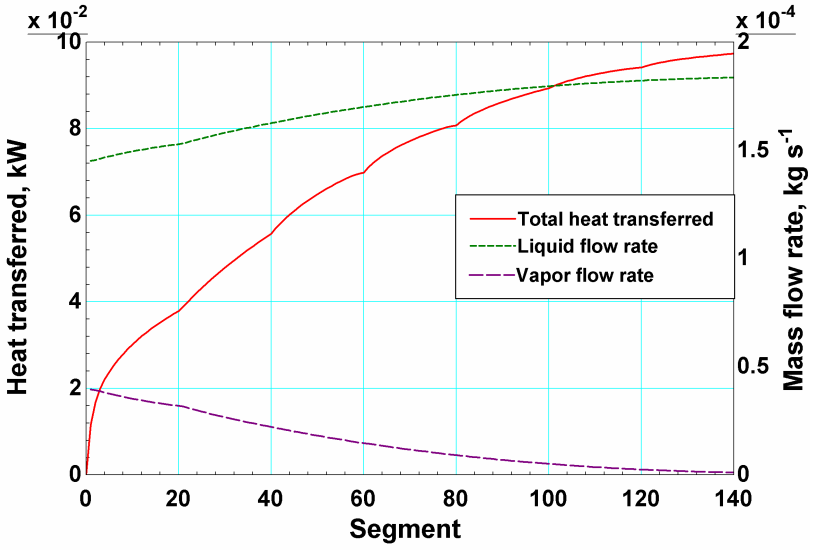

Figure 4.23: Cumulative heat transfer and mass flow rates through absorber

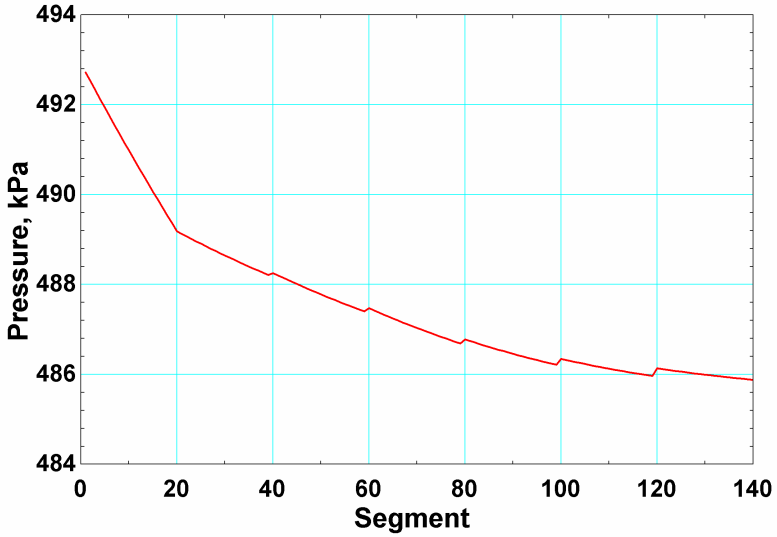

Figure 4.24: Pressure drop through the absorber

higher pressure gradients in the component compared to a typical microchannel absorber with straight channels.

The above model is validated by comparing its predictions with experimental results, specifically, the measured segmental heat duty. Figure 4.25 shows that the model predicts the measured segmental heat duty fairly accurately.

Figure 4.26 directly compares the measured and modeled segmental heat duty for all data points. It is observed that the total heat duty of the component is predicted within 10% for 37 out of the 52 test points (~70% of the measured data.) The model slightly under predicts the heat transfer in the first section with an average deviation (AD) of -13.4% and absolute average deviation (AAD) of 13.4%. The model over predicts the heat transferred in second section with AD of 30.6% and AAD of 36.9%. The overall total heat duty of the absorber is accurately predicted with an AD of 1.6% and AAD of 7.4%.

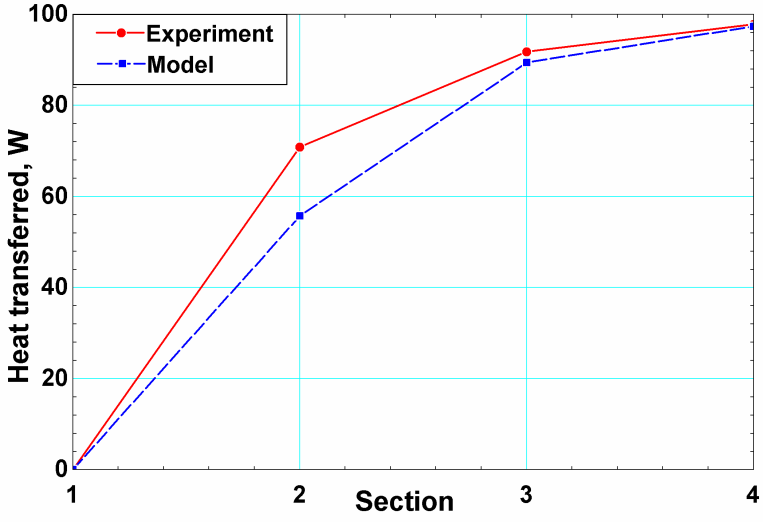

Figure 4.25: Comparison of model predictions with data

There is deviation in the prediction of heat duty in the bottom segment too, but it is observed to be within measurement uncertainty for 50% of the data. The deviation is

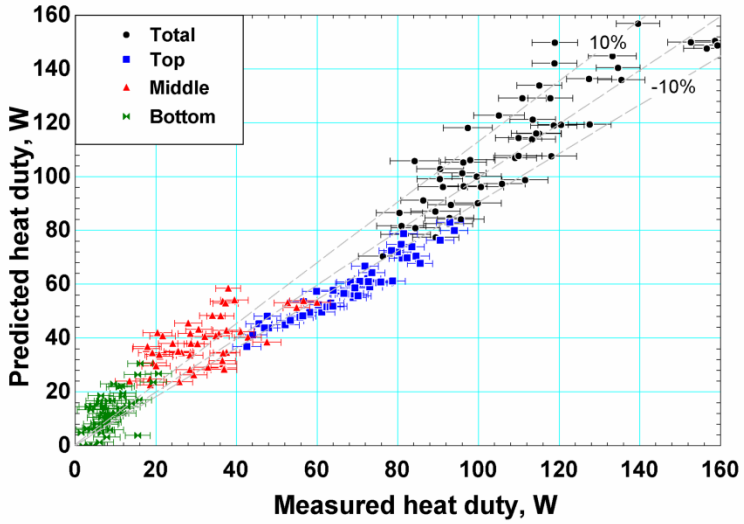

Figure 4.26: Measured and predicted heat duties

predominantly due to two reasons. The first is the presence of the bridge flow regime in sections of the first pass of the absorber. Bridge flow has higher liquid mass transfer coefficients compared to gas-slug flow. If this is accounted for, the heat duty profile will better match the measured profile. Hence, an accurate mass transfer coefficient for micro-pin fins that accounts for different flow regimes will improve the model. Another possible source of error could be that estimation of interfacial area based on air-water experiments, whereas an ammonia-water mixture has different properties. The interfacial area is expected to be slightly higher for ammonia-water mixtures as the surface tension is lower than that between air and water. Accounting for this difference could increase the heat duty in the first section as more vapor will be absorbed into the liquid.

4.6.1 Numerical Studies:

The experimental and modeling results presented so far show that the serpentine micro-pin absorber has high rates of heat transfer but is limited by mass transfer performance. To obtain a better understanding of local flow phenomena in the serpentine micro-pin fin geometry, a numerical study is conducted. Flow visualization of the absorber resulted in qualitative information such as flow regime, flow distribution, etc. For a more quantitative analysis, a CFD simulation of the flow of ammonia vapor and dilute solution through the mirco-pin fin geometry was conducted. The simulations were conducted using the volume-of-fluid method in the commercial software FLUENT^{TM} by ANSYS Inc. (2016). A 3-D structured mesh was used where the face of micro-pin fin geometry was divided into quadrilateral elements and then discretized in the perpendicular direction. The mesh had about 1.7 million elements, with an average edge length of ~0.13 mm. A grid independence study was conducted by comparing void fractions at three

different mesh sizes of average edge lengths 0.13 mm, 0.1 mm and 0.05 mm. Given the large number of mesh elements in the geometry, the grid independence test was conducted on a smaller section of the micro-pin fin geometry. Table 4.2 shows that changes in void fraction are minimal (<0.2%) with change in grid size; hence, the coarser mesh can be used without loss of accuracy. Simulations are conducted for the adiabatic flow of ammonia vapor and dilute solution through the first pass of the absorber. The inlet geometry and flow rates are used in the simulation. Average properties from the model developed in this study are used as inputs. The model was validated by comparing the average void fraction predicted in the CFD simulations with that of an air-water experiment presented in Chapter 3. The void fraction of the bottom half of the geometry was compared as it was assumed that distortion due to inlet geometries will not be as prominent in those passes. The void fraction predicted by the CFD model underpredicted that of the air water experiment by about 10%. This deviation was likely due to the poor modeling of the inlet and outlets of the geometry. It should also be noted that the uncertainty on the void fraction measurements was about 5-8% for the bottom two

Table 4.2: Grid independence study

Grid element length	Void Fraction
0.13 mm	66.45
0.10 mm (4× elements)	66.37
0.05 mm (17× elements)	66.31

windows. The model was then adapted to predict the phase distribution in the first pass of the serpentine micro-pin fin absorber geometry, as shown in Figure 4.27. The ammonia-vapor is shown in red, while the dilute solution is shown in blue. It should be noted that these simulations are for adiabatic flow. Hence, it is presented only for the first pass as vapor and liquid flow rates vary along the length of the actual diabatic absorber. As observed in the flow visualization experiments, there is a large vapor core surrounded by large liquid regions. Hence, ammonia vapor needs to diffuse from the vapor core to the large liquid regions observed at the sides of the absorber. While this distribution was observed in the flow visualization, the numerical simulations allow the derivation of local velocities that determine mixing of the two phases. A plot of velocity profiles in the geometry is shown in Figure 4.28. The legend is adjusted to highlight regions with low and and high velocities. It is observed that the liquid velocities are high in the core region where there is good mixing between vapor and liquid. However, the liquid regions at the sides of the geometries have very low circulation velocities, resulting in a lower driving force for the absorption of ammonia vapor into the solution. Low liquid velocities further

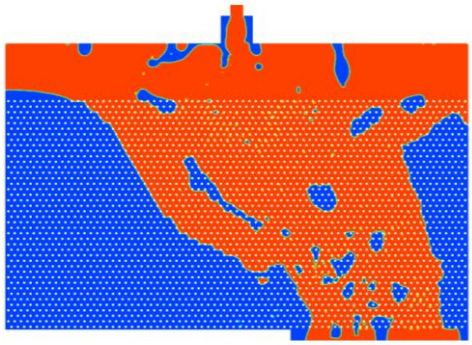

Figure 4.27: Phase distribution in first pass

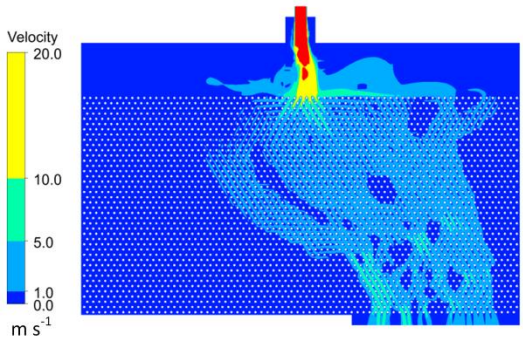

Figure 4.28: Velocity distribution in first pass

validate the conclusion that liquid mass transfer resistance is limiting the overall absorber performance.

4.7 Conclusions

An investigation into absorption of ammonia vapor in a dilute ammonia-water solution in serpentine passages with micro-pin fin geometries is conducted. This geometry is investigated for use as an absorber for ammonia-water absorption cooling systems. Visual observations of the absorption process provided insights into the internal two-phase flow characteristics. Bridge flow is observed near the inlet of the absorber, which transitions to a gas-slug flow regime as the fluid mixture proceeds toward the outlet. The gas-slug flow regime was observed to be unfavorable for absorption due to the large mass transfer resistance on the liquid side. It was also observed that while heat transfer occurred perpendicular to the absorber surface, mass transfer predominantly occurred parallel to the absorber surface. The absorber was tested over a range of three solution flow rates, concentrations, pressures, and two cooling fluid temperatures. Apparent heat transfer coefficients were observed to be between 150-1000 W m^{-2} K^{-1}.

The apparent heat transfer coefficient and absorption flux were observed to increase with the liquid-only Reynolds number and with a decrease in pressure, while they were not significantly affected by solution concentration.

A physics-based model for the absorption of ammonia into a dilute solution in a serpentine micro-pin fin absorber is developed. It was observed that the absorber had high heat transfer rates but was limited by the mass transfer process. The liquid-phase mass transfer rates were observed to be very low. A key feature of this model is the inclusion of liquid mass transfer resistance in the serpentine micro-pin fin absorber, which is typically neglected in microchannel geometries. Flow visualization and numerical investigations showed that the heat transfer between the solution and cooling fluid occurs perpendicular to the sheet surface, while most of the mass transfer occurs between the vapor core and liquid bulk along the interfaces that are perpendicular to the sheet surface. The model to predicts the absorber heat duties measured with an AAD of 6.6% and AD of 2.5%. The insights about heat and mass transfer obtained in this study and the models developed to predict these processes will be useful for the development of small-scale absorption systems.

CHAPTER 5. MICROCHANNEL ABSORBER

5.1 Introduction

A comprehensive review of investigations into the miniaturization of the absorber in ammonia-water vapor absorption systems is presented in Chapter 4. A summary of prior work on the miniaturization of absorbers is provided here. These studies typically investigated falling-film and bubble-mode absorbers to miniaturize the absorbers. Kang *et al.* (2000) and Lee *et al.* (2002a) compared the performance of a plate heat exchanger in falling-film and bubble modes. Both studies found that the plate heat exchanger performed better in the bubble mode. It was observed that liquid mass transfer resistance is the dominant resistance in bubble mode. Jenks and Narayanan (2006, 2008) investigated absorption of ammonia-water in a wide microchannel using a constrained film design, where a porous plate between the vapor and liquid regions acted as the interface. Vapor bubbles observed to encompass the whole depth of the microchannel limited heat transfer in the microchannel and in larger channels, a thick liquid layer limited heat transfer. Cerezo *et al.* (2009) investigated the use of a corrugated plate heat exchanger as an absorber, and later, Cerezo *et al.* (2010) developed a heat and mass transfer model for this corrugated plate absorber using the non-equilibrium model proposed by Colburn and Drew (1937).

Nagavarapu and Garimella (2011) showed that microchannel absorbers, with passages of hydraulic diameter 0.3 mm, have the potential to significantly decrease absorber sizes. A microchannel absorber was fabricated and tested for use in an

ammonia-water absorption chiller as reported by Nagavarapu (2012). The experimental performance was lower that the design predictions, which was attributed to channel blockage and maldistribution of vapor and liquid in the microchannel array.

Chapter 2 investigated the extent of maldistribution in microchannel arrays in adiabatic conditions through flow visualization in microchannel sheets. It was shown that multi-array microchannel heat exchangers can have significant maldistribution when there is a two-phase mixture flowing through it. Poor distribution was shown to be detrimental to the interaction between the two-phases; phase interaction is critical to components such as the absorber, where vapor is absorbed into the liquid. Hence, while heat transfer rates can be high, poor interfacial area intensities can significantly impact absorber performance. It was shown that the presence of mixing sections in microchannel arrays significantly improved phase interaction.

The present study investigates an ammonia-water absorber consisting of multiple arrays of microchannels with mixing sections between them to enhance component performance. A microchannel absorber is fabricated with windows to provide visual access to the flow of the vapor-liquid mixture through the absorber. Visual observations of the flow mechanisms using high-speed photography and heat transfer measurements are used to gain insights into ammonia-water absorption in microscale geometries.

5.2 Test sections

Two test sections, one for flow visualization, and a second for heat transfer experiments, were designed. Figure 5.1(a) shows a microchannel absorber with mixing sections. The microchannels have a channel depth of 0.5 mm and a width of 0.76 mm. The channel rib

thickness is 0.51 mm, and each rib is 11.94 mm long as shown in Figure 5.1(b). Successive microchannel arrays are offset from each other and have a mixing section between them, which is 1.27 mm long. A second sheet is shown in Figure 5.1(c); this is the cooling fluid sheet through which cooling fluid flows to absorb heat from the microchannel sheet. The microchannels in the cooling fluid sheet have the same dimensions as those in the solution sheet.

A test section assembly is designed and fabricated for the visualization of flow phenomena in the microscale ammonia-water absorber shown in Figure 5.2(a). The microchannel test section is sandwiched between a Plexiglas sheet and a cooling fluid sheet. The Plexiglas cover allows for visual access to the flow in the microchannel absorber. The test section in Figure 5.2(a) is placed in a chamber pressurized to the operating pressure so that flow visualization experiments can be conducted at the higher

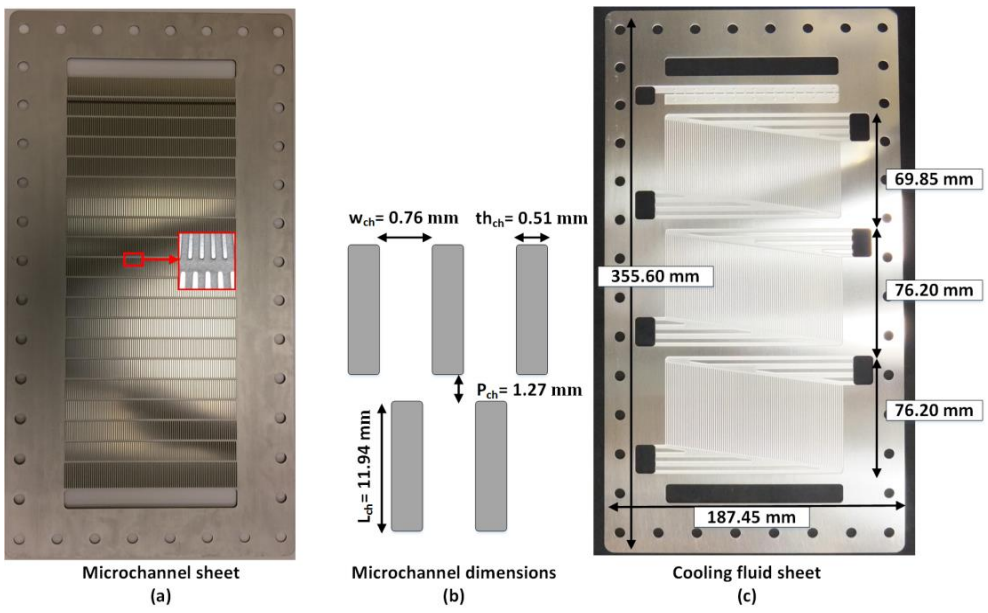

Figure 5.1: Microchannel absorber with mixing sections

operating pressures of an absorber without any appreciable differential pressure across the view ports. Another test section is fabricated for heat transfer experiments, as shown in Figure 5.2(b), where all the sheets are bonded together. This test section assembly is designed to obtain intermediate temperature measurements on the coolant side. The test section is placed outside the chamber during heat transfer tests so that it can be insulated to minimize heat losses. A more detailed description of the test section assemblies is provided in Chapter 4, where the same test section assemblies were used to test a serpentine passage geometry with micro-pin fins instead of the microchannel geometry investigated here.

5.3 Experimental setup

Figure 5.3 presents a schematic of the open ammonia-water loop experimental setup. A two-phase solution of ammonia and water enters the absorber where ammonia vapor is

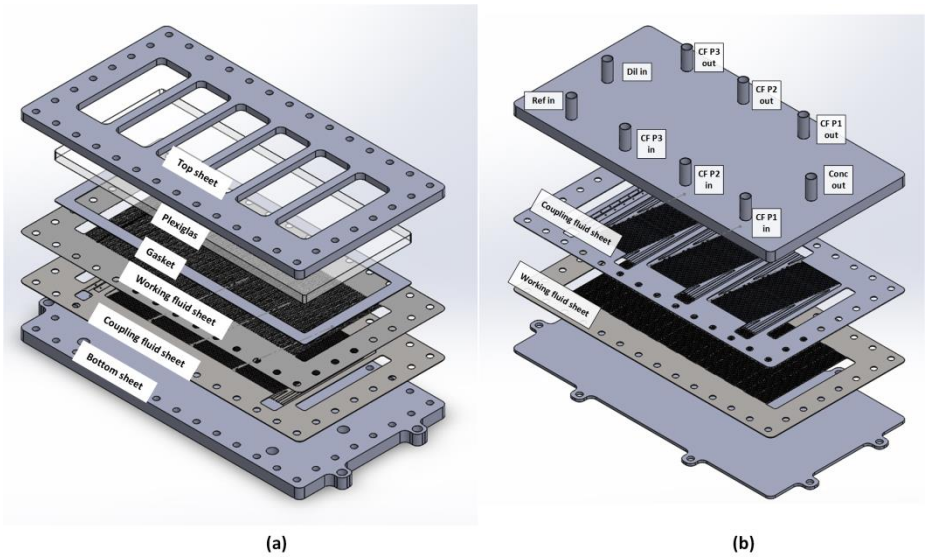

Figure 5.2: Test section assembly

absorbed into the dilute solution and exits the absorber as a concentrated solution of ammonia water. Details of the instrumentation and the experimental setup are presented in Chapter 4. The microchannel test section is tested over three concentrations, flow rates, operating pressures and two cooling fluid temperatures as shown in Table 4.1. This test matrix helps in understanding the impact of the individual parameters on the process of absorption in micro-pin fin geometries. On a system level, this corresponds to capturing the effect of different operating loads, cooling temperatures and ambient temperatures. The cooling fluid flow rates were maintained almost constant, with Reynolds numbers ranging from 24-31.

5.4 Results and discussion

5.4.1 Flow visualization

A representative image of flow through the microchannel absorber is shown in

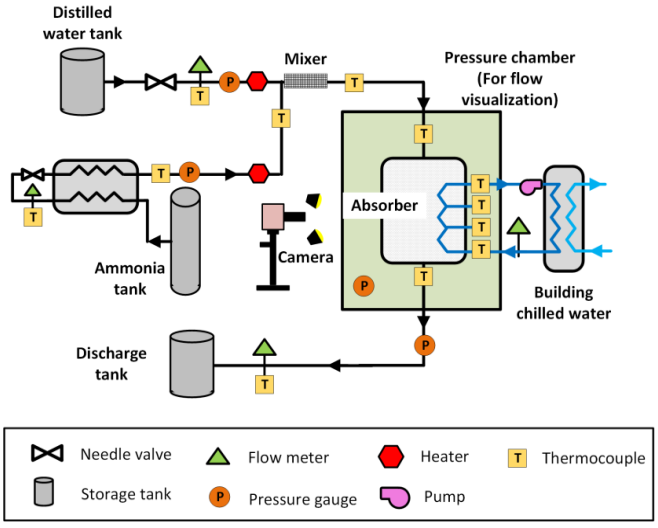

Figure 5.3: Schematic of test facility

Figure 5.4. The ammonia-water mixture flows downwards from the top to the bottom. The representative image in Figure 5.4 corresponds to a mass flux of 5.92 kg m^{-2} s^{-1} and Re_{LO} $\left(Re_{LO,in} = G_{sol,in}\, d_{ch} / \mu_{L,in}\right)$ of 8.41. The flow regime is predominantly slug flow with distinct vapor and liquid regions. High-speed images were captured at the top four windows along the length of the absorber to observe the progression of absorption, as shown in Figure 5.5. At first glance, slug flow regime is observed to be the dominant flow regime in the microchannels. It was also visually confirmed that the mixing sections helped redistribute flow along the length of the channels. This confirms that the mixing sections, first investigated in Chapter 2 under adiabatic conditions, are effective in the diabatic conditions of an absorber as well.

A two-phase mixture of ammonia-water enters through the inlet at the top of the test section. The mixture is assumed to be in equilibrium as a there is an adiabatic mixer positioned just upstream of the inlet of the test section. The vapor flow rate decreases

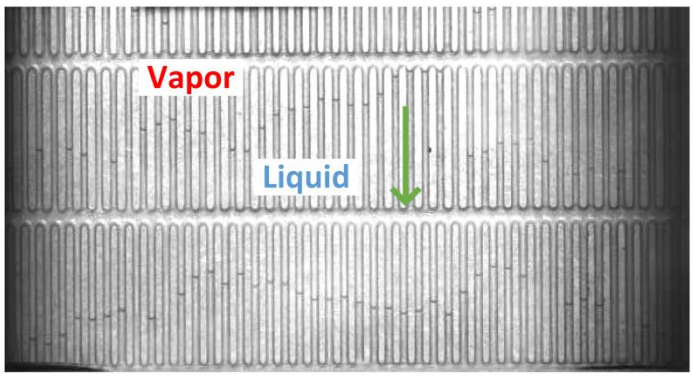

Figure 5.4: Representative image of flow through the microchannel absorber

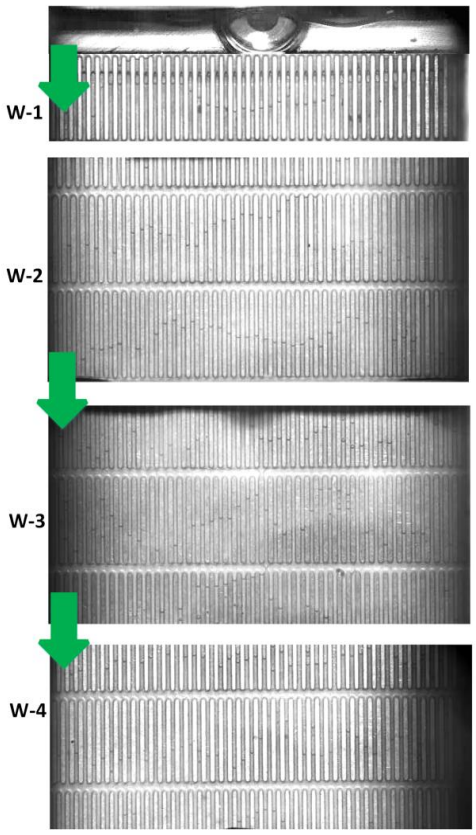

Figure 5.5: Progression of absorption through absorber

from the inlet to the outlet as it is absorbed into the liquid. There are distinct vapor and liquid regions, and the slug flow regime dominates. The vapor bubble is observed to encapsulate the whole channel, resulting in a very thin liquid film that is not easily visible in the channels. The slug flow regime is observed for most cases, and continues to be observed in most channels till the outlet. In the initial segments, liquid flows mostly through the middle channels and the vapor through the channels toward the edge. The mixing sections redistribute the vapor and liquid phases across the microchannel array. Vapor from the channels near the edge can be seen to be redistributed through the mixing

section toward the channels in the middle. Absorption of vapor into liquid can be seen based on the decreasing sizes of the vapor bubbles. Stationary interfaces in the channels are also an indication of absorption; they are observed when vapor flowing into a channel is absorbed into the liquid slug in its flow path.

The slug flow regime is intermittent in nature, and is the predominant flow regime in the microchannel absorber. This causes the flow through the absorber also to be intermittent, especially in cases with incomplete absorption through the absorber. It was also observed that there was a very thin film or no film between the vapor bubble and surface of the absorber in the adiabatic experiments with air-water mixtures conducted in Chapter 2. It is more likely that a very thin film is present in these diabatic experiments, as some vapor condenses on to the surface of the absorber. The thin film is not visible in Figures 5.4 and 5.5. This thin film is easily saturated with ammonia and cannot absorb significant quantities of ammonia from the vapor. This observation is consistent with the observations in Chaoqun *et al.* (2013), who found that film thickness is very low for Capillary numbers (Ca) ~ 10^{-3}, such as those in this study. A schematic of the flow through the microchannel absorber is shown in Figure 5.6, which also illustrates the direction of mass transfer in these channels. The thin film between the vapor bubble and the absorber surface is illustrated in Figure 5.6 (the thickness of the film is exaggerated for better representation)

5.4.2 Heat transfer experiments

Ammonia and water are premixed at the inlet and flow through the absorber. Cooling fluid flows counter to the ammonia-water mixture and the temperature is

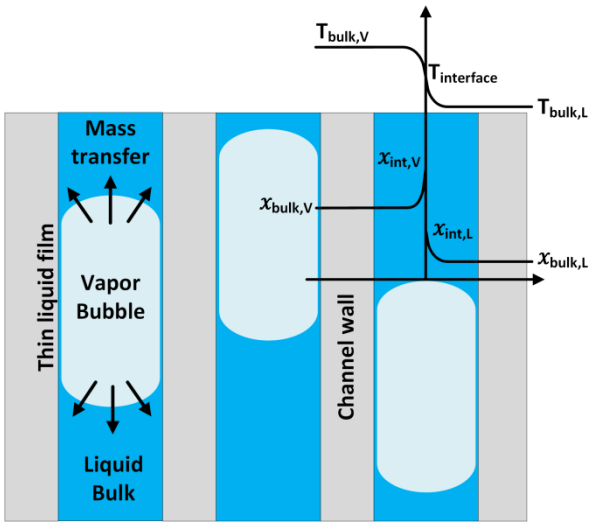

Figure 5.6: Schematic of flow through the microchannel absorber

measured at two intermediate locations. Mass and species balances are used to calculate the concentration of the solution in the absorber. The inlet of the absorber is assumed to be in equilibrium. The measured inlet temperature, pressure and the calculated concentration are used to obtain the inlet state of the two-phase mixture. The data analysis methodology used is described in more detail in Chapter 4 and Appendix A.

The heat duty of the absorber is calculated using the measured segmental cooling fluid flow rates and temperature. The heat transferred through each segment is calculated by summing the heat absorbed by the cooling fluid and the heat lost to the ambient.

The heat transferred in each of the segments is then summed to obtain the total heat transferred in the absorber as shown in Equation (5.1).

$$\dot{Q}_{abs,CF} = \dot{Q}_{seg,top} + \dot{Q}_{seg,mid} + \dot{Q}_{seg,bot} \tag{5.1}$$

The heat transferred in the absorber is also calculated from the solution side as shown in Equation (5.2). In this calculation, it is assumed that the ammonia-water mixture exiting the absorber is in equilibrium.

$$\dot{Q}_{abs,sol} = \dot{m}_{sol,in}\left(h_{sol,in}\left(T_{sol,in}, P_{sol,in}, x_{sol,in}\right) - h_{sol,out}\left(T_{sol,out}, P_{sol,out}, x_{sol,out}\right)\right) \quad (5.2)$$

A comparison of the two calculated values of heat transferred in Figure 5.7 shows that the two values are within experimental uncertainties for about 50% of the data points. It is also observed the heat transfer rate calculated from the working fluid side is significantly higher than that calculated on the cooling fluid side for some of the data points. This deviation is an indication of a case with incomplete absorption of vapor into the liquid. At certain conditions, a two-phase mixture of a subcooled ammonia water solution and superheated ammonia vapor can exit the absorber, indicating that the absorber is mass transfer limited.

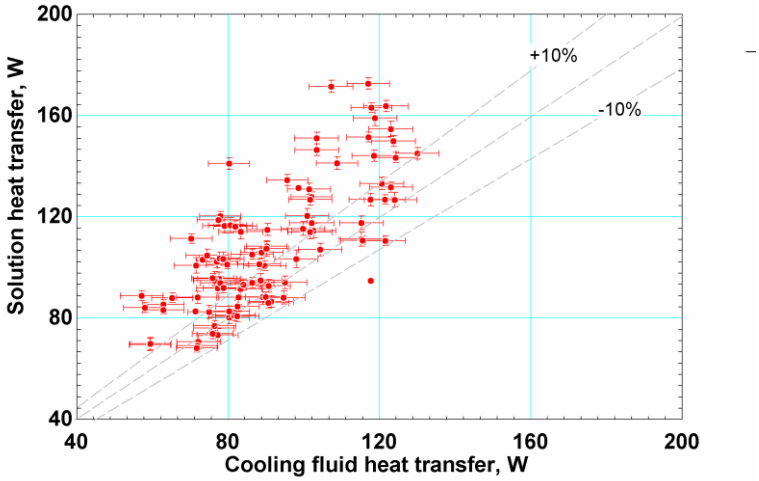

Figure 5.7: Heat transfer rates in the working fluid and cooling fluid

Figure 5.8 shows the cooling fluid temperature distribution and the segmental heat duty in the absorber. The solution enters the absorber at a bulk concentration of 0.41, mass flow rate of 1.98×10^{-4} kg s^{-1}, pressure of 555 kPa and temperature of 81.6°C. The Y-axis on the left corresponds to cooling fluid temperatures at the four locations shown. The Y-axis on the right presents the cumulative heat transferred from the solution. It is observed that there is a steep increase in temperature in the top cooling fluid segment; this indicates that most (~52 W) of the heat transfer occurs in the top segment. The heat transferred through the middle and bottom segments is about 23 W and 16 W, respectively. This characteristic distribution of heat transfer rate is observed in all tests. The high heat duty of the first segment is due to the high rates of sensible cooling and condensation in the first segment. A pre-mixed ammonia-water mixture enters in the first segment at a high temperature, resulting in a high temperature difference between the pre-mixed solution and the cooling fluid, which leads to high heat duties in the first

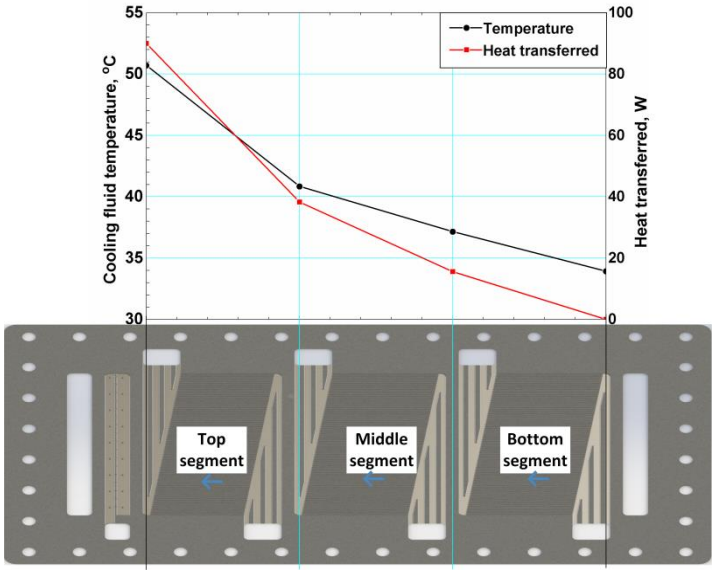

Figure 5.8: Cooling fluid temperature and heat duty distribution in absorber

segment. The segmental heat duty distribution is different from that observed in a study of serpentine passage micro-pin fin absorbers in Chapter 4. In that study, heat duties in the first segment were higher and the heat duties in the last segment were much lower those seen in the present study. This difference is explained by the higher interfacial area at the inlet for the serpentine micro-pin fin absorber leading to higher rates of mass transfer in the first segment. In the microchannel geometry, the flow is constantly redistributing between channels resulting in higher mixing in regions closer to the outlet. This results in higher heat duties in the last segment of the microchannel absorber.

The component UA value is calculated as shown in Equation (5.3) from component heat duty and the logarithmic mean temperature difference.

$$\dot{Q}_{abs,CF} = UA \cdot \Delta T_{LM} \left(T_{sol,in} T_{CF,out}, T_{sol,out}, T_{CF,in} \right) \tag{5.3}$$

The thermal resistance network in the absorber is shown in Figure 5.9. The coolant-side thermal resistance is calculated in Equation (5.4) using the correlation for heat transfer coefficient for flow through semi-circular channels developed by Sparrow and Haji-Sheikh (1965) and cited in Kakac *et al.* (1987). For the low Reynolds numbers in the range 25-30 as they are in this study, the Nusselt number is constant, with a value of 4.08, yielding a heat transfer coefficient of ~3600 W m^{-2} K^{-1}. The solution-side thermal resistance is calculated from the *UA* value as shown in Equation (5.5). Zeotropic mixture condensation involves a combination of heat and mass transfer. Therefore, an apparent heat transfer is typically calculated for zeotropic mixtures as the actual heat transfer coefficient is difficult to calculate. The solution apparent heat transfer coefficient defined in Equation (5.6) is then calculated as shown in Equation (5.7).

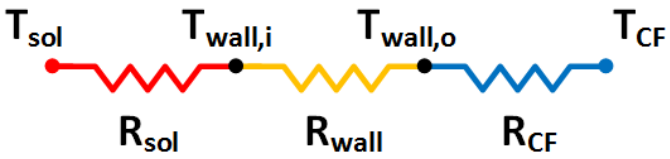

Figure 5.9: Absorber resistance network

$$R_{CF} = \frac{1}{\alpha_{CF} A_{CF,ht}} \tag{5.4}$$

$$R_{sol} = \frac{1}{UA} - R_{wall} - R_{CF} \tag{5.5}$$

$$\alpha'_{abs} = \frac{q''_{abs}}{T_{bulk} - T_w} \tag{5.6}$$

$$\alpha'_{abs} = \frac{1}{R_{sol} A_{MC,ht}} \tag{5.7}$$

Figure 5.10(a) shows the increase in absorber heat duty with an increase in the inlet liquid only Reynolds number (Re_{LO}) and a decrease in cooling fluid temperature. Figure 5.10(b) shows that all heat transfer coefficient increase with Re_{LO} and are in a narrow range of values between 60-180 W m^{-2} K^{-1}. These trends were also observed in Nagavarapu (2012) where a microchannel absorber was investigated as part of a complete vapor absorption cooling system. The apparent heat transfer coefficient was observed to be slightly higher at lower cooling fluid temperatures. This was observed in the serpentine micro-pin fin absorber studied in Chapter 4 as well. A lower cooling fluid temperature indirectly increases the concentration difference between the interface and the bulk vapor. This concentration difference is the driving force for mass transfer between the vapor and the interface; hence, as it increases, the rates of mass transfer increase.

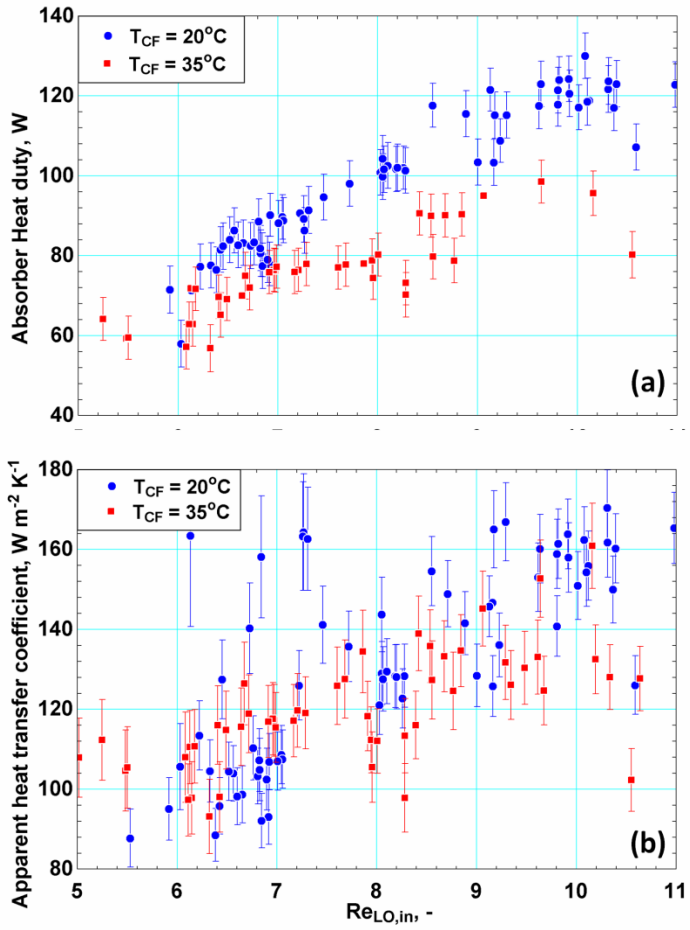

Figure 5.10: Variation of apparent heat transfer coefficient with inlet Reynolds number

The uncertainty in the measured heat duty is a direct function of the uncertainty in the flow meter and the temperature measurement and has a constant value ~5.5 W. The solution side accounted for 90-95% of the thermal resistance, which resulted in low uncertainties in the apparent heat transfer coefficient. The uncertainty in the apparent heat transfer coefficient varies from 5.1% to 13.9%, with the average at about 7.2 %. The lowest uncertainties are at a ΔT_{LM} of 23.9°C, while the highest uncertainties are at ΔT_{LM} of 12.4°C.

The vapor and liquid have high single-phase heat transfer coefficients due to the small hydraulic diameter, which is the heat transfer length scale. The mass transfer length scale was observed to be much higher in the absorber as mass transfer predominantly occurs in a direction parallel to flow as shown in Figure 5.6. The low diffusivity of ammonia in the liquid phase (4.2×10^{-9} m^2 s^{-1}) compared to the vapor phase (6.4×10^{-6} m^2 s^{-1}) further limits mass transfer rates in the liquid phase. Hence, the vapor and liquid are assumed to be only in thermal equilibrium at the measured outlet temperature given the high heat transfer rates. The vapor is assumed to be saturated at the outlet. The average enthalpy of the solution outlet is calculated as shown in Equation (5.8).

$$\dot{m}_{sol} h_{sol,out} = \dot{m}_{sol} h_{sol,in} - \dot{Q}_{abs,cf} \tag{5.8}$$

Equations (5.9-5.11) are solved iteratively to obtain the mass flow rates and concentrations of the individual phases.

$$\dot{m}_{sol} = \dot{m}_{vap,out} + \dot{m}_{liq,out} \tag{5.9}$$

$$\dot{m}_{sol} x_{sol,out} = \dot{m}_{vap,out} x_{vap,out} + \dot{m}_{liq,out} x_{liq,out} \tag{5.10}$$

$$\dot{m}_{sol} h_{sol,out} = \dot{m}_{vap,out} h_{vap,out}\left(P_{abs,out}, T_{sol,out}, q_{vap,out} = 1\right) + \dot{m}_{liq,out} h_{liq,out}\left(P_{abs,out}, T_{sol,out}, x_{liq,out}\right) \tag{5.11}$$

The absorption flux, which is defined as the rate of vapor absorbed per unit area and the absorption intensity, defined as the rate of vapor absorbed per unit fluid volume of the heat exchanger, are used to quantify absorber mass transfer efficiency. Figure 5.11 shows the impact of cooling fluid temperature on the rate of absorption. A lower cooling water temperature results in higher rates of absorption. A similar trend was observed in the serpentine absorber presented in Chapter 4. As the liquid interface temperature decreases, the corresponding equilibrium concentration at the liquid interface increases. This

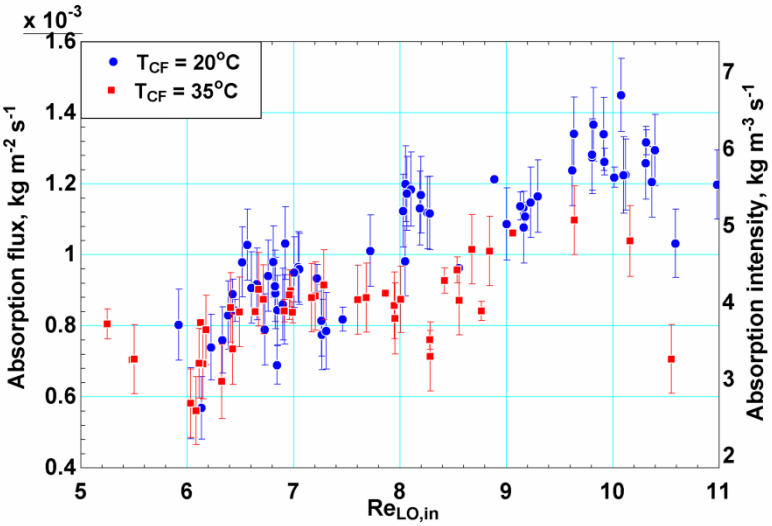

Figure 5.11: Influence of cooling fluid temperature on the rate of absorption

increases the concentration difference between the liquid interface and liquid bulk, which is the driving force for absorption into the liquid bulk. As the vapor cools, more water is condensed from the vapor bulk to the interface.

Figure 5.12(a) shows that the apparent heat transfer coefficient is not significantly influenced by system pressure. The two-phase mixture at the inlet has higher volumetric flow rates at lower pressures due to higher specific volumes of the vapor. The higher vapor specific volumes result in higher bubble and slug velocities, which leads to higher heat and mass transfer coefficients through higher rates of circulation in the vapor bubble and liquid slug. This is balanced out by increased concentration difference between the interface and the liquid bulk at higher operating pressures. Hence, there is no appreciable effect of pressure on apparent heat transfer coefficient in microchannel absorbers. Similarly there is no appreciable difference in absorption flux shown in Figure 5.12(b), which is more influenced by the Reynolds number than pressure.

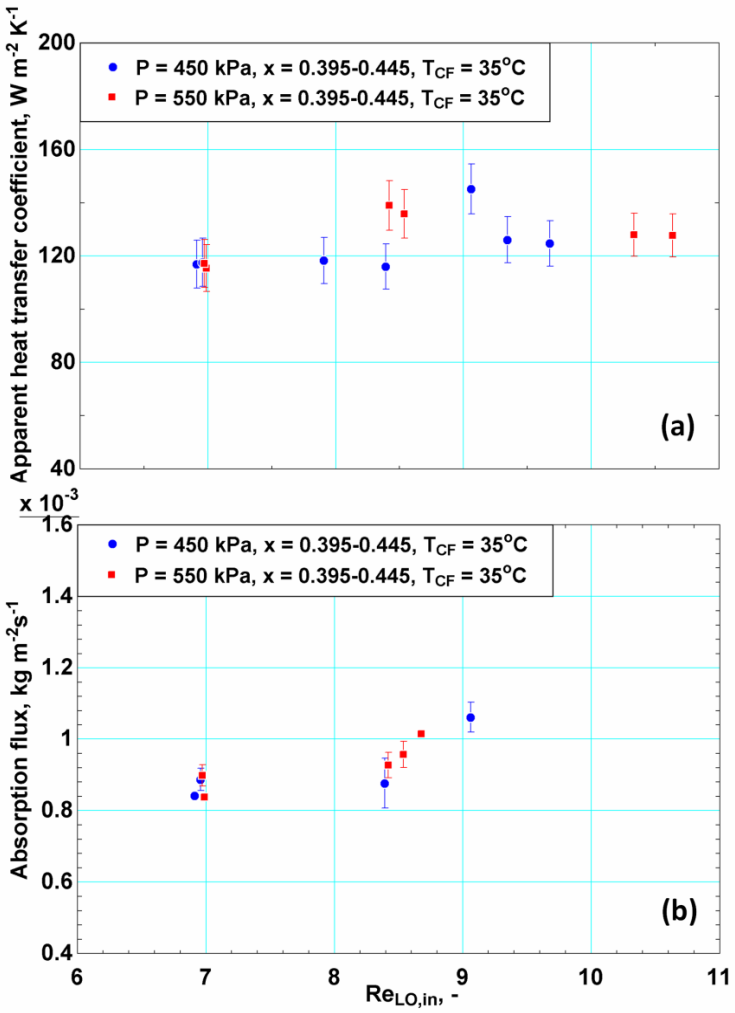

Figure 5.12: Effect of pressure on heat transfer coefficient and absorption flux

The performance of the microchannel absorber with mixing sections is then compared to that of the serpentine micro-pin fin absorber investigated in Chapter 4. Both absorber geometries were investigated across the same test matrix; hence, a direct comparison of various performance parameters is possible as the test conditions were very similar. The small variations in the test conditions were not enough to account for the large differences in various performance parameters. Figure 5.13(a) presents a direct comparison of absorber heat duty for the geometries across at all test conditions. The heat

transferred in the serpentine absorber was higher than that in the microchannel absorber. Since both geometries have high local heat transfer coefficients, this is likely due to higher rates of absorption in the serpentine absorber.

Figure 5.13(b) presents a comparison of apparent heat transfer coefficient for the two geometries across the test matrix. The serpentine absorber can be observed to have significantly higher apparent heat transfer coefficients than the microchannel absorber. The higher apparent heat transfer coefficients confirm higher rates of absorption in the serpentine absorber. Flow visualization experiments through these geometries had shown better mixing between vapor and liquid phases in the serpentine absorber. The increased interfacial area results in higher rates of mass transfer from the vapor to the liquid.

Figure 5.14 compares the absorption intensity of the microchannel and serpentine micro-pin fin absorbers at a constant cooling fluid inlet temperature. The serpentine absorber is observed to have higher absorption intensities compared to the microchannel absorber. This is due to the higher interfacial area in the serpentine micro-pin fin geometry, which leads higher mass transfer rates.

5.5 Heat and mas-transfer model development

The equilibrium approach described by Silver (1947) and Bell and Ghaly (1973), often used to model binary mixture heat and mass transfer is computationally simple. The computationally intensive non-equilibrium approach developed by Colburn and Drew (1937) and later adapted by Price and Bell (1974) is used here to model the microchannel absorber, as the conditions for the applicability of the equilibrium approach are not

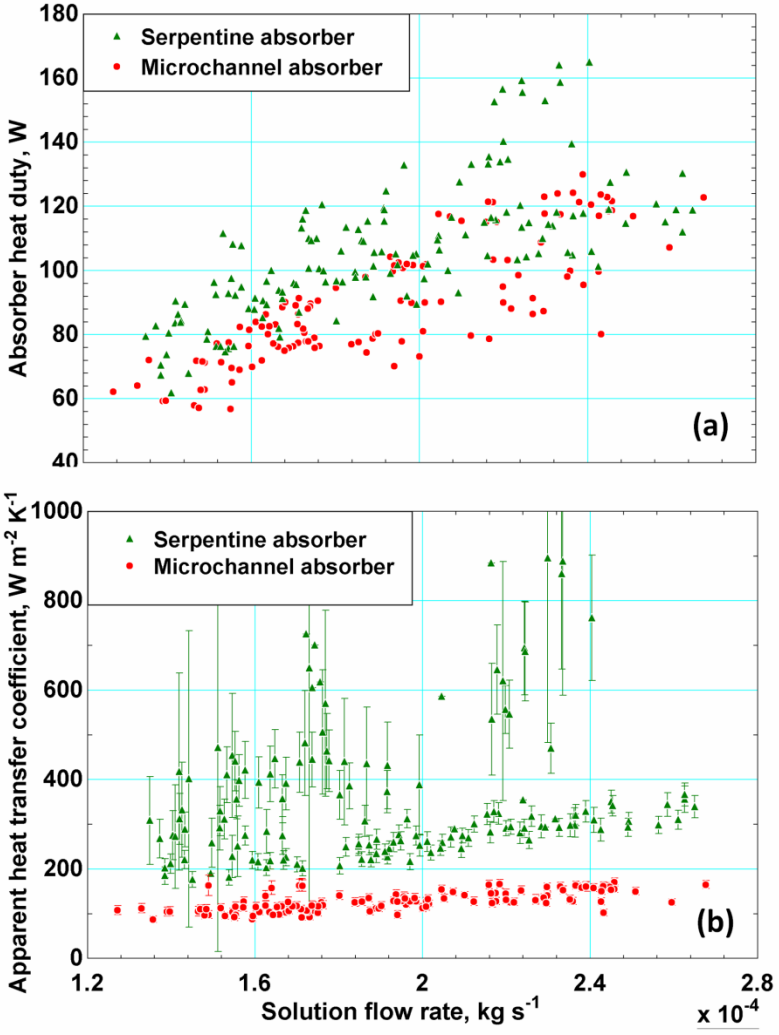

Figure 5.13: Comparison of microchannel and serpentine micro-pin absorbers

satisfied. A more detailed justification for the use of the non-equilibrium approach can be found in Chapter 4.

As discussed earlier, the two-phase flow under consideration here has really low Capillary numbers (Ca) of the order of 10^{-3}, which results in bubbles with very thin films similar to those reported by Chaoqun *et al.* (2013). Hence, the mass transfer to the liquid

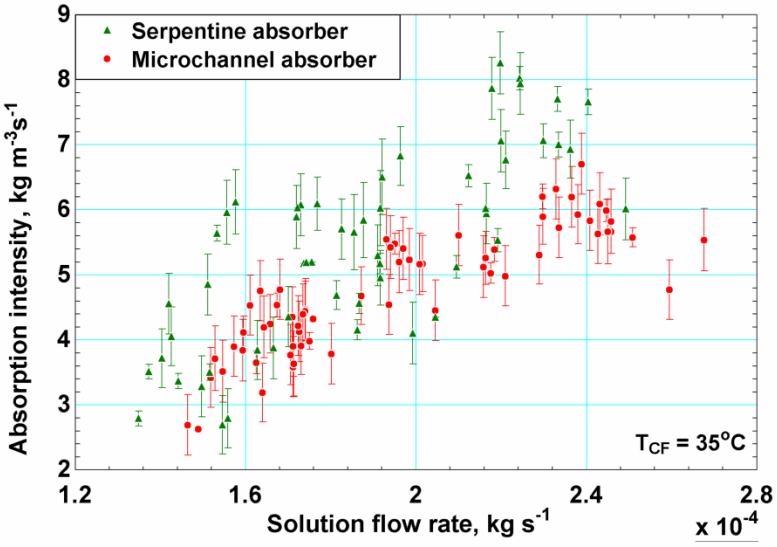

Figure 5.14: Comparison of absorption intensity in microchannel and serpentine micro-pin absorbers

film is neglected as these films are very thin and cannot absorb appreciable quantities of vapor.

The high-speed videos of flow through the absorber guide the conceptual representation of flow through the microchannels shown in Figure 5.15. The ammonia-water mixture enters the absorber as a two-phase mixture in thermal equilibrium. As the cooling fluid sensibly cools the mixture, water is preferentially absorbed into the mixture, resulting in higher ammonia concentration at the interface. The mass that is absorbed at interface has a higher ammonia concentration than the liquid bulk; hence, there is transfer of ammonia from the interface to the liquid bulk. The temperature is highest in the vapor phase, which exchanges heat with the interface. The heat is transferred from the interface to the liquid bulk, which is cooled by the coupling fluid on the adjacent sheet.

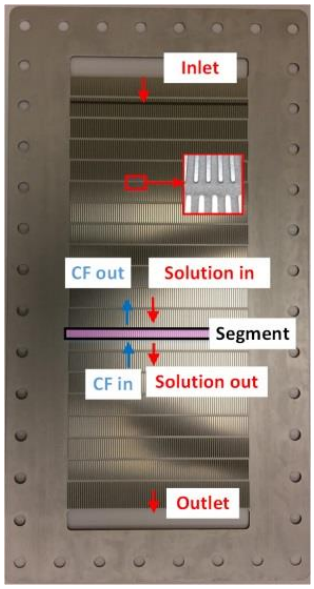

Figure 5.15: Representative segment in the microchannel absorber

5.5.1 Segmental Model

Figure 5.16 shows an illustration of a sample segment where the solution and cooling fluid are in a counter-flow orientation. Each segment had a constant length of 2.54 mm and was chosen to be able to match exactly the lengths of each cooling fluid segment. This resulted in a total of 93 segments along the length of the absorber. The resistance network for the heat and mass transfer process is shown in Figure 5.17. Heat is transferred from the vapor to the interface. The vapor-liquid interface is assumed to be in thermal equilibrium with the liquid bulk as the liquid-phase heat transfer coefficients are high. Heat is then transferred from the liquid phase to the channel wall. The heat conducted across the wall is absorbed by the cooling fluid flowing in passages on the adjacent sheet. An explicit segmented model is developed, where outlet conditions from one segment are used as the inlet conditions to the next segment.

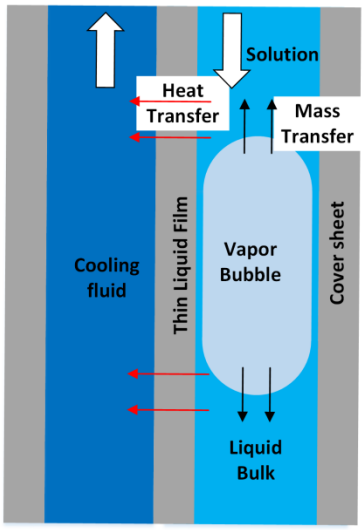

Figure 5.16: Schematic of flow through microchannels

At the inlet of each segment, the inlet interface liquid and vapor concentrations are determined as shown in Equations (5.12) and (5.13). The segment inlet pressure, interface temperature and a saturation condition are used to determine the properties. The interface temperature is assumed to be same as the liquid temperature due to the high rates of heat transfer in the geometry.

$$x_{L,int,in} = f\left(P = P_{seg,in}, T = T_{L,in}, q = 0\right) \tag{5.12}$$

$$x_{v,int,in} = f\left(P = P_{seg,in}, T = T_{L,in}, q = 1\right) \tag{5.13}$$

Once the interface concentrations are known, the mass fluxes from the vapor to the interface are calculated using the framework presented in Price and Bell (1974) as shown in Equation (5.14).

$$\dot{n}''_{T} = \beta_{v} \times C_{v,T} \times \ln\left(\frac{\tilde{z} - \tilde{x}_{v,int}}{\tilde{z} - \tilde{x}_{v,bulk}}\right) \tag{5.14}$$

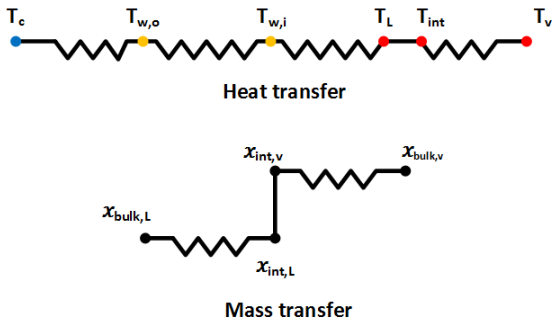

Figure 5.17: Resistance diagram for heat and mass transfer

where $\tilde{x}_{v,int}$ is the mole fraction of vapor at the interface, $\tilde{x}_{v,bulk}$ is bulk vapor concentration, $\tilde{z}$ is the mole fraction of the condensing flux, and $C_{v,T}$ is the bulk concentration. All bulk properties are averaged across the inlet and outlet. β_v is the vapor-phase mass transfer coefficient from the interface to the vapor bulk. The flow through the channels is predominantly in the slug flow regime.

The mass transfer coefficient β_v is determined based on the internal circulation of the vapor bubble. Kashid *et al.* (2005) studied the internal flow circulation in slug flow using PIV and CFD based investigations. Their investigations showed that the internal circulation patterns in the bubble and slug are very similar, and these circulation patterns determine the mass transfer of a species from the interface to the bulk. There have been several investigations of mass transfer in slug flow (Vandu *et al.*, 2005; Yue *et al.*, 2007; Dessimoz *et al.*, 2008; Di Miceli Raimondi *et al.*, 2008; Sobieszuk *et al.*, 2011). The mass transfer correlation developed by Di Miceli Raimondi *et al.* (2008) was observed to be most applicable for the superficial velocities and channel geometries under

consideration here. The mass transfer coefficient is calculated as shown in Equation (5.15).

$$Sh_{d,v} = 31.4\left(\frac{\rho_L j_V d_h}{\mu_L}\right)^{0.371}\left(\frac{\mu_L j_V}{\sigma}\right)^{0.371}\left(\frac{4D_{aw,v}\left(L_{bub} - w_{ch} + \pi w_{ch}/2\right)}{d_h^2 j_v}\right)^{-0.338}\left(\frac{\mu_v}{\rho_v D_{aw,v}}\right)^{-0.125} \quad (5.15)$$

where $D_{aw,v}$ is the diffusivity of ammonia in the vapor phase, d_h is the hydraulic diameter of the channel, L_{bub} is the bubble length and w_{ch} is the width of the channel. The four terms from left to right are the Reynolds number, Capillary number, Fourier number and the Schmidt number. The Fourier number is a function of the contact time in the bubble. In this case, the contact time is defined as the length travelled by a fluid element in the bubble over the phase velocity.

The molar flux from the interface to the liquid bulk is also calculated similarly as shown in Equation (5.16). The mass transfer is determined by the circulation patterns in the liquid slug. As both the vapor bubble and liquid slug have similar circulation patterns, the mass transfer coefficient in the liquid slug was also calculated using the correlation of Di Miceli Raimondi *et al.* (2008).

$$\dot{n}_T'' = -\beta_L \times C_{L,T} \times \ln\left(\frac{\tilde{z} - \tilde{x}_{L,\text{int}}}{\tilde{z} - \tilde{x}_{L,bulk}}\right) \quad (5.16)$$

The condensed flux of ammonia and water are calculated as shown in Equations (5.17) and (5.18).

$$\dot{n}_A'' = \tilde{z} \cdot \dot{n}_T'' \quad (5.17)$$

$$\dot{n}_W'' = (1 - \tilde{z}) \cdot \dot{n}_T'' \quad (5.18)$$

The masses of ammonia and water absorbed into the solution are then calculated as shown in Equations (5.19) and (5.20).

$$\dot{m}_{abs,A} = \dot{n}''_A \cdot A_{int} \cdot M_A \tag{5.19}$$

$$\dot{m}_{abs,W} = \dot{n}''_W \cdot A_{int} \cdot M_W \tag{5.20}$$

where M_A and M_W are the molecular masses of ammonia and water. The interfacial area (A_{int}) is estimated from the results presented in Chapter 2, where the average interfacial area intensity was observed to be 850 m^2 m^{-3} × ε_{ch} for the data range. The interfacial area was then calculated as shown in Equation (5.21).

$$IA_{area} = 850\ [m^2 m^{-3}] \cdot \varepsilon_{ch} \cdot \forall_{ch} \tag{5.21}$$

where, ε_{ch} is the channel void fraction and $\forall_{ch}$ is the volume of the channel segment. The mass and concentration of vapor leaving the segment are calculated using Equations (5.22) and (5.23).

$$\dot{m}_{v,out} = \dot{m}_{v,in} - \dot{m}_{abs,A} - \dot{m}_{abs,W} \tag{5.22}$$

$$\dot{m}_{v,out} \cdot x_{v,out} = \dot{m}_{v,in} \cdot x_{v,in} - \dot{m}_{abs,A} \tag{5.23}$$

where $x_{v,in}$ and $x_{v,out}$ are the segment inlet and outlet concentrations of ammonia in the vapor phase. Once the outlet vapor mass flow rate and concentration are known, a mass, species and energy balances on the segment are conducted to obtain the liquid outlet properties as shown in Equations (5.24) and (5.25).

$$\dot{m}_{v,out} + \dot{m}_{L,out} = \dot{m}_{v,in} + \dot{m}_{L,in} \tag{5.24}$$

$$\dot{m}_{v,out} \cdot x_{v,out} + \dot{m}_{L,out} \cdot x_{L,out} = \dot{m}_{v,in} \cdot x_{v,in} + \dot{m}_{L,in} \cdot x_{L,in} \tag{5.25}$$

With the liquid concentration known, the heat released during absorption is calculated as shown in Equation (5.26).

$$\dot{m}_{v,out} \cdot h_{v,out} + \dot{m}_{L,out} \cdot h_{L,out} + \dot{Q}_{abs} = \dot{m}_{v,in} \cdot h_{v,in} + \dot{m}_{L,in} \cdot h_{L,in} \tag{5.26}$$

Here, $\dot{Q}_{abs}$ is the heat transferred from the solution to the cooling fluid. This includes the sensible cooling and heat of absorption. It should be noted that at this point, the outlet

vapor and liquid enthalpies are not known. While the outlet pressure and concentration of the two phases are known, a third property is needed to completely define the outlet state. The sensible heat transfer from vapor to the interface is calculated as shown in Equation (5.27).

$$\dot{Q}_v = \alpha_v \left(\frac{\phi}{1 - e^{-\phi}} \right) A_{int} \cdot \Delta T_{LM,v,int} \tag{5.27}$$

where α_v is the vapor-phase heat transfer coefficient and $\Delta T_{LM,v,int}$ is the log mean temperature difference between the vapor and the interface. The term in the parenthesis corrects for mass transfer from the vapor to the interface, and ϕ is defined as shown in Equation (5.28).

$$\phi = \frac{\left(\dot{n}''_A \tilde{C}_{p,A} \right) + \left(\dot{n}''_W \tilde{C}_{p,W} \right)}{\alpha_v} \tag{5.28}$$

where $\tilde{C}_{p,A}$ and $\tilde{C}_{p,W}$ are the molar specific heat capacities of ammonia and water. The Nusselt number (Nu_v) is calculated from the single-phase heat transfer coefficient for flow through semi-circular channels developed by Sparrow and Haji-Sheikh (1965) cited in Kakac *et al.* (1987) as shown in Equation (5.29).

$$Nu_v = 2.0705 \cdot \left(1 + 2.2916 \cdot \theta - 2.5682 \cdot \theta^2 + 1.4815 \cdot \theta^3 - 0.3338 \cdot \theta^4 \right) \tag{5.29}$$

The sensible heat transfer from the vapor phase can also be calculated as shown in Equation (5.30). The vapor outlet temperature is calculated by solving Equations (5.27) and (5.30).

$$\dot{Q}_v = \dot{m}_v \cdot C_{p,v} \cdot \left(T_{v,in} - T_{v,out} \right) \tag{5.30}$$

An energy balance on the cooling fluid is presented in Equation (5.31). $\dot{Q}_{abs}$ can also be calculated from the overall heat transfer coefficient as shown in Equation (5.32). Equations (5.26), (5.31) and (5.32) are solved in parallel to calculate the cooling fluid outlet temperature, liquid outlet temperature, and $\dot{Q}_{abs}$.

$$\dot{Q}_{abs} = \dot{m}_{CF} \cdot C_{p,CF} \cdot \left(T_{CF,out} - T_{CF,in}\right) \tag{5.31}$$

$$\dot{Q}_{abs} = \left(U \cdot A\right)_{abs} \cdot \Delta T_{LM,int,CF} \tag{5.32}$$

where, U_{abs} is the overall heat transfer coefficient, A_{abs} the overall absorber area and $\Delta T_{\text{LM,int,CF}}$ is the log mean temperature difference between the interface and cooling fluid. The *UA* for the absorber is calculated from the resistance diagram as shown in Equation (5.33).

$$\left(U \cdot A\right)_{abs} = \frac{1}{R_{abs}} = \frac{1}{R_{sol} + R_{wall} + R_{CF}} \tag{5.33}$$

where R_{sol} is the solution side thermal resistance, R_{wall} is the thermal resistance for conduction across the sheet and R_{CF} is the cooling fluid resistance. The individual resistances are calculated as shown in Equations (5.34) - (5.36).

$$R_{sol} = \frac{1}{\alpha_{sol} \cdot N_{ch} \cdot \left(A_{base} + \eta_{ch} A_{ch,ht}\right)} \tag{5.34}$$

where α_{sol} is the solution side heat transfer coefficient calculated using the correlation from Kim and Mudawar (2013). This correlation was most applicable as it was developed for condensing flow in microchannels for low Reynolds numbers. The absorber is designed to operate in a vertical configuration. Flow visualization experiments showed that the flow is predominantly in the slug flow regime. A_{base} is the

channel base area, N_{ch} is the number of channels in the segment, $A_{ch,ht}$ is the fin surface area of the channel and η_{ch} is the fin efficiency of the channel fin surfaces.

$$R_{wall} = \frac{th_{sheet}}{k_{wall} \cdot A_{seg}} \tag{5.35}$$

where th_{sheet} is the thickness of the absorber sheet, k_{wall} is the thermal conductivity of the sheet, which in this case is stainless steel 304, and A_{seg} is the segmental cross-sectional area.

$$R_{CF} = \frac{1}{\alpha_{CF} \cdot N_{ch} \cdot \left(A_{ch,base} + \eta_{cf,fin} A_{cf,fin} \right)} \tag{5.36}$$

where α_{CF} is the cooling fluid heat transfer coefficient in the microchannels calculated using the correlation for semi-circular channels developed by Sparrow and Haji-Sheikh (1965), N_{ch} is the number of channels in the segment, $A_{ch,base}$ is channel base area, $A_{ch,fin}$ is the fin area and $\eta_{cf,fin}$ is fin efficiency of the cooling fluid channel fin. A sample calculation of the above heat and mass transfer framework is presented in Appendix B. The pressure drop is calculated across every segment as shown in Equations (5.37) - (5.40) and the inlet pressure to the following segment is updated. The frictional pressure drop across the absorber is calculated from the framework presented in Garimella *et al.* (2005b).

$$\Delta P_{seg} = \Delta P_{fr} + \Delta P_{gravity} + \Delta P_{dec} \tag{5.37}$$

$$\Delta P_{gravity} = -\left[\alpha \rho_g + (1-\alpha) \rho_l \right] gh \tag{5.38}$$

$$\Delta P_{fr} = \Delta P_{L,slug} + \Delta P_{bubble} + \Delta P_{transition} \tag{5.39}$$

$$\Delta P_{dec} = \frac{G^2}{\rho_{h,out}} - \frac{G^2}{\rho_{h,in}} \tag{5.40}$$

The above discussion pertains to the modeling of heat and mass transfer for a single segment. The calculated outlet conditions are used as the inlet conditions for the successive segment and this continues for all segments.

5.6 Model results

The temperature profiles of the vapor bulk, interface, liquid bulk and cooling fluid along the length of the absorber (0-0.24 m) predicted by the model described above for a representative case with a concentration of 0.47, pressure of 488 kPa, inlet temperature of 77°C and coolant inlet temperature of 34°C are shown in Figure 5.18. There is a steep temperature drop from the inlet to 0.02 m as the solution is sensibly cooled from a high inlet temperature of ~77°C to ~48°C. This results in significant heat transfer in the region close to the inlet. The vapor temperature is higher than the interface temperature in the initial segments and then decreases to almost the same temperature as the liquid. This shows that there is a lag between the temperatures of the two phases. As the liquid region

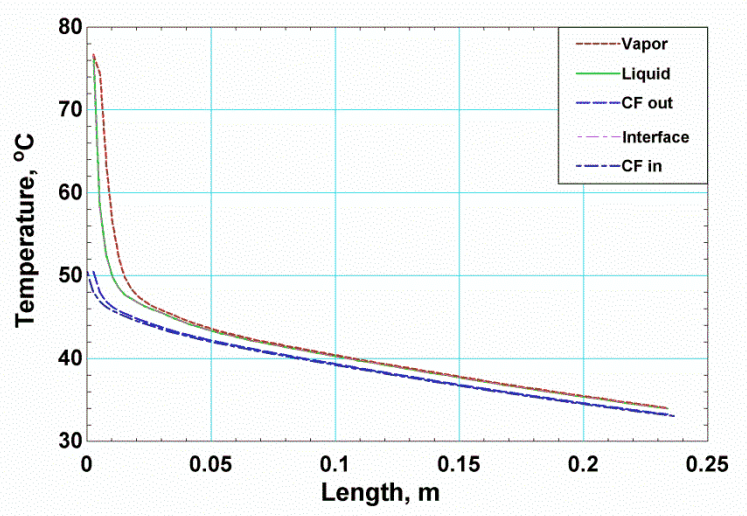

Figure 5.18: Temperature profile in absorber

cools, the vapor cools down too, albeit with a delay. This indicates that in the initial segments, poor vapor heat transfer could be limiting absorption.

Figure 5.19 presents the concentration profile of the vapor bulk, vapor interface, liquid bulk, liquid interface and the concentration of the condensing flux (z). The concentration of the condensing flux increases along the length of the absorber from 0.54 at the inlet to approaching 1 at 0.1 m, as water preferentially condenses from the vapor as it is cooled. Once most of the water condenses out of the vapor phase, the vapor and vapor interface concentration both approach unity. A large concentration difference between the interface and bulk concentration is typically an indication of low mass transfer rates. The initial difference between the vapor and interface vapor concentration is due to low mass transfer in the initial segments of the absorber. . The two-phase heat transfer coefficient (~4400 W m^{-2} K^{-1}) is much higher than the vapor-phase heat transfer coefficient (~187 W

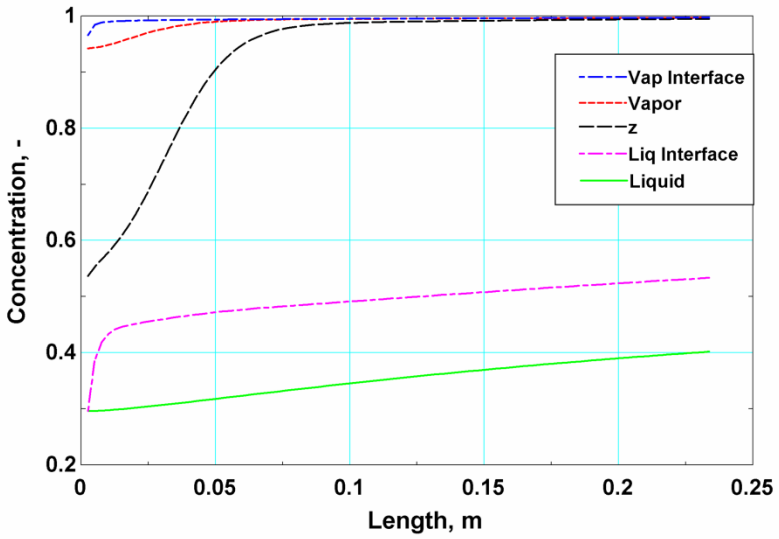

Figure 5.19: Concentration profile in absorber

m^{-2} K^{-1}). This results in a lower rate of heat transfer in the vapor compared to the liquid, especially initially, where a large temperature difference between the interface and coolant results in very high heat transfer rates. This is due to poor vapor-phase heat transfer between the vapor bulk and vapor interface compared to that between the interface and the coolant in the initial segments as seen in the temperature profiles. The liquid bulk concentration is significantly lower than the liquid interface concentration as the liquid phase has high heat transfer rates but also has a high mass transfer resistance. This high mass transfer resistance is predominantly due to lower diffusivity of ammonia and low circulation velocities in the liquid slug. The high mass transfer resistance results in the liquid phase being in a subcooled state, while the interface is in a saturated state. Unlike the vapor phase, the liquid region continues to be subcooled throughout the absorber due to the high mass transfer resistance in the liquid phase that prevents it from reaching saturation conditions. High liquid phase mass transfer resistance was also observed in the serpentine micro-pin fin absorber investigated in Chapter 4.

Figure 5.20 shows high rates of heat transfer in the first few segments due to a high sensible cooling load of the liquid phase in the microchannels, which decreases after 0.01 m. The absorption rate follows a similar trend where it rapidly increases initially up to about 0.02 m and then starts decreasing. The lag between absorption rate and the heat transfer rate is explained by the vapor phase, which has relatively high rates of sensible heat transfer up to about 0.02 m, after which the vapor and interface temperature approach each other. As the vapor cools, the absorption rate rises, and then slows down as the vapor sensible heat transfer rate starts decreasing.

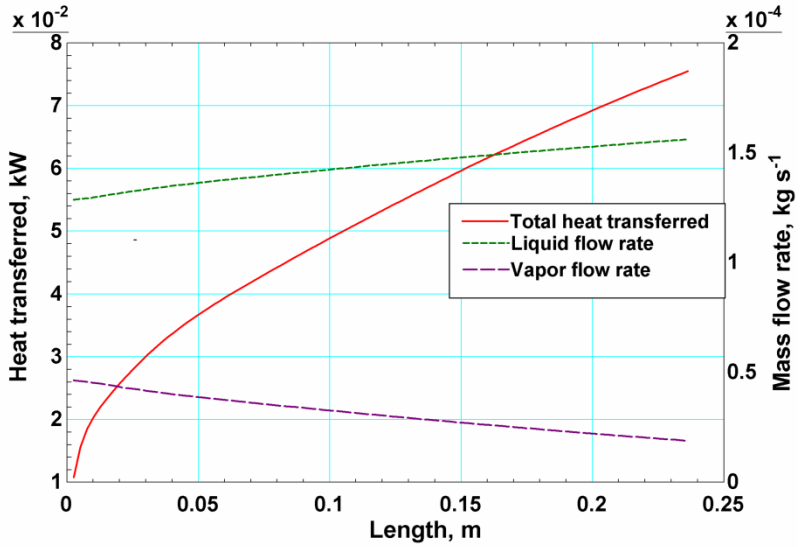

Figure 5.20: Cumulative heat transfer and mass flow rates through absorber

Figure 5.21 presents the cumulative heat transferred in the absorber and mass flow rates of the two phases. The cumulative heat transfer curve shows high rates of heat transfer initially before reaching a steadier rate. The vapor mass flow rate decreases along the length, while the liquid mass flow rate increases.

Figure 5.22 shows the pressure drop through the microchannel absorber. It is observed that the pressure does not change appreciably through the microchannel absorber. This is due to the vertically downward configuration of the absorber, where the frictional component is countered by the increase in pressure due to gravity from the top to the bottom. The net result is very low pressure drop through the microchannel absorber.

The model is validated by comparing the measured segmental heat duties with the segmental heat duty predicted by the heat and mass transfer model discussed here. Figure

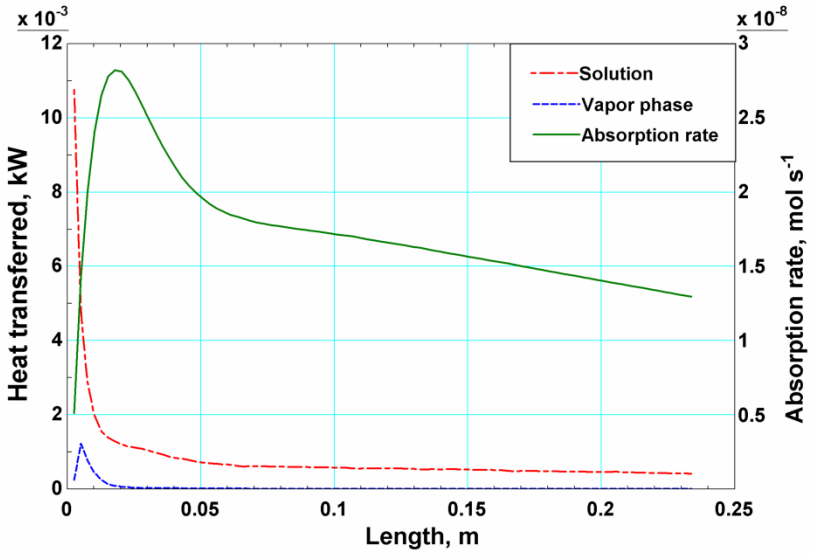

Figure 5.21: Heat and mass transfer rates in the absorber

5.23 shows that the model predicts the segmental heat duty and total heat transfer accurately.

Figure 5. 24 shows that the total heat duty of the component is predicted within 10% by the model for 37 out of 52 (70%) data points. The model slightly under predicts the heat transfer in the first section, with an average deviation (AD) of 2.7% and absolute average deviation (AAD) of 8.3%. It over predicts the heat transferred in second section with AD of 8.8% and AAD of 17.3%. The heat transfer in the bottom section is predicted with an AD of -0.4% and AAD of 15.3%. The overall total heat duty of the absorber is predicted with an AD of 2.7% and AAD of 8.6%.

Figure 5.25 presents the variation of measured and predicted segmental absorber heat duty with the liquid-only Reynolds number. It is observed that the heat duty increases with Re_{LO} for the individual segments and the overall absorber heat duty. The model

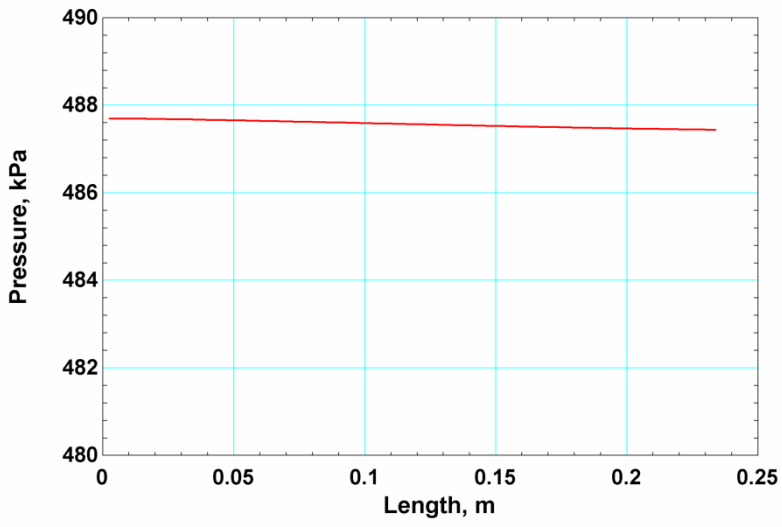

Figure 5.22: Pressure drop through the absorber

accurately predicts this trend between the absorber segmental heat duty and liquid-only Reynolds number.

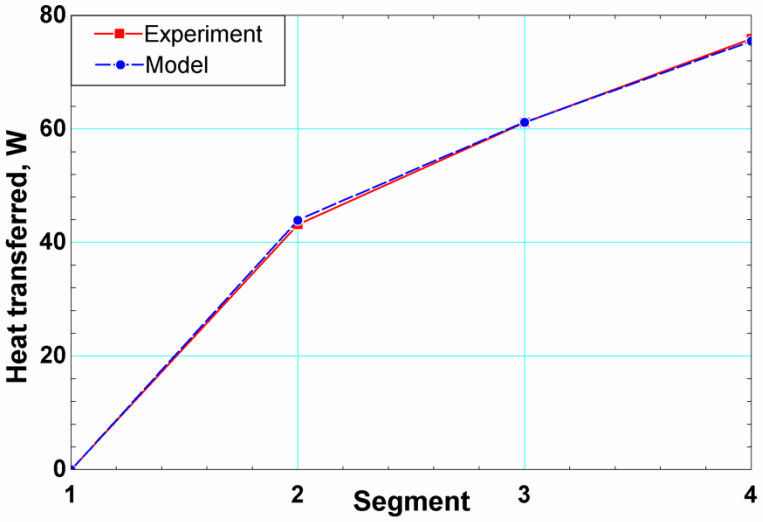

Figure 5.23: Comparison of model with experiment

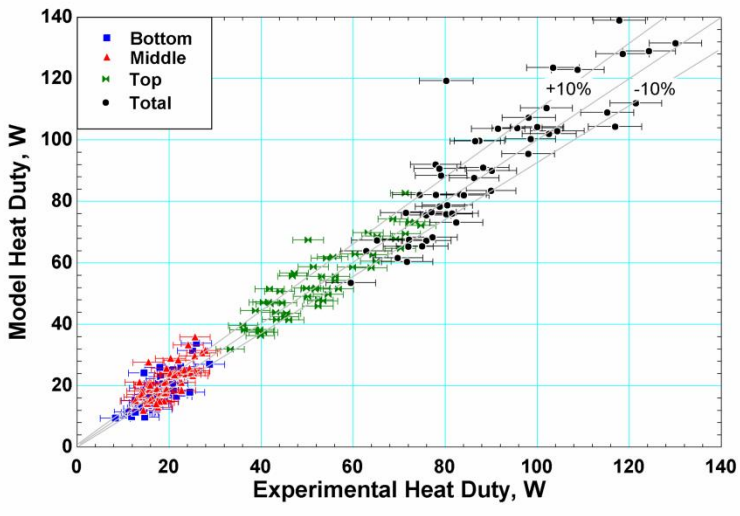

Figure 5.25: Comparison of all data with model predictions

5.7 Surfactants

The investigation of micro-pin fin and microchannel geometries showed that micro-feature absorbers are limited by high mass transfer resistance on the liquid side.

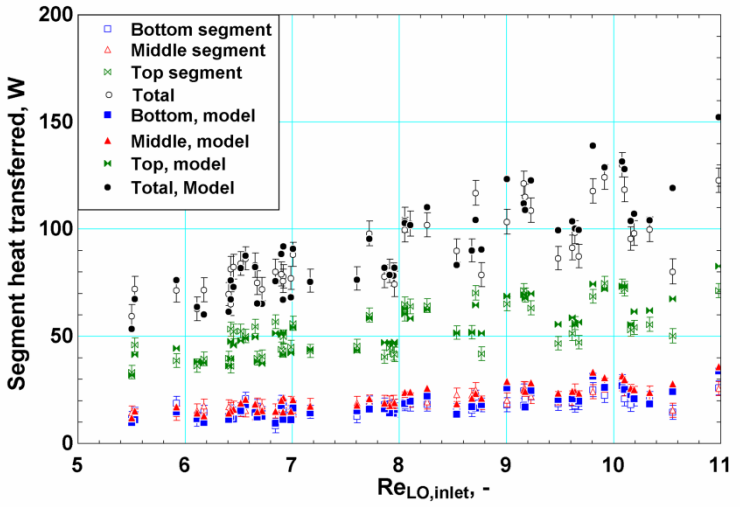

Figure 5.24: Experimental and Modeled Heat Transfer Rates

This high mass transfer resistance is due to the low diffusivity of ammonia in the liquid phase and low circulation velocities in the liquid phase. High capillary forces in these geometries decreases the wetting of surfaces and interfacial turbulence. One way to increase rates of absorption is to increase interfacial area or interfacial turbulence by using surfactants.

Surfactants have been widely studied for use in Water-LiBr absorption systems, investigations of pool absorbers showed the time taken for the surfactants to diffuse to the interface often determines the magnitude of enhancement in the rates of absorption. Kulankara and Herold (2000) investigate the impact of the surfactant 2-ethyl-1-hexanol at various concentrations on a falling-film tube-in-tube absorber. The impact of adding the surfactant was observed to be almost instantaneous, with appearance of secondary flows such as rivulets and droplets on the tube surface. The intensity of secondary flows was observed to increase with heat flux, which was attributed to vaporized surfactants that condense on the tube surface, resulting in enhanced rates of absorption through Marangoni convection.

Kang and Kashiwagi (2002) investigated the impact of n-octanol on an ammonia-water pool absorber at concentrations from 0-800 ppm. The highest rates of absorption were observed in the cases with concentrations of 800 ppm. It should be noted that the solubility of octanol in water is 75 ppm, and at the higher concentrations, islands of surfactant are observed on absorber surface. These islands were observed to be the trigger for Marangoni convection, which enhanced the rates of absorption.

Möller and Knoche (1996) investigated the effect of five surfactants, two anionic tensides, two non-ionic tensides, and n-octanol. The anionic surfactants (Marlon PS and Marlon A) reduce surface tension. The non-ionic surfactants have long chain lengths and lower diffusion velocities. The surfactants were tested in a pool absorber again, where it was observed that the two anionic surfactants and non-ionic surfactants did not affect the rates of absorption. n-octanol at concentrations of 50-500 ppm was observed to increase absorption rates. It was also found that the presence of islands of surfactants was not necessary to trigger Marangoni convection in ammonia-water mixtures. It was observed to be triggered by the salting-out or radical-out effect. In the radical-out effect, the OH^- ion of the n-octanol binds to the NH_4^+ ion and the $C_8H_{17}^+$ radical diffuses to the interface between the vapor and liquid. At the interface, this alkyl radical decreases the local surface tension, which results in the interface surface becoming wavy as curvatures of the interfaces change to match the corresponding vapor pressure. The waviness of the interface increases the interfacial area and the interfacial turbulence, resulting in higher rates of absorption.

Kim *et al.* (2006) investigated the impact of surfactants in bubble absorbers for ammonia-water systems. Three different isomers, n-octanol, 2-octanol and 2-ethyl-1-hexanol, were observed to enhance rates of absorption. They used shadowgraphy to visualize bubbles rising in the absorber. It was observed that the addition of surfactant decreased the surface tension and resulted in larger bubbles. Marangoni convection was not clearly observed in these bubbles, but the change in surface tension affects bubble formation and behavior, which was attributed to Marangoni effects. Surfactant concentrations from 0-1000 ppm were investigated, and the highest rates of absorption

were observed to be at 700 ppm for 2-ethyl-1-hexanol. The rates of absorption remained relatively constant for 100-700 ppm for n-octanol and 2-octanol. The impact of surfactants was also observed to increase at higher ammonia concentrations, indicating that the role of surfactants becomes more prominent at lower interface-bulk concentration differences.

The studies discussed above indicate the potential for the enhancement in the rates of absorption by the use of surfactants. This section investigates whether the surfactant n-octanol, which has widely been observed to enhance rates of absorption in pool and bubble absorbers, can enhance the absorption rates in the microchannel absorber. Based on prior investigations on various surfactants, it was observed that any enhancement in the rates of absorption in the microchannel absorber will be through the radical-out effect, as there will not be any islands of surfactant in the microchannel absorber. To test the impact of octanol in the present experimental setup, octanol was first dissolved to its solubility limit in distilled water and then charged into the distilled water tank shown in Figure 5.3. The solubility limit of n-octanol in water at 25°C is 75 ppm. It was ensured that no more surfactant would dissolve by the appearance of islands of surfactant in the water. Once the water-octanol solution is charged, the absorption tests were conducted on the microchannel geometry for the conditions of a nominal concentration of 0.395-0.445 and coolant temperature of 20°C resulting in n-octanol concentrations of ~43 ppm in the ammonia–water solution. Figure 5.26 presents a comparison of the apparent heat transfer coefficient for cases with n-octanol and cases without. It is observed that the use of n-octanol as a surfactant resulted in higher apparent heat transfer coefficients. The corresponding higher rates of absorption are attributed to increased interfacial turbulence

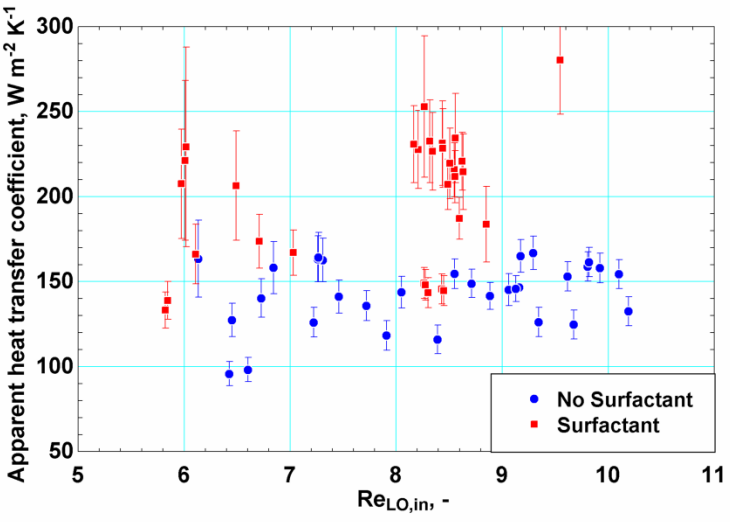

Figure 5.26: Effect of surfactants on apparent heat transfer coefficients

and interface area due to the radical-out effect. In this effect, n-octanol dissociates into $C_8H_{17}^+$ and OH^- ions, and, the OH^- ion bonds with the NH_4^+ ion, and the $C_8H_{17}^+$ ion diffuses to interface. This results in a reduction in local surface tension by up to 50% depending on local concentrations (Kim *et al.*, 2006) at various regions of the interface. This imbalance in surface tension results in increased interfacial turbulence by the formation of a wavy interface. An additional benefit of using n-octanol is that at the concentrations of about 50 ppm, it reduces the surface tension of the ammonia-water solution by about 5%. This decrease in surface tension will likely lead to slightly improved flow distribution among the microchannels, thereby increasing the interfacial area between the vapor and the liquid phases. A third reason for enhancement is obtained from the vapor surfactant theory in Kulankara and Herold (2000), where it is predicted that some of the surfactant will vaporize in the adiabatic mixer where ammonia and water with surfactant are pre-mixed before the inlet of the absorber. As the solution is cooled,

the surfactant condenses at the vapor-liquid interface, resulting in interfacial turbulence. A better understanding of the enhancement techniques can be obtained using flow visualization to investigate the changes in the interface characteristics, but foaming or any dramatic change in interfacial characteristics are not expected as they have not been observed in other studies where significantly higher concentrations of n-octanol were used.

Fluorinated surfactants are another class of surfactants that have been observed to reduce surface tension of water more effectively than hydrocarbons (Kissa, 2001). Fluorinated surfactants are classified into anionic surfactants, cationic surfactants, amphoteric surfactants and non-ionic surfactants. Based on the positive impact of octanol and its isomers, cationic fluorinated surfactants such as perfluoroalkyls, perfluoroalkaneamides, perfluorooctanesulfonamides, etc., with a hydrophobic cation and hydrophilic anion are expected to be most applicable. There are no investigations on the impact of fluorinated surfactants in absorbers, but there appears to be some potential for increasing rates of absorption. These molecules have been shown to be very stable and no material compatibility issues are expected.

While there have not been many investigations on fluorinated surfactants on absorption there has been one on heat transfer. Inoue *et al.* (2004) investigated the enhancement of pool boiling in water and water/ethanol mixtures using perfluoroalkyl surfactants. The presence of the surfactant was observed to enhance boiling heat transfer coefficients. The surfactants result in lower surface tension, resulting in smaller bubbles leaving the surface more frequently.

It should be noted that due the stable nature of fluorinated surfactants molecules, some of them have been observed to accumulate in the blood of humans, resulting in adverse health effects; hence, the chosen surfactant must have low toxicity.

5.8 Conclusions

An investigation of absorption of ammonia vapor into a dilute ammonia-water solution in microchannel geometries with intermediate mixing sections was conducted. It was observed that the flow in the microchannels was predominantly in the slug flow regime, which is not favorable for absorption due to a large mass transfer resistance on the liquid side. The absorber was tested over a range of solution flow rates, concentrations, pressures, and cooling fluid temperatures. It was observed that higher solution flow rates resulted in higher rates of heat transfer. Apparent heat transfer coefficients were observed to be between 60-180 W m^{-2} K^{-1}. The microchannel geometry with mixing sections was observed to have lower apparent heat transfer coefficients compared to the serpentine micro-pin fin geometry investigated in Chapter 4.

A physics-based model for the absorption of ammonia into a dilute solution in a microchannel absorber is developed. It was observed that the absorber had high heat transfer rates, but was limited by the mass transfer process. The liquid-phase mass transfer resistance was observed to be the dominant mass transfer resistance. A key feature of this model is the inclusion of liquid mass transfer resistance in the microchannel fin absorber, which is typically neglected in microchannel geometries. The slug flow regime was observed to be the predominant flow regime and the model was adapted to account for qualitative information obtained from the flow visualization data.

The major portion of the mass transfer was observed to occur between the vapor bubble to liquid slug interface along the length of the channel. The model is validated with experimental data and was able to predict the absorber segmental heat transfer and overall heat duty accurately.

The impact of the surfactant n-octanol is investigated and observed to increase rates of absorption in the microchannel absorber. The use of n-octanol increased the interfacial turbulence caused by the radical out phenomenon, which resulted in higher rates of absorption.

CHAPTER 6. CONCLUSIONS

A comprehensive investigation of the absorption of ammonia vapor into a dilute solution in microscale components is conducted. Flow maldistribution in microchannel geometries was investigated first. Two-phase flow through an array of microchannels was visualized to reveal that the flow is maldistributed when gas and liquid are distributed among multiple parallel channels. The implementation of mixing sections in the microchannel plate redistributes the flow more evenly. The effect of maldistribution on absorption heat and mass transfer was quantified, and improved communication between channels was shown to be critical for ensuring the desired performance.

A new geometry with serpentine passages with micro-pins was developed, and two-phase flow through this geometry was visually investigated. The micro pin fins allowed for redistribution of the two phases, resulting in an improved flow distribution in the sheets. Some maldistribution was still observed in the pin-fin geometry, as the vapor phase was observed to predominantly flow through the center of the test section. The serpentine geometry had higher mixing of the two phases compared to the microchannel design of same size. Hence, it is better suited for components with mass transfer between the two phases. Microchannel void fraction models from the literature were found to accurately predict the void fraction through the test section. The frictional pressure drop through the pin fins was the largest contributor to the overall pressure drop across the serpentine test section. A method to calculate two-phase pressure drop across a serpentine pin fin geometry was developed.

The serpentine micro-pin fin geometry is also investigated for use as an absorber for ammonia-water absorption cooling systems. Visual observations of the absorption process provided insights into the internal two-phase flow characteristics. Bridge flow is observed near the inlet of the absorber, which transitions to a gas-slug flow regime as the fluid mixture proceeds toward the outlet. The gas-slug flow regime was observed to be unfavorable for absorption due to large mass transfer resistance on the liquid side. It was also observed that while heat transfer occurred perpendicular to the absorber surface, mass transfer predominantly occurred parallel to the absorber surface. The absorber was tested over a range of three solution flow rates, concentrations, pressures, and two cooling fluid temperatures. Apparent heat transfer coefficients were observed to be between 150-1000 W m^{-2} K^{-1}. The apparent heat transfer coefficient and absorption flux were observed to increase with the liquid-only Reynolds number and with a decrease in pressure, while they were not significantly affected by solution concentration. A model for the absorption of ammonia into a dilute solution in a serpentine micro-pin fin absorber is also developed. A key feature of this model is the inclusion of liquid mass transfer resistance in the serpentine micro-pin fin absorber, which is typically neglected in microchannel geometries.The model predicts the measured absorber heat duties with an AAD of 6.6% and AD of 2.5%.

Absorption of ammonia vapor into a dilute ammonia-water solution in microchannel geometries with intermediate mixing sections was also investigated. It was observed that the flow in the microchannels was predominantly in the slug flow regime, which is not favorable for absorption due to a large mass transfer resistance on the liquid side. The absorber was tested over a range of solution flow rates, concentrations,

pressures, and cooling fluid temperatures. Apparent heat transfer coefficients were observed to be between 60-180 W m^{-2} K^{-1}. The microchannel geometry with mixing sections was observed to have lower apparent heat transfer coefficients compared to the serpentine micro-pin fin geometry investigated in Chapter 4.

A physics-based model for the absorption of ammonia into a dilute solution in a microchannel absorber is developed. It was observed that the absorber had high heat transfer rates but was limited by the mass transfer process. The liquid-phase mass transfer resistance was observed to be the dominant mass transfer resistance. Due consideration was also given to the liquid-phase mass transfer resistance in the microchannel absorber, which is typically neglected in microchannel geometries. The slug flow regime was observed to be the predominant flow regime and the model was adapted to account for qualitative information obtained from the flow visualization data. The major portion of the mass transfer was observed to occur between the vapor bubble to liquid slug interface along the length of the channel. The model is validated with experimental data, which showed that it was able to predict the absorber segmental heat transfer and overall heat duty accurately. The use of the additive n-octanol was shown to be successful in enhancing absorption rates in the microchannel absorber by increasing interfacial turbulence.

In both the serpentine micro-pin fin absorber and the microchannel absorber, a high liquid side mass transfer resistance was observed to be the bottleneck to absorption. The dominance of capillary forces over inertial forces in these microscale geometries resulted in very thin films between the vapor bubble and channel wall. These films were so thin that they did not absorb any significant quantities of ammonia from the vapor.

This resulted in ammonia having to diffuse through liquid slugs in microchannels and large lengths in the micro-pin fin geometry. Given that the diffusivity of ammonia is liquid is 1000 times lower than that in vapor, the liquid-side mass transfer resistance significantly limited performance. This high mass transfer resistance in the liquid phase led to lower than expected apparent heat transfer coefficients in the microscale absorbers. Addressing this high mass transfer resistance is critical to the development of compact absorbers.

6.1 Recommendations of future work

The present study provided some insights into flow distribution and absorption heat and mass transfer in microscale geometries. However, during the course of this study, several avenues for further research were revealed. The following are some recommendations to further advance small-scale absorbers.

The microscale absorbers investigated in this study were observed to be limited in performance by high mass transfer resistance in the liquid-phase. A detailed study of factors governing liquid-phase mass transfer resistance and designs to decrease it will further help advance this technology. Further investigations of various surfactants and their impact on microscale absorbers is also recommended based on the improvements seen with the use of n-octanol on absorption rates.

Decreasing liquid-phase mass transfer resistance using deeper channels could lead to thicker liquid films between the vapor bubbles and channel walls. A thicker liquid film would result in significant mass of ammonia being absorbed across the currently unused vapor-liquid interface. In addition to the increased active interfacial area, the film

will have a lower mass transfer resistance compared to diffusion along a liquid slug. This better utilization of the vapor-liquid interfacial area and the thin film between the vapor bubble and channel wall would improve the performance of these geometries.

Another limitation of the absorber was the co-flow nature of the vapor and liquid phases in the absorber. Co-flow absorbers typically result in unfavorable concentration gradients during mass transfer, as the concentration gradient is highest at the inlet and lowest at the outlet. The development of a counter-flow absorber, where the vapor and liquid phases flow counter to each other, will result in more favorable concentration gradients for mass transfer.

A counter-flow absorber with deeper channels has the potential to result in improved absorber design. A working fluid flow passage with a deeper flow area that operates in a bubble mode with liquid flowing from the top to bottom and vapor bubbles rising from the bottom to the top is recommended. The use of pin fins, offset fin strips or a mesh in the working fluid sheet could enhance heat transfer from the solution side to the coolant side.

This investigation observed that the use of cylindrical micro-pins in microscale absorbers improved vapor-liquid interaction in the absorber. There have been a large variety of micro-pin fin designs developed for various applications in the literature. An investigation of these alternate micro-pin fin shapes can further improve these absorbers. The development of a pin fin profile that increases interfacial area and vapor-liquid interaction has the potential to yield better performance. Pin fin profiles with sharp corners between the fin and the base have been observed to have liquid aggregate in

them, which could increase interfacial interaction between the vapor and liquid. Improved fabrication techniques would be needed to facilitate such designs.

APPENDIX A. DATA AND UNCERTAINTY ANALYSIS

Sample data and uncertainty analysis calculations of the apparent heat transfer coefficient are presented in this section.

A.1: Measurements on experimental setup

Solution side measurements	
$T_{sol,in}$	81.28±0.5°C
$T_{sol,out}$	40.5±0.5°C
$P_{sol,in}$	492.9±3.5 kPa
$\dot{m}_w$	1.078±0.004313 $\times 10^{-4}$ kg s^{-1}
$\dot{m}_{abs}$	1.847±0.007388 $\times 10^{-4}$ kg s^{-1}
Cooling fluid side measurements	

$T_{CF,bot,in}/T_{CF,abs,in}$	35.79±0.5°C
$T_{CF,bot,out}$	36.73±0.5°C
$T_{CF,mid,in}$	36.04±0.5°C
$T_{CF,mid,out}$	39.96±0.5°C
$T_{CF,top,in}$	38.69±0.5°C
$T_{CF,top,out}/T_{CF,abs,out}$	52.5±0.5°C
$\dot{m}_{CF}$	1.172±0.002344 $\times 10^{-3}$ kg s^{-1}
Miscellaneous	
T_{amb}	23.29±0.5°C

A.2: Heat loss from test section

Heat loss sample calculations		
Inputs	**Equations**	**Results**
T_{amb}=23.29°C P_{amb}=101.3 kPa $T_{sol,in}$=81.28°C $T_{sol,out}$ = 40.5°C $T_{CF,abs,in}$ = 35.79°C $T_{CF,abs,out}$=52.5°C	$R_{wall,front} = \frac{th_{plate,front}}{k_{plate} A_{plate}}$	0.035 K W^{-1}
	$R_{wall,back} = \frac{th_{plate,back}}{k_{plate} A_{plate}}$	0.009 K W^{-1}
	$R_{ins} = \frac{th_{ins}}{k_{ins} A_{ins}}$	13.94 K W^{-1}
	$R_{rad,front,i} = \frac{1}{A_{ins}\sigma_{rad}\left(T_{ins,front,i} + T_{amb}\right)\left(T_{ins,front,i}^2 + T_{amb}^2\right)}$	7.42 K W^{-1}

k_{ins} =0.041 W m^{-1} K^{-1} th_{ins}=0.0127 m $A_{ins,seg}$= 0.0222 m^2 k_{plate}= 16.2 W m^{-1} K^{-1} $th_{plate,front}$ = 0.0127 m $th_{plate,back}$ = 0.003 m $A_{plate,seg}$ = 0.0222 m^2 L = 0.35 m	$R_{rad,back,i} = \frac{1}{A_{ins}\sigma_{rad}\left(T_{ins,back,i}+T_{amb}\right)\left(T_{ins,back,i}^2+T_{amb}^2\right)}$	7.9×10^7
	$Ra_{air} = \frac{g\beta\left(T_{ins}-T_{amb}\right)L^3}{\alpha\nu}$	1.247×10^8
	$Nu_T = \frac{0.671}{\left(1+\left(0.492/\mathrm{Pr}\right)^{9/16}\right)^{4/9}}Ra^{1/4}$ $Nu_L = \frac{2}{\ln\left(1+2/Nu_T\right)}$ $Nu_{ts} = \frac{0.13\,\mathrm{Pr}^{0.22}}{\left(1+0.61\,\mathrm{Pr}^{0.81}\right)^{0.42}}\left(\frac{Ra^{1/3}}{1+1.4\times10^9\,\mathrm{Pr}/Ra}\right)$ $Nu = \left(Nu_L^6+Nu_{ts}^6\right)^{1/6}$	55.53
	$R_{free,front,i} = \frac{1}{h_{free}A_{ins}}$	10.77 K W^{-1}

	$R_{free,back,i} = \frac{1}{h_{free} A_{ins}}$	10.77 K W^{-1}
	$\dot{Q}_{loss,top} = \frac{T_{wall,front} - T_{amb}}{R_{wall,front} + R_{ins} + \frac{R_{free} R_{rad}}{R_{free} + R_{rad}}} + \frac{T_{wall,back} - T_{amb}}{R_{wall,back} + R_{ins} + \frac{R_{free} R_{rad}}{R_{free} + R_{rad}}}$	3.258 W
	$\dot{Q}_{loss,total} = \dot{Q}_{loss,top} + \dot{Q}_{loss,mid} + \dot{Q}_{loss,bot}$	6.41 W
	$\dot{Q}_{CF,top} = \dot{Q}_{CF,top,measured} + \dot{Q}_{loss,top}$	70.9 W

A.3: Data analysis method

Data reduction		
Inputs	**Equations**	**Results**
$T_{sol,in}$=81.28°C	$\dot{m}_A = \dot{m}_{abs,in} - \dot{m}_W$	$\dot{m}_A = 7.69\times10^{-5}\,\mathrm{kg\ s^{-1}}$
$T_{sol,out}$=40.5°C	$\dot{m}_{abs,in} x_{abs,in} = \dot{m}_A x_A + \dot{m}_W x_W$	$x_{abs,in} = 0.416$
$P_{sol,in}$=492.5 kPa	$q_{abs,in} = f(T_{abs,in}, P_{abs,in}, x_{abs,in})$	$q_{abs,in} = 0.214$
$\dot{m}_w$ =1.078×10^{-4} kg s^{-1}	$x_{liq,in} = f(T_{abs,in}, P_{abs,in}, q_{liq,in} = 0)$	$x_{liq,in} = 0.2769$
$\dot{m}_{abs}$ =1.847×10^{-4} kg s^{-1}	$x_{vap,in} = f(T_{abs,in}, P_{abs,in}, q_{vap,in} = 1)$	$x_{vap,in} = 0.928$
$T_{CF,bot,in}$/$T_{CF,abs,in}$=35.79°C	$\dot{Q}_{top} = \dot{m}_{CF} C_{p,CF} \left(T_{top,out} - T_{top,in}\right) + \dot{Q}_{loss,top}$	70.9±3.5 W

$T_{CF,bot,out}$=36.73°C	$\dot{Q}_{mid} = \dot{m}_{CF} C_{p,CF} \left(T_{mid,out} - T_{mid,in} \right) + \dot{Q}_{loss,seg}$	20.9±3.5 W
$T_{CF,mid,in}$=36.04°C	$\dot{Q}_{bot} = \dot{m}_{CF} C_{p,CF} \left(T_{bot,in} - T_{bot,out} \right) + \dot{Q}_{loss,bot}$	6±3.5 W
$T_{CF,mid,out}$=39.96°C	$\dot{Q}_{abs,CF} = \dot{Q}_{seg,top} + \dot{Q}_{seg,mid} + \dot{Q}_{seg,bot}$	97.8±6.1 W
$T_{CF,top,in}$=38.69°C	$\dot{Q}_{abs,sol} = \dot{m}_{sol,in} \begin{pmatrix} h_{sol,in}\left(T_{sol,in}, P_{sol,in}, x_{sol,in}\right) \\ -h_{sol,out}\left(T_{sol,out}, P_{sol,out}, x_{sol,out}\right) \end{pmatrix}$	95.7±2.3 W
$T_{CF,top,out}/T_{CF,abs,out}$=52.5°C	$\dot{Q}_{abs,CF} = UA \cdot \Delta T_{LM} \left(T_{sol,in} T_{CF,out}, T_{sol,out}, T_{CF,in} \right)$	UA_{abs} = 7.59±0.59 W K^{-1}
$\dot{m}_{CF}$ =1.17×10^{-3} kg s^{-1}	$R_{sol} = \frac{1}{UA} - R_{wall} - R_{CF}$	R_{sol} = 0.1224±0.01018 K W^{-1}
	$\alpha'_{abs} = \frac{1}{R_{sol} A_{serp,ht}}$	256.1±21.3 W m^{-2} K^{-1}
	$\dot{m}_{sol} h_{sol,out} = \dot{m}_{sol} h_{sol,in} - \dot{Q}_{abs,cf}$	$h_{sol,out} = -64.92$ kJ kg^{-1}

	$\dot{m}_{sol} = \dot{m}_{vap,out} + \dot{m}_{liq,out}$ $\dot{m}_{sol} x_{sol,out} = \dot{m}_{vap,out} x_{vap,out} + \dot{m}_{liq,out} x_{liq,out}$ $\dot{m}_{sol} h_{sol,out} = \dot{m}_{vap,out} h_{vap,out}\left(P_{abs,out}, T_{sol,out}, q_{vap,out} = 1\right)$ $+\dot{m}_{liq,out} h_{liq,out}\left(P_{abs,out}, T_{sol,out}, x_{liq,out}\right)$	$\dot{m}_{vap,out} = 0$ $\dot{m}_{liq,out} = 1.847 \times 10^{-4}\ \mathrm{kg\ s^{-1}}$

APPENDIX B. MODEL SAMPLE CALCULATIONS

B.1: Sample Calculation

Sample calculation		
Inputs	**Equations**	**Results**
$A_{int} = 5.75\times10^{-5}$ m^2 $D_v = 6.41\times10^{-6}$ m^2 s^{-1} $D_L = 4.25\times10^{-9}$ m^2 s^{-1} $D_h = 0.67$ mm $h_{v,in} = 1367$ kJ kg^{-1}	$Sh_{d,vap} = 31.4\,\mathrm{Re}_d^{0.371} Ca_d^{0.371} Fo_d^{-0.338} Sc_{d,v}^{-0.125}$	4.845
	$\beta_{vap} = \frac{Sh_{d,vap} D_v}{d_h}$	0.04619 m s^{-1}
	$\dot{n}''_T = \beta_{vap} \times C_{vap,T} \times \ln\left(\frac{\tilde{z} - \tilde{x}_{vap,int}}{\tilde{z} - \tilde{x}_{vap,bulk}}\right)$	2.91×10^{-4} kmol m^{-2} s^{-1}
	$\dot{m}_{abs,A} = \dot{n}''_A \cdot A_{int} \cdot M_A$	2.82×10^{-7} kg s^{-1}

$h_{L,in}$ = -39.65 kJ kg^{-1}	$\dot{m}_{abs,w} = (1-z)\dot{n}_T'' \cdot A_{int} \cdot M_w$	3.05×10^{-9} kg s^{-1}
$m_{v,in}$ = 3.103×10^{-5} kg s^{-1}	$\dot{m}_{v,out} = \dot{m}_{v,in} - \dot{m}_{abs,A} - \dot{m}_{abs,W}$	3.075×10^{-5}kg s^{-1}
$m_{L,in}$ = 1.44×10^{-4} kg s^{-1}	$\dot{m}_{v,out} \cdot x_{v,out} = \dot{m}_{v,in} \cdot x_{v,in} - \dot{m}_{abs,A}$	$x_{v,out}$ = 0.9953
$T_{L,in}$= 39.4°C $T_{L,int,in}$= 39.4°C	$R_{CF} = \frac{1}{\alpha_{CF} \cdot L_{seg} \cdot \left(L_{flat} + \eta_{fin} L_{fin}\right)}$	0.8825 K W^{-1}
$T_{v,in}$ = 39.52°C $T_{v,int,in}$= 39.4°C	$R_{wall} = \frac{th_{wall}}{k_{wall} L_{seg} w_{wall}}$	0.1976 K W^{-1}
	$R_{sol} = \frac{1}{\alpha_{sol} \cdot L_{seg} \cdot \left(L_{flat} + \eta_{fin} L_{fin}\right)}$	0.5394 K W^{-1}
$T_{CF,out}$ = 38.49°C	$\left(U \cdot A\right)_{abs} = \frac{1}{R_{abs}} = \frac{1}{R_{sol} + R_{wall} + R_{CF}}$	0.6175 W K^{-1}

$x_{v,in} = 0.9953$ $x_{v,int} = 0.9955$ $x_{L,in} = 0.354$ $x_{L,int} = 0.497$ z = 0.9899(assumed)	$\dot{Q}_{abs} = \dot{m}_{CF} \cdot C_{p,CF} \cdot \left(T_{CF,out} - T_{CF,in}\right)$ $\dot{Q}_{abs} = \left(U \cdot A\right)_{abs} \cdot \Delta T_{LM,int,CF}$ $\Delta T_{LM,int,CF} = \frac{\left(T_{L,\text{int},in} - T_{CF,out}\right) - \left(T_{L,\text{int},out} - T_{CF,in}\right)}{\ln\left(\frac{T_{L,\text{int},in} - T_{CF,out}}{T_{L,\text{int},out} - T_{CF,in}}\right)}$ $\dot{Q}_{abs} = \dot{m}_{v,in} \cdot h_{v,in} + \dot{m}_{L,in} \cdot h_{L,in} - \dot{m}_{v,out} \cdot h_{v,out} - \dot{m}_{L,out} \cdot h_{L,out}$ $T_L = T_{\text{int}}$ $h_{v,out} = f\left(T_{v,out}, x_{v,out}, P_{v,out}\right)$ $h_{L,out} = f\left(T_{L,out}, x_{L,out}, P_{L,out}\right)$ $\dot{Q}_v = \dot{m}_v \cdot C_{p,v} \cdot \left(T_{v,in} - T_{v,out}\right)$ $\dot{Q}_v = \alpha_v \left(\frac{\phi}{1 - e^{-\phi}}\right) A_{int} \cdot \Delta T_{LM,v,int}$ $\Delta T_{LM,v,\text{int}} = \frac{\left(T_{v,in} - T_{v,\text{int},in}\right) - \left(T_{v,out} - T_{v,\text{int},out}\right)}{\ln\left(\frac{T_{v,in} - T_{v,\text{int},in}}{T_{v,out} - T_{v,\text{int},out}}\right)}$ $T_{v,\text{int}} = T_{L,\text{int}}$	Equations are solved iteratively to get the 11 parameters below $h_{v,out} = 1366$ kJ kg^{-1} $h_{L,out} = -40.68$ kJ kg^{-1} $T_{CF,in} = 38.36°C$ $T_{L,out} = 39.27°C$ $T_{L,int,out} = 39.27°C$ $T_{v,int,out} = 39.27°C$ $T_{v,out} = 39.34°C$ $Q_{abs} = 0.5617$ W $Q_v = 0.0097$ W

		$\Delta T_{LM,int,CF} = 0.9098°C$ $\Delta T_{LM,v,int} = 0.1194°C$
	$Sh_{d,Liq} = 31.4\,\mathrm{Re}_d^{0.371}\,Ca_d^{0.371}\,Fo_d^{-0.338}\,Sc_{d,L}^{-0.125} = 4.834$	3.68
	$\beta_L = \frac{Sh_{d,L} D_L}{d_h}$	2.32×10^{-5} m s^{-1}
	$\dot{n}''_T = -\beta_{Liq} \times C_{Liq,T} \times \ln\left(\frac{\tilde{z} - \tilde{x}_{Liq,int}}{\tilde{z} - \tilde{x}_{Liq,bulk}}\right)$	z which was assumed initially is now calculated iteratively from this equation

REFERENCES

Ahmad, M., G. Berthoud and P. Mercier (2009), "General Characteristics of Two-Phase Flow Distribution in a Compact Heat Exchanger," *International Journal of Heat and Mass Transfer* Vol. 52 pp. 442-450

ANSYS Inc. (2016). *Fluent*. Lebanon, NH.

Balasubramanian, P. and S. G. Kandlikar (2005), "Experimental Study of Flow Patterns, Pressure Drop, and Flow Instabilities in Parallel Rectangular Minichannels," *Heat Transfer Engineering* Vol. 26(3) pp. 20-27

Bell, K. J. and M. A. Ghaly (1973), "An Approximate Generalized Design Method for Multicomponent/Partial Condensers," *AlchE Symposium Series Heat Transfer Research and Design* Vol. 69(72-79)

Beutler, A., L. Hoffmann, F. Ziegler, G. Alefeld, K. Gommed, G. Grossman and A. Shavit (1996), "Experimental Investigation of Heat and Mass Transfer on Horizontal and Vertical Tubes," *Proceedings of the International Ab-Sorption Heat Pump Conference*, Montreal, Canada, pp. 409-419.

Cavallini, A., D. D. Col, L. Doretti, M. Matkovic, L. Rossetto, C. Zilio and G. Censi (2006), "Condensation in Horizontal Smooth Tubes: A New Heat Transfer Model for Heat Exchanger Design," *Heat Transfer Engineering* Vol. 27(8) pp. 31-38

Cerezo, J., R. Best, M. Bourouis and A. Coronas (2010), "Comparison of Numerical and Experimental Performance Criteria of an Ammonia–Water Bubble Absorber

Using Plate Heat Exchangers," *International Journal of Heat and Mass Transfer* Vol. 53(17–18) pp. 3379-3386 DOI: http://dx.doi.org/10.1016/j.ijheatmasstransfer.2010.02.031.

Cerezo, J., M. Bourouis, M. Vallès, A. Coronas and R. Best (2009), "Experimental Study of an Ammonia–Water Bubble Absorber Using a Plate Heat Exchanger for Absorption Refrigeration Machines," *Applied Thermal Engineering* Vol. 29(5) pp. 1005-1011

Chaoqun, Y., Z. Yuchao, Y. Chunbo, D. Minhui, D. Zhengya and C. Guangwen (2013), "Characteristics of Slug Flow with Inertial Effects in a Rectangular Microchannel," *Chemical Engineering Science* Vol. 95(Supplement C) pp. 246-256 DOI: https://doi.org/10.1016/j.ces.2013.03.046.

Chisholm, D. (1980), "Two-Phase Flow in Bends," *International Journal of Multiphase Flow* Vol. 6(4) pp. 363-367

Colburn, A. P. and T. B. Drew (1937), "The Condensation of Mixed Vapours," *AIChE Transactions* Vol. 33 pp. 197-212

Dessimoz, A.-L., L. Cavin, A. Renken and L. Kiwi-Minsker (2008), "Liquid–Liquid Two-Phase Flow Patterns and Mass Transfer Characteristics in Rectangular Glass Microreactors," *Chemical Engineering Science* Vol. 63(16) pp. 4035-4044 DOI: https://doi.org/10.1016/j.ces.2008.05.005.

Determan, M. D. and S. Garimella (2012), "Design, Fabrication, and Experimental Demonstration of a Microscale Monolithic Modular Absorption Heat Pump,"

Applied Thermal Engineering Vol. 47(0) pp. 119-125 DOI: http://dx.doi.org/10.1016/j.applthermaleng.2011.10.043.

Di Miceli Raimondi, N., L. Prat, C. Gourdon and P. Cognet (2008), "Direct Numerical Simulations of Mass Transfer in Square Microchannels for Liquid–Liquid Slug Flow," *Chemical Engineering Science* Vol. 63(22) pp. 5522-5530 DOI: https://doi.org/10.1016/j.ces.2008.07.025.

Fei, P. and P. Hrnjak (2004). *Adiabatic Developing Two-Phase Refrigerant Flow in Manifolds of Heat Exchangers*. A. C. a. R. Center. University of Illinois at Urbana-Champaign, Vol. TR-225.

Fronk, B. M. and S. Garimella (2016), "Condensation of Ammonia and High-Temperature-Glide Zeotropic Ammonia/Water Mixtures in Minichannels – Part Ii: Heat Transfer Models," *International Journal of Heat and Mass Transfer* Vol. 101 pp. 1357-1373 DOI: http://dx.doi.org/10.1016/j.ijheatmasstransfer.2016.05.048.

Garimella, S., A. Agarwal and J. D. Killion (2005a), "Condensation Pressure Drop in Circular Microchannels," *Heat Transfer Engineering* Vol. 26(3) pp. 28-35 DOI: 10.1080/01457630590907176.

Garimella, S., A. Agarwal and J. D. Killion (2005b), "Condensation Pressure Drop in Circular Microchannels," *Heat Transfer Engineering* Vol. 26(3) pp. 1-8

Garimella, S., C. M. Keinath, J. C. Delahanty, D. C. Hoysall, M. A. Staedter, A. Goyal and M. A. Garrabrant (2016), "Development and Demonstration of a Compact

Ammonia–Water Absorption Heat Pump Prototype with Microscale Features for Space-Conditioning Applications," *Applied Thermal Engineering* Vol. 102 pp. 557-564 DOI: http://dx.doi.org/10.1016/j.applthermaleng.2016.03.169.

Goyal, A., M. A. Staedter, D. C. Hoysall, M. J. Ponkala and S. Garimella (2017), "Experimental Evaluation of a Small-Capacity, Waste-Heat Driven Ammonia-Water Absorption Chiller," *International Journal of Refrigeration* Vol. 79 pp. 89-100 DOI: http://dx.doi.org/10.1016/j.ijrefrig.2017.04.006.

Herbine, G. S. and H. Perez-Blanco (1995), "Model of an Ammonia-Water Bubble Absorber," *Proceedings of the 1995 ASHRAE Annual Meeting, Jan 29-Feb 1 1995*, Chicago, IL, USA, ASHRAE, Atlanta, GA, USA, pp. 1324-1332.

Hetsroni, G., A. Mosyak, Z. Segal and E. Pogrebnyak (2003), "Two-Phase Flow Patterns in Parallel Micro-Channels," *International Journal of Multiphase Flow* Vol. 29(3) pp. 341-360 DOI: http://dx.doi.org/10.1016/S0301-9322(03)00002-8.

Inoue, T., Y. Teruya and M. Monde (2004), "Enhancement of Pool Boiling Heat Transfer in Water and Ethanol/Water Mixtures with Surface-Active Agent," *International Journal of Heat and Mass Transfer* Vol. 47(25) pp. 5555-5563 DOI: https://doi.org/10.1016/j.ijheatmasstransfer.2004.05.037.

Jenks, J. and V. Narayanan (2006), "An Experimental Study of Ammonia-Water Bubble Absorption in a Large Aspect Ratio Microchannel," (47853) pp. 243-249 DOI: 10.1115/IMECE2006-14036.

Jenks, J. and V. Narayanan (2008), "Effect of Channel Geometry Variations on the Performance of a Constrained Microscale-Film Ammonia-Water Bubble Absorber," *Journal of Heat Transfer* Vol. 130(11) pp. 112402-112402-112409 DOI: 10.1115/1.2970065.

Kakac, S., R. K. Shah and W. Aung (1987). *Handbook of Single-Phase Convective Heat Transfer*. New York, Wiley.

Kandlikar, S. G. and P. Balasubramanian (2005), "An Experimental Study on the Effect of Gravitational Orientation on Flow Boiling of Water in 1054×197 Mm Parallel Minichannels," *Journal of Heat Transfer-transactions of The Asme* Vol. 127(8) DOI: 10.1115/1.1928911.

Kandlikar, S. G., M. Steinke, S. Tian and L. A. Campbell (2001), "High-Speed Photographic Observation of Flow Boiling of Water in Parallel Mini-Channels," *35th Proceedings of National Heat Transfer Conference*

Kang, Y. T., A. Akisawa and T. Kashiwagi (2000), "Analytical Investigation of Two Different Absorption Modes: Falling Film and Bubble Types," *International Journal of Refrigeration* Vol. 23 pp. 430-433

Kang, Y. T., R. N. Christensen, T. Kashiwagi and F. Ziegler (1998), "Ammonia-Water Bubble Absorber with a Plate Heat Exchanger/Discussion," *ASHRAE Transactions* Vol. 104 p. 1565

Kang, Y. T. and T. Kashiwagi (2002), "Heat Transfer Enhancement by Marangoni Convection in the Nh_3-H_2o Absorption Process," *International Journal of Refrigeration* Vol. 25(6) pp. 780-788

Kashid, M. N., I. Gerlach, S. Goetz, J. Franzke, J. F. Acker, F. Platte, D. W. Agar and S. Turek (2005), "Internal Circulation within the Liquid Slugs of a Liquid−Liquid Slug-Flow Capillary Microreactor," *Industrial & Engineering Chemistry Research* Vol. 44(14) pp. 5003-5010 DOI: 10.1021/ie0490536.

Kawahara, A., P. M.-Y. Chung and M. Kawaji (2002), "Investigation of Two-Phase Flow Pattern, Void Fraction and Pressure Drop in a Microchannel," *International Journal of Multiphase Flow* Vol. 28(9) pp. 1411-1435

Keinath, B. and S. Garimella (2016), "Measurement and Modeling of Void Fraction in High-Pressure Condensing Flows through Microchannels," *Heat Transfer Engineering* Vol. 37(13-14) pp. 1172-1180 DOI: 10.1080/01457632.2015.1112590.

Kim, J.-K., J. Y. Jung, J. H. Kim, M.-G. Kim, T. Kashiwagi and Y. T. Kang (2006), "The Effect of Chemical Surfactants on the Absorption Performance During Nh3/H2o Bubble Absorption Process," *International Journal of Refrigeration* Vol. 29(2) pp. 170-177 DOI: https://doi.org/10.1016/j.ijrefrig.2005.06.006.

Kim, S.-M. and I. Mudawar (2013), "Universal Approach to Predicting Heat Transfer Coefficient for Condensing Mini/Micro-Channel Flow," *International Journal of*

Heat and Mass Transfer Vol. 56(1) pp. 238-250 DOI: https://doi.org/10.1016/j.ijheatmasstransfer.2012.09.032.

Kissa, E. (2001). *Fluorinated Surfactants and Repellants*. 2 Ed., Marcel Dekker Inc.

Kosar, A., C. Mishra and Y. Peles (2005), "Laminar Flow across a Bank of Low Aspect Ratio Micro Pin Fins," *Journal of Fluids Engineering, Transactions of the ASME* Vol. 127(3) pp. 419-430

Krishnamurthy, S. and Y. Peles (2007), "Gas-Liquid Two-Phase Flow across a Bank of Micropillars," *Physics of Fluids (1994-present)* Vol. 19(4) p. 043302 DOI: doi:http://dx.doi.org/10.1063/1.2722424.

Krishnamurthy, S. and Y. Peles (2008a), "Flow Boiling of Water in a Circular Staggered Micro-Pin Fin Heat Sink," *International Journal of Heat and Mass Transfer* Vol. 51(5–6) pp. 1349-1364 DOI: http://dx.doi.org/10.1016/j.ijheatmasstransfer.2007.11.026.

Krishnamurthy, S. and Y. Peles (2008b), "Two-Phase Flow Pattern Transition across Micropillars: Size Scale Effect at the Microscale," *Physics of Fluids (1994-present)* Vol. 20(2) p. 023602 DOI: doi:http://dx.doi.org/10.1063/1.2868762.

Kulankara, S. and K. E. Herold (2000), "Theory of Heat/Mass Transfer Additives in Absorption Chillers," *HVAC&R Research* Vol. 6(4) pp. 369-380 DOI: 10.1080/10789669.2000.10391422.

Lee, K. B., B. H. Chun, J. C. Lee, J. C. Hyun and S. H. Kim (2002a), "Comparison of Heat and Mass Transfer in Falling Film and Bubble Absorbers of Ammonia-Water," *Experimental Heat Transfer* Vol. 15(3) pp. 191 - 205

Lee, K. B., B. H. Chun, J. C. Lee, C. H. Lee and S. H. Kim (2002b), "Experimental Analysis of Bubble Mode in a Plate-Type Absorber," *Chemical Engineering Science* Vol. 57(11) pp. 1923-1929 DOI: http://dx.doi.org/10.1016/S0009-2509(02)00089-1.

Lockhart, R. W. and R. C. Martinelli (1949), "Proposed Correlation of Data for Isothermal Two-Phase, Two Component Flow in Pipes," *Chemical Engineering Progress* Vol. 45(1) pp. 39 - 48

Mahvi, A. J. and S. Garimella (2017), "Visualization of Flow Distribution in Rectangular and Triangular Header Geometries," *International Journal of Refrigeration* Vol. 76(Supplement C) pp. 170-183 DOI: https://doi.org/10.1016/j.ijrefrig.2017.02.002.

Marchitto, A., F. Devia, M. Fossa, G. Guglielmini and C. Schenone (2008), "Experiments on Two-Phase Flow Distribution inside Parallel Channels of Compact Heat Exchangers," *International Journal of Multiphase Flow* Vol. 34(2) pp. 128-144 DOI: DOI 10.1016/j.ijmultiphaseflow.2007.08.005.

McNeil, D., A. Raeisi, P. Kew and P. Bobbili (2010), "A Comparison of Flow Boiling Heat-Transfer in in-Line Mini Pin Fin and Plane Channel Flows," *Applied thermal engineering* Vol. 30(16) pp. 2412-2425

McNeil, D. A., A. H. Raeisi, P. A. Kew and R. S. Hamed (2014), "An Investigation into Flow Boiling Heat Transfer and Pressure Drop in a Pin–Finned Heat Sink," *International Journal of Multiphase Flow* Vol. 67, Supplement(0) pp. 65-84 DOI: http://dx.doi.org/10.1016/j.ijmultiphaseflow.2014.06.012.

Mehdizadeh, A., S. A. Sherif and W. E. Lear (2009), "Cfd Modeling of Two-Phase Gas-Liquid Slug Flow Using Vof Method in Microchannels," *ASME 2009 Fluids Engineering Division Summer Meeting*, Vail, Colorado, ASME

Merrill, T. L., T. Setoguchi and H. Perez-Blanco (1994), "Compact Bubble Absorber Design and Analysis," *Proceedings of the International Absorption Heat Pump Conference, Jan 19-21 1994*, New Orleans, LA, USA, ASME, New York, NY, USA, pp. 217-223.

Merrill, T. L., T. Setoguchi and H. Perez-Blanco (1995), "Passive Heat Transfer Enhancement Techniques Applied to Compact Bubble Absorber Design," *Journal of Enhanced Heat Transfer* Vol. 2(3) pp. 199-208

Merrill, T. L., T. Setoguchi and H. Perez-Blanco (1998), "Compact Bubble Absorber Design," Vol. 5(4) pp. 249-256

Möller, R. and K. F. Knoche (1996), "Surfactants with Nh3・H2o," *International Journal of Refrigeration* Vol. 19(5) pp. 317-321 DOI: https://doi.org/10.1016/S0140-7007(96)00035-7.

Nagavarapu, A. K. (2012). *Binary Fluid Heat and Mass Exchange at the Microscales in Internal and External Ammonia-Water Absorption*. Mechanical Engineering. Atlanta, Georgia Institute of Technology, Vol. PhD p. 422.

Nagavarapu, A. K. and S. Garimella (2011), "Design of Microscale Heat and Mass Exchangers for Absorption Space Conditioning Applications," *Journal of Thermal Science and Engineering Applications* Vol. 3(2) pp. 021005-021005 DOI: 10.1115/1.4003720.

Ozawa, M., K. Akagawa and T. Sakaguchi (1989), "Flow Instabilities in Parallel-Channel Flow Systems of Gas-Liquid Two-Phase Mixtures," *International Journal of Multiphase Flow* Vol. 15(4) pp. 639-657 DOI: http://dx.doi.org/10.1016/0301-9322(89)90058-X.

Peles, Y. (2003), "Two-Phase Boiling Flow in Microchannels: Instabilities Issues and Flow Regime Mapping," *1st International Conference on Microchannels and Minichannels*, Rochester, New York, USA, ASME, pp. 559-566.

Peles, Y., A. Kosar, C. Mishra, C.-J. Kuo and B. Schneider (2005), "Forced Convective Heat Transfer across a Pin Fin Micro Heat Sink," *International Journal of Heat and Mass Transfer* Vol. 48(17) pp. 3615-3627

Prasher, R. S., J. Dirner, J.-Y. Chang, A. Myers, D. Chau, D. He and S. Prstic (2006), "Nusselt Number and Friction Factor of Staggered Arrays of Low Aspect Ratio Micropin-Fins under Cross Flow for Water as Fluid," *Journal of Heat Transfer* Vol. 129(2) pp. 141-153 DOI: 10.1115/1.2402179.

Price, B. C. and K. J. Bell (1974), "Design of Binary Vapor Condensers Using the Colburn-Drew Equations," *AIChE Symposium Series - Heat Transfer - Research and Design* Vol. 70(138) pp. 163-171

Qu, W. and A. Siu-Ho (2008), "Liquid Single-Phase Flow in an Array of Micro-Pin-Fins—Part Ii: Pressure Drop Characteristics," *Journal of Heat Transfer* Vol. 130(12) pp. 124501-124501 DOI: 10.1115/1.2970082.

Qu, W. and A. Siu-Ho (2009), "Measurement and Prediction of Pressure Drop in a Two-Phase Micro-Pin-Fin Heat Sink," *International Journal of Heat and Mass Transfer* Vol. 52(21–22) pp. 5173-5184 DOI: http://dx.doi.org/10.1016/j.ijheatmasstransfer.2009.05.007.

Rattner, A. S. and S. Garimella (2011), "Energy Harvesting, Reuse and Upgrade to Reduce Primary Energy Usage in the USA," *Energy* Vol. 36(10) pp. 6172-6183

Reeser, A., A. Bar-Cohen and G. Hetsroni (2014), "High Quality Flow Boiling Heat Transfer and Pressure Drop in Microgap Pin Fin Arrays," *International Journal of Heat and Mass Transfer* Vol. 78 pp. 974-985

Schrage, D. S., J. T. Hsu and M. K. Jensen (1988), "Two-Phase Pressure Drop in Vertical Crossflow across a Horizontal Tube Bundle," *AIChE Journal* Vol. 34(1) pp. 107-115 DOI: 10.1002/aic.690340112.

Silver, L. (1947), "Gas Cooling with Aqueous Condensation," *Industrial Chemist and Chemical Manufacturer* Vol. 23(269) pp. 380-386

Sobieszuk, P., R. Pohorecki, P. Cygański and J. Grzelka (2011), "Determination of the Interfacial Area and Mass Transfer Coefficients in the Taylor Gas–Liquid Flow in a Microchannel," *Chemical Engineering Science* Vol. 66(23) pp. 6048-6056 DOI: https://doi.org/10.1016/j.ces.2011.08.029.

Sparrow, E. M. and A. Haji-Sheikh (1965), "Laminar Heat Transfer and Pressure Drop in Isosceles Triangular, Right Triangular, and Circular Sector Ducts," *Journal of Heat Transfer* Vol. 87(3) pp. 426-427 DOI: 10.1115/1.3689131.

Tshuva, M., D. Barnea and Y. Taitel (1999), "Two-Phase Flow in Inclined Parallel Pipes," *International Journal of Multiphase Flow* Vol. 25(6–7) pp. 1491-1503 DOI: http://dx.doi.org/10.1016/S0301-9322(99)00048-8.

U.S.EIA (2016). *International Energy Outlook 2016*. www.eia.gov, U.S. Energy Information Administration p. 276.

Vandu, C. O., H. Liu and R. Krishna (2005), "Mass Transfer from Taylor Bubbles Rising in Single Capillaries," *Chemical Engineering Science* Vol. 60(22) pp. 6430-6437 DOI: https://doi.org/10.1016/j.ces.2005.01.037.

Vist, S. and J. Pettersen (2004), "Two-Phase Flow Distribution in Compact Heat Exchanger Manifolds," *Experimental Thermal and Fluid Science* Vol. 28(2-3) pp. 209-215 DOI: Doi 10.1016/S0894-1777(03)00041-4.

Winkler, J., J. Killion and S. Garimella (2012), "Void Fractions for Condensing Refrigerant Flow in Small Channels. Part Iı: Void Fraction Measurement and

Modeling," *International Journal of Refrigeration* Vol. 35(2) pp. 246-262 DOI: http://dx.doi.org/10.1016/j.ijrefrig.2011.08.012.

Yue, J., G. Chen, Q. Yuan, L. Luo and Y. Gonthier (2007), "Hydrodynamics and Mass Transfer Characteristics in Gas–Liquid Flow through a Rectangular Microchannel," *Chemical Engineering Science* Vol. 62(7) pp. 2096-2108 DOI: https://doi.org/10.1016/j.ces.2006.12.057.